UNIVERSITY OF MESSINA
DEPARTMENT OF ENGINEERING
PhD Course in "Industrial and Information Engineering"
Coordinator: ***Prof. Edoardo Proverbio***

UBIQUITOUS MICROWAVE AND MM-WAVE RADARS FOR ADVANCED MOTION DETECTION

Doctoral Dissertation of:
Eng. Luigi Ferro

Supervisor:
Prof. Graziella Scandurra

Co-Supervisor:
Prof. Emanuele Cardillo

SSD IINF-01/A

Academic Year 2024/25 – XXXVIII CYCLE

COESIONE ITALIA 21-27 SICILIA | Cofinanziato dall'Unione europea | Regione Siciliana

Ringraziamenti

"Il cuor dell'uomo medita la sua via, ma l'Eterno dirige i suoi passi." (Proverbi 16:9).

Vorrei esprimere la mia più sincera gratitudine nei confronti di Emanuele, colui che mi ha inizialmente spinto a rientrare professionalmente a Messina mostrando, in primis, fiducia nei miei confronti e promettendo il suo massimo impegno. Comincio con una borsa pre-dottorato il cui bando è stato scritto mentre non sapeva nemmeno se la sua carriera universitaria potesse continuare. Continuo col dottorato sebbene ufficialmente non potesse essere il mio Supervisore. Grazie perché non sei venuto meno all'impegno promesso e per esserci stato quando ero ad un passo dalla sedia a rotelle e mentre altri fattori esterni minavano la mia tranquillità. Di certo mi chiedo tuttora cosa tu abbia fatto al laboratorio di microonde visto che da quando ci sono entrato mi è accaduto di tutto nella vita. Ti considero un amico, è un piacere disquisire con te del più e del meno spaziando tra i più disparati argomenti quotidiani anche se provo un sentore di odio misto oppressione ogni volta che mi proponi delle malsane idee di lavoro. Grazie perché ancora oggi, a fine dottorato, mi vorresti accanto.

I più sentiti ringraziamenti alla Professoressa Caddemi e a Graziella. La prima perché ha instillato in me l'interesse verso l'elettronica delle microonde con la sua profonda maestria nei suoi insegnamenti. Ho avuto anche l'onore di passare un po' di tempo quotidiano con lei prima che lasciasse l'ateneo messinese e non potrò mai dimenticarlo. La seconda poiché ha mostrato la sua massima disponibilità, seppur non dovuta, quando bisognava prodigarsi affinché mi venisse concessa la possibilità di partecipare a questo percorso. Grazie perché credi in me.

Colei che mi ha partorito ancora sente il privilegio e l'onore di aver riverito l'Ingegnere quale sono. Si è presa cura dei vestiti da indossare e del cibo da gustare giornalmente a lavoro anche se questo ha implicato perdite immani di tempo a causa sua. Olio cosparso su tutti i sedili della macchina definendo tragitti lunghi e tortuosi fino al laboratorio, obbligando me a ripulire pozzanghere oleose in ogni dove. Posate perse nell'oblio di casa mia che mi hanno costretto ad improvvisare aggeggi fortuiti per cibarmi mentre mi trovavo in laboratorio. Grazie Madre.

Daniele, amico e fratello, è stato presente in uno dei momenti più topici della mia vita. Ha annichilito le 7 e più ore di fuso orario tra me e lui facendosene beffa quotidianamente. Compagno di viaggio vigile e volenteroso con cui ho potuto condividere sensazioni e gioie mentre coronavo il sogno di stare negli Stati Uniti d'America. In Texas, precisamente a Lubbock, tutti ti conoscono anche se non ti hanno mai visto. Dio ci ha uniti, grazie.

A dir poco indimenticabili i periodi all'estero, dal Texas alla Serbia. Ho incontrato persone meravigliose, imparato davvero tanto e vissuto momenti intensi superando qualsiasi aspettativa umana e terrena. Li ringrazio perché mi hanno fatto sentire a casa.

Grazie ai familiari, agli amici e a tutti coloro coinvolti nella Firedove che si sono interessati a me. Non posso nominarvi tutti altrimenti non ne usciamo più, ma grazie per esservi sincerati che il mio percorso stesse andando avanti e soprattutto grazie a coloro i quali, nell'invisibile e senza decantarlo, mi hanno sostenuto.

Ogni cosa grazie a Colui che si adopera attraverso il versetto citato in apertura perché nei dettagli si può comprendere quanto si è amati dal Signore.

Table of contents

Ringraziamenti ..... **I**

Table of contents ..... **III**

List of acronyms ..... **V**

List of tables ..... **IX**

List of figures ..... **X**

Introduction **1**

1 Radar systems **8**

1.1 Radar equation and main characteristics 8

1.2 Doppler radar 22

1.3 FMCW radar 35

1.4 MIMO radar 45

2 Radar board and data acquisition **54**

2.1 Radar by Infineon 54

2.2 Radar by Texas Instruments 59

2.3 Radar by Indie Semiconductor 62

2.4 Comparison of listed radars 66

3 Case studies **68**

3.1 Space and navigation 69

3.2 Design of a 120 GHz MIMO radar by combining SISO ICs 83

3.3 Enhanced phase detection..... 95

3.4 Gesture recognition..... 115

3.5 Breathing activity detection in real-time 128

3.6 Eye-blinking detection..... 136

Conclusions 153

References 155

List of publications 179

List of acronyms

(Alphabetic order)

AC	Alternating Current
ADAS	Advanced Driver-Assistance Systems
ADC	Analog-to-Digital Converter
AOA	Angle-Of-Arrival
AWGN	Additive White Gaussian Noise
BPM	Binary Phase Modulation
CA-CFAR	Cell-Average Constant False Alarm Rate
CADCA	Collision Avoidance Dynamic Critical Area
COTS	Commercial Off-The-Shelf
CPU	Central Process Unit
CW	Continuous Wave
DAC	Digital-to-Analog Converter
DC	Direct Current
DFT	Discrete Fourier Transform
DSP	Digital Signal Processor
EEG	Electroencephalography
EIRP	Effective Isotropic Radiated Power
EM	Electromagnetic
EOG	Electrooculography
ESA	European Space Agency
FCBGA	Flip-Chip Ball Grid Array

FDM	Frequency Division Multiplexing
FFT	Fast Fourier Transform
FMCW	Frequency-Modulated Continuous-Wave
FOV	Field-Of-View
FPGA	Field-Programmable Gate Array
GEO	Geostationary Orbit
HPBW	Half-Power Beamwidth
I/Q	In-phase and Quadrature
IC	Integrated Circuits
IEEE	Institute of Electrical and Electronics Engineers
IF	Intermediate Frequency
ISM	Industrial Scientific and Medical
JTFA	Joint Time-Frequency Analysis
LEO	Low-Earth Orbit
LNA	Low Noise Amplifier
LO	Local Oscillator
LOS	Line-Of-Sight
MCU	Microcontroller Unit
MDS	Minimum Detectable Signal
MIMO	Multiple-Input-Multiple-Output
MMIC	Monolithic Microwave Integrated Circuit
NF	Noise Figure
PC	Personal Computer
PCB	Printed Circuit Board

PhD	Philosophiae Doctor
PLL	Phase-Locked Loop
PPF	Polyphase Filter
PRF	Pulse Repetition Frequency
PRT	Pulse Repetition Time
QFN	Quad Flat No-leads
RADAR	Radio Detection and Ranging
RAM	Random Access Memory
RCS	Radar-Cross Section
RF	Radio Frequency
RFE	Radar Front End
RoHS	Restriction of Hazardous Substances
RRE	Radar Range Equation
RX	Receive
SAR	Synthetic Aperture Radar
SiGe	Silicon Germanium
SIMO	Single-Input-Multiple-Output
SISO	Single-Input-Single-Output
SNR	Signal-to-Noise-Ratio
SPI	Serial Peripheral Interface
STFT	Short-Time Fourier Transform
TDM	Time Division Multiplexing
TI	Texas Instruments
TSV	Tab Separated Values

TX	Transmit
USB	Universal Serial Bus
VCO	Voltage-Controlled Oscillator
VESPA	Vega Secondary Payload Adapter
VQFN	Very-thin-profile Quad Flat No-lead
WHO	World Health Organization
WWII	Second World War

List of tables

1.1	Electromagnetic spectrum sub-bands.	p. 11
1.2	Typical RCS values for several types of targets.	p. 18
2.1	Main features of the radar sensor systems used during the PhD activity.	p. 66
3.1	Technical requirements.	p. 77
3.2	Radar payload parameters.	p. 80
3.3	Effect of the distance variation on field-of-view and angular resolution.	p. 86

List of figures

1.1	Radar applications: (a) typical radar employed during WWII in England, (b) long-range radar in navigation systems and (c) recent application fields of radar.	p. 9
1.2	Antenna dimensions scale as a function of the frequency.	p. 11
1.3	Basic radar configurations: (a) bistatic and (b) monostatic.	p. 13
1.4	Plan position indicator used in navigation systems.	p. 14
1.5	Schematic illustration of the typical radar environment.	p. 16
1.6	Comparison of noise and P_{MDS} levels.	p. 20
1.7	Threshold detection example.	p. 21
1.8	Block diagram of a CW radar system architecture.	p. 24
1.9	Couples of sampled data translated in a target motion approaching and moving away from radar.	p. 27
1.10	Effect of an ambiguous velocity measurement.	p. 28
1.11	Phase variation that follows the approaching path of the target.	p. 29
1.12	Correction of the phase history by means of unwrapping.	p. 30
1.13	Detailed application of the STFT to a time-continuous, frequency-varying signal.	p. 34
1.14	Block diagram of an FMCW radar system architecture.	p. 36
1.15	Amplitude and frequency representation of a chirp over time.	p. 36
1.16	Sequence of transmitted (black curves) and received (blue curves) frequency pairs in the case of a stationary target. The beat frequency is the difference between them.	p. 38
1.17	Transmitted (black curve), received (black curves) and difference between transmitted and received frequency (red curves) for the case of multiple targets and (b) power-frequency spectrum of the related beat signals.	p. 40
1.18	Typical 2TX × 4RX MIMO radar architecture.	p. 46
1.19	Angle estimation with a simple SIMO radar.	p. 47
1.20	Example of physical array.	p. 50
1.21	Physical array (a) and corresponding virtual array (b).	p. 51
1.22	Example of a two-dimensional MIMO array.	p. 53

2.1	The internal block diagram of BGT24MTR11.	p. 55
2.2	Block diagram (a) and location of different building blocks on Sense2Go2 demo board (b).	p. 56
2.3	Picture of the in-house realized radar system.	p. 58
2.4	Functional block diagram.	p. 59
2.5	PCB antennas and virtual array.	p. 60
2.6	Integration of the mmWaveICBoost and the antenna module with IWR6843 chip.	p. 61
2.7	Block diagram (a) and location of the on-chip dipole antennas (b).	p. 62
2.8	Modular evaluation kit.	p. 64
2.9	A different radar system: the RFE board on the left, the FPGA and baseband amplifier on the right.	p. 65
3.1	Block diagram of the simulated scenario, including radar and channel models.	p. 72
3.2	Spectrum of the beat signal for the 24 GHz radar.	p. 73
3.3	Spectrum of the beat signal for the 60 GHz radar.	p. 74
3.4	Spectrum of the beat signal for the 77 GHz radar.	p. 74
3.5	Satellite approaching the VESPA with the help of the radar.	p. 77
3.6	Radar payload block diagram.	p. 78
3.7	SNR versus detection probability.	p. 82
3.8	Chips placement and its virtual array. The green squares are the transmitting antennas, the red circles identify the receiving ones. On the top left the tiny representation of the selected chip.	p. 87
3.9	Chips placement and its virtual array in case of the second chip rotation. The green squares are the transmitting antennas, the red circles identify the receiving ones.	p. 88
3.10	Main lobe width, grating lobes and side lobe level of both uniform arrays.	p. 90
3.11	First prototype layout of the MIMO radar system.	p. 92
3.12	Simulated target displacement (a) without and (b) with noise.	p. 97
3.13	Simulated I and Q channels during movement (blue) and stationary (red) intervals. In the inset, the enlarged detail of the stationary interval.	p. 98
3.14	Picture of the experimental setup.	p. 100

3.15 (a) First (blue solid line) and second (red dotted line) displacement from a stationary target and (b) difference between the two measurements. p. 101

3.16 (a) Reference signal (red dotted line) and measured displacements from an alternating moving target (blue solid line) and (b) difference between the two measurements. p. 102

3.17 (a) Elimination of incorrect displacement evaluation during stationary moments and (b) realignment of the entire motion. p. 104

3.18 Simulated displacement evaluation after the first part of the algorithm. p. 105

3.19 Displacement evaluation after the second step of the algorithm in the simulated scenario. p. 106

3.20 Target displacement in the real-world scenario. p. 107

3.21 Hand displacement after the application of the algorithm in the real scenario. p. 107

3.22 Phase samples collected in data blocks. p. 110

3.23 Wrong (blue solid line) and correct (red dotted line) displacement reconstruction. p. 111

3.24 First step of the proposed algorithm (a) and the related second step (b). p. 113

3.25 The displacement reconstruction by means of: offline measurement and elaboration (red dotted line), real-time measurement and offline procedure (blue solid line) and by real-time measurement and its ad-hoc processing algorithm (green dashed line). p. 114

3.26 Micro-Doppler signature and related chest displacement of a passenger on the rear seat. p. 118

3.27 Micro-Doppler signature of a driver falling asleep at the wheel. p. 119

3.28 Micro-Doppler signature concerning four couples of "next-song"/"previous-song" gestures. p. 120

3.29 Movement of fingers associated with the audio level. p. 121

3.30 Measured micro-Doppler signature (a) before and (b) after the I/Q imbalance correction in case of sound level adjustment. p. 122

3.31 Displacements measured related to different finger apertures: a) 0% to 100%, b) 0% to 100% to 20% to 100%. p. 123

3.32 Picture of the demo glasses equipped with the mm-wave radar. p. 125

3.33 Halt command: (a) displacement and (b) micro-Doppler signature. p. 125

3.34 Invite-to-move closer gesture: (a) displacement and (b) micro-Doppler signature. p. 126

3.35 Real-time chest displacement estimation during inhale/exhale activity. p. 128

3.36 Radar system and experiment setup. p. 129

3.37 Sketch of a simple pendulum. p. 130

3.38 Displacement (a) and frequency spectra (b) to evaluate the linearity of the system. p. 132

3.39 Displacement (a) and frequency spectra (b) to evaluate the sensitivity of the system. p. 133

3.40 Wrong (blue dashed line) and correct (red solid line) displacement reconstruction after the application of the optimized algorithm during a real-time measurement. p. 134

3.41 Thickness of some parts of the eyelid. p. 139

3.42 Simulated displacement (a) and micro-Doppler signature (b) due to the eye blinking. p. 140

3.43 Displacement (a) and micro-Doppler signature (b) due to the eye blinking during costal breathing. Whereas from (a) it is not possible to notice the eye blinking, it is clearly highlighted in (b). p. 142

3.44 Photograph of the glasses equipped with the mm-wave radar. p. 144

3.45 Radar test positions. p. 145

3.46 Micro-Doppler shift evaluation (a) and average of different measured micro-Doppler shifts for different radar positions (b). p. 145

3.47 I/Q signal (a), displacement (b) and micro-Doppler signature (c) due to the eye blinking during costal breathing. The measurement is performed with the radar placed on the glasses frame. p. 147

3.48 Head movements during eye blinking. p. 148

3.49 Eye-blinking micro-Doppler signature during random head movements. p. 149

3.50 Eye-blinking micro-Doppler signature during random wheelchair movements. p. 150

Introduction

In industrial, biomedical and automotive applications, RADAR (Radio Detection and Ranging) can be considered a disruptive technology. This statement is justified not only by the possibility of obtaining excellent performance both in terms of accuracy and spatial resolution, but also by the ability to detect parameters of interest without contact, drastically minimizing the size of the circuits and with minimal privacy concerns. Among the most relevant applicative examples in the context of use related to smart cities and industries, and in addition to the well-known ability of radars to measure distances and speeds of objects, it is possible to mention:

A. Detection of vital parameters, such as respiratory rate, heartbeat and eye blinking. Radar can also become a very powerful tool in the medical field not only for its ability to detect, for example, respiratory rate [1] and heartbeat [2] but also for a series of features that should not be underestimated such as, for example, the possibility of avoiding contact with the patient in order to make the hospitalization less invasive or the possibility of monitoring the rooms in which patients are staying in compliance with current regulations privacy; indeed the radar does not return images of the surrounding areas as it would happen using a video camera. For example, one of the key findings of the doctoral work is to enable communication with patients affected by neurodegenerative disorders by means of a radar system that detects eye blinking and reformulates them into a request from the patient [3], [4]. At the same time, healthcare sensing via radar is not only related to clinical environments, but it can change and help effectively with the daily life of people. For instance, in [5], the realization of a short-range radar system is presented to be mounted on a traditional white cane to assist people affected by blindness. Thus, this

contribution enables autonomous walking of visually impaired patients. Moreover, a multiple-input-multiple-output (MIMO) radar system, thanks to the presence of several antennas, would allow to monitor a fairly large environment both in terms of azimuth and elevation using only one radar. This aspect could be very beneficial for each mentioned application. For example, in a hospital room with several patients, a single radar would be enough to monitor the vital signs of each hospitalized person rather than the use of a radar for each patient; this would lead to the reduction of costs related to the introduction of this technology within the hospital and clinical world. In addition, the use of a MIMO radar in similar applications would allow continuous monitoring of all patients at the same time, even without medical staff close by.

B. Identification of gestures and movements of the human body that can be interpreted as commands or behaviors of interest. This gives the possibility to monitor the environment for obtain enhanced security and advanced infotainment systems. The gesture recognition finds fertile ground in the most diverse and nearly unimaginable applications. As an instance, in [6], the researchers introduce a human pose estimation and gesture recognition system with a parallel architecture using frequency-modulated continuous-wave (FMCW) radar for privacy compliance. Whereas, in [7], [8], the gesture recognition by radar is declared in two very different fields, music and metaverse, respectively. In detail, the latest is focused on the development of the next generation of interactive systems based on radar to support traditional camera-based sensors to provide an advanced, complete and reliable interaction among users. Differently, [9] introduces the concept of smart home or office employing radar to control the air conditioning and ventilation efficiently. At

the same time, the radar system is also exploited inside the car both to implement intelligent anti-abandon systems [10] and to develop infotainment control systems through simple gestures and movements. The latter would allow a clear decrease in the driver's loss of concentration while driving as well as increase the range of activities that can be carried out safely inside a means of transport [11], [12]. In this regard, a micro-Doppler analysis can be carried out that allows to highlight the simple gestures and movements of every single part of the body of humans. For example, in [11], micro-Doppler analysis is used to determine specific movements of the human head that indicate a level of fatigue such that the act of driving is compromised and dangerous while, in [12], with this analysis it can be observed how certain gestures detected by the radar can translate into particular functions such as, for example, increasing or lowering the volume of the radio allowing a more immediate and safe interaction with the machine. Thus, the importance of developing inattentive driving behavior detection based on radar sensors is confirmed in [13] too. Indeed, monitoring driver’s attentiveness is crucial for obtaining higher transportation safety. Precisely, this contribution places emphasis on how the combination of radar and machine learning can classify the gestures correctly.

C. Automation of some tasks in several applications is very popular nowadays and radars play an important role like, as an example, in the automotive sector where one of the main focuses is on autonomous driving. In [14], new ways of radar installation are investigated with respect to the standards adopted until today by car manufacturers. Thus, a medium-range radar was designed to be placed on the rear lamp rather than behind the bumpers or in the car body, ensuring undisturbed view and better protection from disturbances and accidents. Differently, in [15], the

feasibility of a short-range ship collision avoidance radar system has been investigated. Indeed, ships are usually equipped with long-range radars for the open-see navigation, whereas the in-harbor one relies only on the manual ability of the captain. Therefore, this contribution paves the way for enabling the concept of autonomous ship navigation by exploiting radar sensors. Another example of autonomous task is the implementation of a radar system to be mounted on a satellite to detect space debris as in [16]. The goal is to assist satellites to approach and collect debris because space junk has become an emerging issue over the last decade. This work represents the preliminary work of an on-satellite radar system.

Thus, in recent decades, the number of applications related to radar systems has increased exponentially due to the high ductility of these systems. From automotive to meteorology, from military defense to ship traffic control, from industrial security to the medical field, the applications in which radar becomes the main protagonist of technologically complex and advanced systems are among the most diverse. Initially, radar systems were used exclusively to detect objects and their distance, but today, they are also used for their ability to estimate speed and millimeter displacements relative to the targets of interest for the application. Moreover, the possibility of using multiple radars, operating at different frequencies, by combining their data leads to a growing scientific and industrial interest in accurately monitoring the surrounding scenario.

This philosophiae doctor (PhD) thesis deepens and expands the study of microwave and millimeter-wave radar for advanced applications of high scientific and industrial/commercial interest in the fields of vital signs detection, motion analysis and gesture recognition. The use of radar in space and airport navigation will also be discussed. A large section is dedicated to enabling communication with patients suffering from neurodegenerative disorders using radar

systems. In particular, continuous wave (CW) radars that exploit Doppler effect, FMCW and MIMO techniques will be used, depending on the specific case. First and foremost, the dissertation aims to provide an overview of advanced and portable radar systems.

Considering the increasing degree of miniaturization and the required advanced performance of modern electronic devices, the evolution of radar systems is a topic of great scientific interest. Thus, a study of scientific literature has been carried out in the context of major critical issues related to radar systems. This is evidenced by the growing demand for radar systems working at increasingly higher frequencies, given that the size of the components decreases as the operating frequency increases, and that they have better performance. The latter are strongly linked to the use of higher bandwidths and the presence of more antennas, both in transmission and reception, within the radar system. The use of wider bands requires the use of devices operating at higher and higher frequencies since they are, in part, not yet allocated for other applications. As a result, it was decided to work with radars working at different frequencies to identify the most suitable radar for each type of application under consideration. Therefore, in order to minimize size and improve performance, especially in terms of accuracy and spatial resolution, microwave (24 GHz) and millimeter-wave (60 GHz - 80 GHz and 110 GHz -130 GHz) front ends are used, operating in different modes such as continuous wave radars or frequency-modulated radars. In particular, the potential of radars operating in the 110 GHz - 130 GHz frequency range is still little explored given the complexity of these systems and, moreover, such high frequencies still represent a world that is little explored for the field of electronics. Using this frequency range increases the complexity of the hardware and makes it more complicated to analyze the results during processing.

The present thesis aims to improve the performance of these radar systems and, therefore, to face and overcome the current challenges present in the literature and to develop applications

of relevance for the territory and for the national and international scene. Initially, the main critical issues in the radar field will be addressed, such as, for example, in-phase and quadrature (I/Q) imbalance, phase detection, displacement evaluation during real-time measurement, advanced micro-Doppler signature elaboration and angle-of-arrival (AOA) estimation in the field-of-view (FOV) of the selected MIMO radar.

Subsequently, all the radars employed during the doctoral study will be presented to analyze their characteristics and to compare them before showing all the accomplished results.

In addition, this thesis paves the way for developing a modular 120 GHz MIMO radar composed of multiple single-input-single-output (SISO) integrated circuits (IC) chips, allowing the detection of the so-called angle-of-arrival. Several antennas make up the MIMO radar and their better positioning in transmission and reception areas is the most relevant critical issue that has been addressed during the doctorate program.

Considering the application areas indicated above, post-processing techniques will be used to identify the different types of targets and to appropriately process the data according to the results pertinent to the application under consideration. All the problems emerging from the study of the results obtained will be analyzed to find new solutions applicable in the elaboration phase in such a way as to avoid the addition of hardware for solving them. Once the devices to be used have been identified, we will move on to the manufacture of more complex radar systems with a particular focus on systems with the ability to detect angle-of-arrival.

The possibility of improving and customizing the processing phase of the data obtained from the measurements according to the expected results and the individual aspects of greatest scientific interest for the individual application has not been overlooked. In fact, another objective is to significantly diversify the entire post-processing phase in order to optimize it for each specific case.

After this brief examination, we can assert that although the radar area has seen a very strong qualitative and quantitative increase in the scientific literature produced, there are numerous challenges to be overcome both in the technological and signal processing fields. The very structure of modern radar systems, consisting of microwave and millimeter-wave front ends, analog signal conditioning sections, conversion and digital processing of the measured data, underlines the complexity of the research field.

This doctorate thesis fits perfectly into the renewed current and future industrial context where the development of the related enabling technologies is of fundamental importance for the evolution of society. Additionally, the highly innovative nature of the technologies covered by this dissertation encourages entrepreneurial and patent activity.

The present thesis is organized into three chapters. In Chapter 1, the main characteristics of radar systems are discussed, and an overview of radar topologies is drawn. Chapter 2 makes a list of the employed radar boards summarizing their features and comparing them to connect the radar theory with all case studies for short-range applications shown in Chapter 3, in detail. Finally, the conclusions are drawn and a glance at some future directions and possibilities in terms of research developments is explored. During the three-year PhD there was the opportunity to work on different topics beyond microwave and mm-wave radars. The related results and achievements are reported in the list of publications at the end of the thesis.

1 Radar systems

As seen in the Introduction, the possible radar applications are numerous, and it is impossible to comprehend all of them in a simple list. This assertion is enhanced by the continuously increasing number of new applications throughout different fields. This aspect has allowed a decrease in the price of radars in the last decades, increasing the radar's performance contextually. In this chapter, the main radar operating principles and topologies are discussed, explaining the basic concepts and going deeper into the most relevant aspects for the PhD work.

1.1 Radar equation and main characteristics

A radar is defined as an electronic system that, through the transmission and reception of electromagnetic waves, allows the determination of the position at which objects are located and their speed within a monitored scenario. More accurately, the radar system also allows the detection of the direction at which the target in question is located, its shape and its size, as well as giving the possibility of estimating the so-called angle of arrival.

Radar was patented in the early twentieth century and, in particular, England was the first nation to exploit the radar system as a defense mechanism against air attacks and for the detection of enemy ships during the Second World War (WWII), as shown in Fig. 1.1(a).

Subsequently, radar was no longer used only for war purposes but also in the meteorological field to locate atmospheric disturbances and assess their intensity or, for example, for air and naval traffic control in anti-collision systems up to, today, the automotive and medical sectors as briefly replicated for example purposes in Fig. 1.1(b) and 1.1(c).

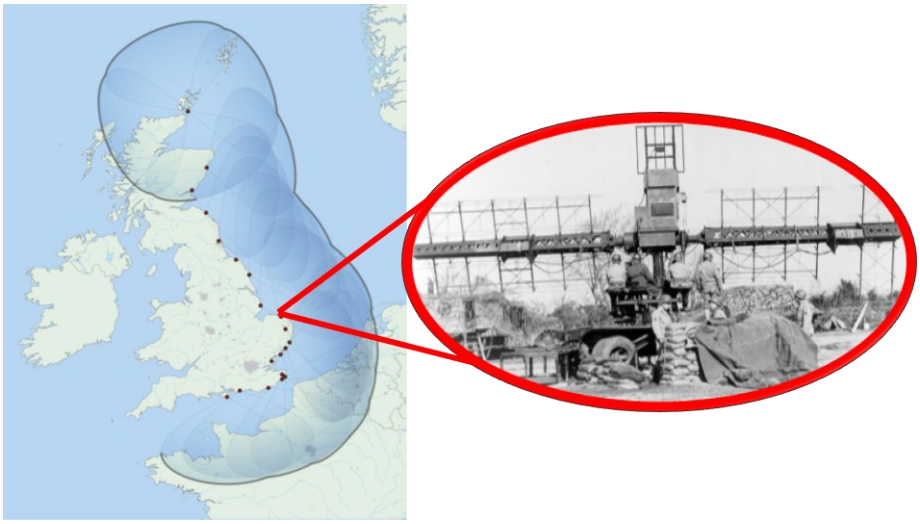

(a)

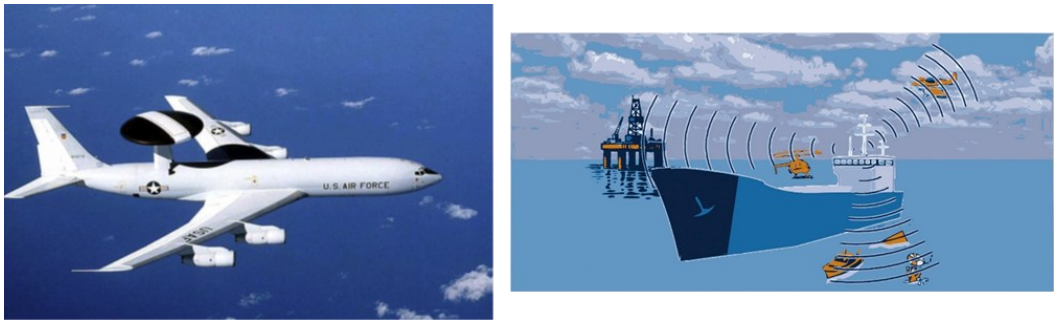

(b)

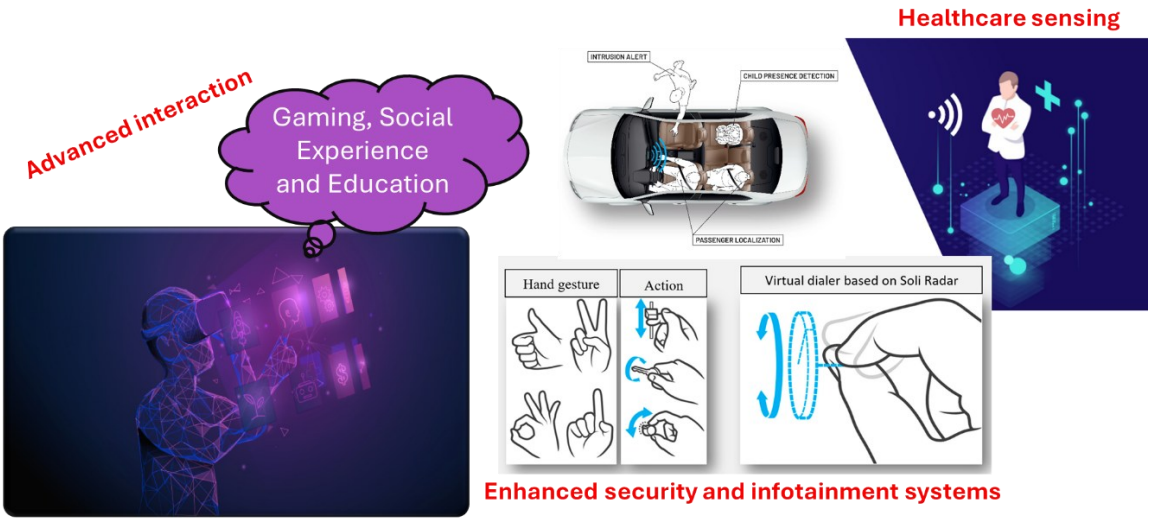

(c)

Fig. 1.1: Radar applications: (a) typical radar employed during WWII in England, (b) long-range radar in navigation systems and (c) recent application fields of radar.

Microwave frequencies range from 3 GHz to 300 GHz, between radio and infrared waves. Radars operate within this same frequency range. All of the radars used in this work are portable, i.e., their dimensions are relatively small. This is due to their operating frequencies being very close to and within the mm-waves bandwidth, which is conventionally defined as 30 GHz to 300 GHz [17].

Though the higher frequencies make the design of microwave devices and systems tricky, as listed hereafter, they bring several advantages which are exploited by short-range radar applications:

- The gain of the antennas is proportional to their electrical size. Since the higher the frequency, the smaller the wavelength, at higher frequencies for the same physical size, the antenna looks electrically bigger, increasing the gain. In other words, the higher the frequency, the higher the directivity.
- In the upper range of the microwave frequencies, there is more available bandwidth due to the lack of additional applications [18]. As a consequence, more bandwidth is provided, and this is beneficial to obtain better performance in radar applications.
- The target radar cross-section (RCS) is proportional to its electrical size. Using an electromagnetic wave characterized by a smaller wavelength makes the target even more “detectable”.
- Again, the higher the frequency the smaller the antenna dimensions, thus the more compact and lightweight systems can be realized which are considered portable as is shown in Fig. 1.2.

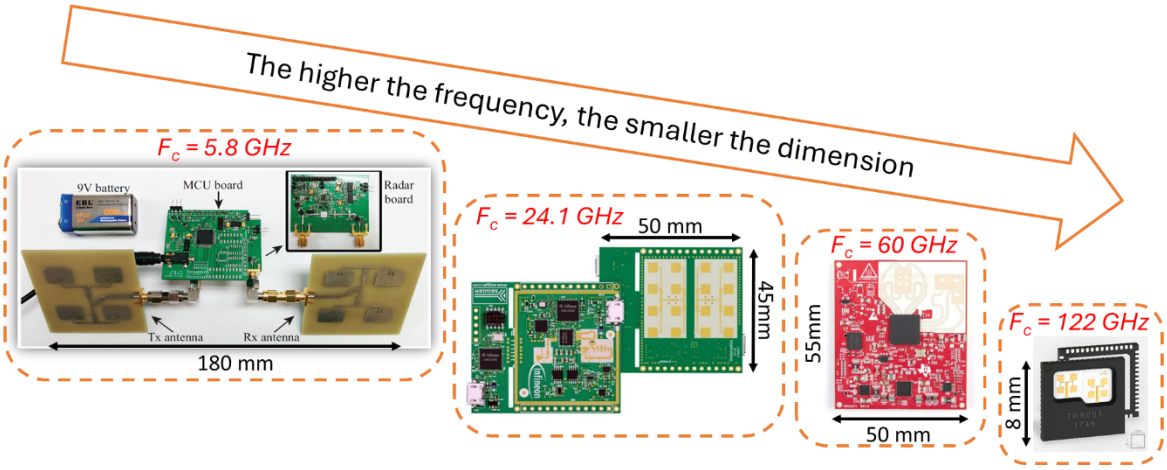

Fig. 1.2: Antenna dimensions scale as a function of the frequency.

The electromagnetic (EM) spectrum is divided into sub-bands depending on the frequency. Mnemonic letters are associated with each band to make professional reference to a specific bandwidth easier, according to the Institute of Electrical and Electronics Engineers (IEEE) classification reported in Tab. 1.1.

Tab. 1.1: Electromagnetic spectrum sub-bands.

IEEE sub-band mnemonic letters	Sub-band frequency range
Medium frequency	300 kHz – 3 MHz
HF	3 MHz – 30 MHz
VHF	30 MHz – 300 MHz
UHF	300 MHz – 1 GHz
L	1 GHz – 2 GHz
S	2 GHz – 4 GHz
C	4 GHz – 8 GHz
X	8 GHz – 12 GHz
K_u	12 GHz – 18 GHz
K	18 GHz – 27 GHz

K_a	27 GHz – 40 GHz
V	40 GHz – 75 GHz
W	75 GHz – 110 GHz
F	90 GHz – 140 GHz
D	110 GHz – 170 GHz
Y	325 GHz – 500 GHz

The L band is mainly used for navigation, mobile phones, and military applications. The S band is used for navigation beacons and wireless networks. The C band is used for long-distance telecommunications due to its ability to penetrate clouds, dust, and rain. The X band is used for radar and space communications. The K_u band is used for satellite communications. The K band and K_a band are used for satellite communications, astronomical observations, and radar. The V band is used for high-capacity terrestrial millimeter-wave communication and radar. Automotive radars currently operate in the K and W bands, around 24 GHz and 77 GHz, respectively, whereas industrial radars operate at approximately 60 GHz within the V band. The radars used during the doctorate operate in the three different bands: K, V and D, which will be discussed later.

Basically, the mode of operation of any radar can be divided into simple steps. Initially, the radar sends an electromagnetic wave towards the monitored scenario by means of a transmitting chain that generates and transmits the signal by exploiting an antenna. If a target is present, the signal bounces off the object and is reflected back to the radar. The reflected electromagnetic wave is received and converted into a current signal by a receiving antenna and amplified and filtered by the receiver. Simplifying, the signal can be elaborated to discern the difference, in terms of magnitude, frequency and phase primarily, between the transmitted signal and the received one. Exploiting these differences, it is possible to extract the distance and the velocity

of the target, its dimension and angular position with respect to the location of the radar itself. Therefore, the antennas play an important role because they are considered the eyes of the radar sensor system. There are two basic antenna configurations of radar systems: monostatic and bistatic, as illustrated in Fig. 1.3.

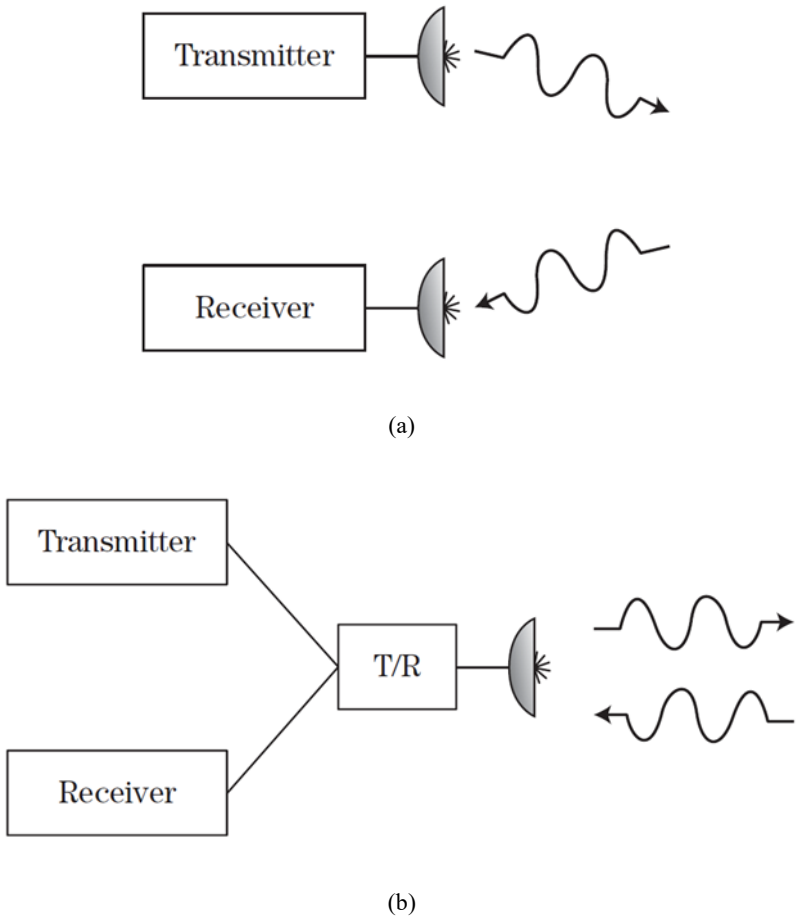

Fig. 1.3: Basic radar configurations: (a) bistatic and (b) monostatic.

In a monostatic configuration, one antenna serves as both the transmitter and receiver. In contrast, bistatic configurations have separate antennas for the transmitting and receiving radar functions. Nevertheless, the use of two antennas alone does not determine whether a system is monostatic or bistatic. If the two antennas are very close together, the system is considered to be monostatic. A system is bistatic only if the two antennas are sufficiently separated such that the angles or ranges to the target differ significantly.

The transmitter is a relatively high-power device, whereas the receiver is very sensitive. High-power EM waves from the transmitter, if introduced directly into the receiver, would prevent the detection of targets (self-jamming) and could damage the receiver's components. Therefore, the receiver should be isolated from the transmitter. A bistatic radar configuration can provide significant isolation. While most modern radars are monostatic for more practical design and operations, it is more difficult to provide isolation between the transmitter and receiver. Consequently, circulators and switches (duplexers) can be used to separate transmit (TX) and receive (RX) signals.

Moreover, radars can be noncoherent or coherent. Whereas a noncoherent system detects only the amplitude of the received signal, the coherent system detects both amplitude and phase. Noncoherent systems are cheaper and often used to provide a two-dimensional display of target location in a ground map background. The amplitude of the signal at any instant in time will determine the brightness of the corresponding area of the radar map, as shown in Fig. 1.4, where the beam indicates where the radar is pointing at a particular moment and the green filled circles indicate the locations of the detected targets during scanning.

Fig. 1.4: Plan position indicator used in navigation systems.

All early radars were noncoherent and target detection depended on the operator's skill to discern targets from the surrounding environment. In coherent systems, the additional phase

information provides target motion characteristics and the ability to image a target. Though there are still applications of noncoherent radars, most modern radars are coherent. Indeed, all the radars employed during the research activity are coherent systems.

Radar performance dramatically depends on the level of the received echo. However, at the receiver's input, in addition to the signal of interest, noise is received likewise. When a signal is received, the so-called echo, a combination of noise and signal is present. The noise obstacles the target detection and, in radar field, consists mainly of thermal noise and is due to the random thermal motion of charged particles. In addition, the receiver section generates its own internal noise, which usually dominates over the noise from the environment. Noise is not correlated with the target signal, so the total power is just the sum of the signal power and the noise one. To properly ensure the detection of the targets, it is fundamental to refer to the signal-to-noise ratio (SNR); in fact, if this parameter is relatively high, the probability of detecting the target is higher. Radar system designers use an equation to compute the SNR at the receiver, namely the radar range equation (RRE), which is a relatively simple equation that considers all the parameters affecting the power budget. The RRE can also be exploited to determine the maximum range at which a particular radar can detect a target, but it can also serve as a means for understanding the factors affecting radar performance and how to select the best radar components for a particular application.

In Fig. 1.5, there is a sketched representation of the typical radar environment where the emphasis is placed on the single contributions, in the channel section, that can decrease the SNR of the entire radar system.

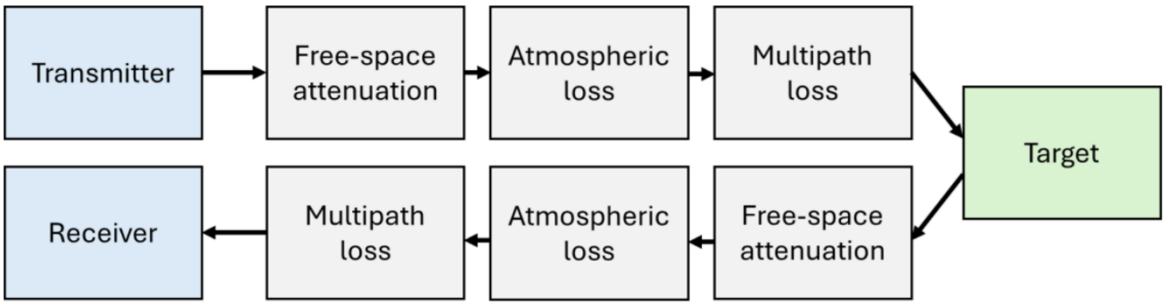

Fig. 1.5: Schematic illustration of the typical radar environment.

Considering the first line of the schematic illustration, the power at the target P_{target} can be expressed as in Eq. 1.1:

$$P_{target} = P_{TX} \cdot \frac{G_t A_{fs}}{L_t} \tag{1.1}$$

where:

- P_{TX} is the transmitted power.
- G_t is the transmitting antenna gain.
- A_{fs} is the free space attenuation.
- L_t is the sum of atmospheric and multipath loss, i.e., the propagation of a wave from one point to another by more than one path.

In detail, multipath loss is the process by which a transmitted signal arrives at the receiver via at least two different paths. These paths are typically the main direct path, and at least one reflected path. Depending on the phase, the signals may combine constructively or destructively, resulting in a signal that is either stronger or weaker than the one would be in free space.

Regarding the free space attenuation shown in Eq. 1.1, in turn, it can be calculated as highlighted in Eq. 1.2:

$$A_{fs} = \frac{\lambda^2}{(4\pi R)^2} \tag{1.2}$$

where:

- R is the target range intended as line-of-sight distance.
- λ is the wavelength.

When the EM wave hits the target, it is reflected in many directions. The target behaves as if it were a source of EM waves itself, because the incident EM signal induces time-varying currents [19]. Consequently, the power reflected and captured by the radar is influenced not only by the target, but also by the channel again. The target contribution, G_{target}, is inferior to unity and can be expressed as in Eq. 1.3:

$$G_{target} = \frac{4\pi\sigma_t}{\lambda^2} \tag{1.3}$$

where σ_t is the target radar cross-section that is a measure of power scattered in a given spatial direction when a target is illuminated by an incident wave. The radar cross-section is used to characterize the target regardless of the transmitter and receiver topology and the distance between radar and target itself. Indeed, the RCS value is normalized by the power density of the incident wave at the target, thus, it is independent of the distance. The RCS depends on several parameters such as the physical size, the geometric shape and the material composition of the target and it is expressed in square meters m^2. It is worth noting that the RCS depends on the frequency and, thus wavelength, because scattering mechanisms depend on the size of the scattering body relative to the wavelength. In general, if the target can be approximated to a

sphere or a cylinder, RCS should be expected to increase with decreasing wavelength up to a wavelength in the millimeter-wave region. In general, the larger the target physical sizes, the higher the radar cross-section. Typical values of RCS can span 10^{-5} m^2 for insects to 10^{+6} m^2 for large ships. Due to the large dynamic range, a logarithmic power scale is often used with reference value of σ_{sphere} = 1 m^2. In Tab. 1.2, some radar cross-section values are reported, by way of example.

Tab. 1.2: Typical RCS values for several types of targets.

Targets	RCS (m^2)	RCS (dB)
Container ship	10000	40
Jumbo jet	100	20
Small truck	100	20
Jet airliner	20 – 40	13 – 16
Cabin cruiser	10	10
Large fighter	6	7.8
Helicopter	3	4.7
Four-passenger jet	2	3
Man	1	0
Stealth jet	0.1 – 0.01	-10 – -20
Birds	0.001	-30
Insects	0.00001	-50

Therefore, RCS is quite difficult to estimate, and it is normally determined by measurements. Indeed, although it equals the target cross-sectional area theoretically, not all reflected energy is distributed in all directions, and some energy is absorbed.

Clarifying the three main contributions in the typical radar environment beyond the transmitting power and considering both A_{fs} and L_t two times due to the round-trip path of the electromagnetic wave, the previous equations can be combined to obtain the expression of the power at the radar receiver in Eq. 1.4.

$$P_{RX} = P_{TX} \cdot \left[\frac{G_{TX} \cdot G_{RX} \cdot \lambda^2 \cdot \sigma_t}{(4\pi)^3 \cdot R^4 \cdot L_s} \right] \tag{1.4}$$

where:

- L_s are the square losses due to the round-trip path.
- G_{TX} and G_{RX} are the transmitting and receiving antenna gains respectively.

Therefore, the power received is a function of the system specifications, the type of targets and channel attenuation. A radar engineer cannot change either the transmit/receive channel, or the target characteristics. However, a radar engineer can exploit the RRE to select and design the best radar components to fulfil the desired application. For this purpose, often the RRE is written in a particular form to highlight the maximum distance detectable by the radar sensor, considering the so-called minimum discernible signal power, P_{MDS}, as shown in Eq. 1.5.

$$R_{max} = \sqrt[4]{P_{tx} \cdot \left[\frac{G^2 \cdot \lambda^2 \cdot \sigma_t}{(4\pi)^3 \cdot P_{MDS} \cdot L_s} \right]} \tag{1.5}$$

This parameter indicates how sensitive the radar is, in fact, it represents the minimum power detectable by the radar and its value is generally 3 dB higher than the average noise level as can be seen from Fig. 1.6. Receiving signals that have power lower than the P_{MDS} cannot be picked up by radar, eliminating the possibility of detecting a given target because the signal is immersed in the noise which is mix of thermal noise, receiver noise limited by the receiver

bandwidth, and might also include air or ground clutter echoes from objects which are of no interest for the radar application, electromagnetic interference from other non-intentional EM sources (television stations, cellular telephones), and hostile intentional jamming. The signals received from these different noise sources are modeled as additive random processes. Thus, the target echo is entirely deterministic, the combined target-plus-interference signal is a random process [19].

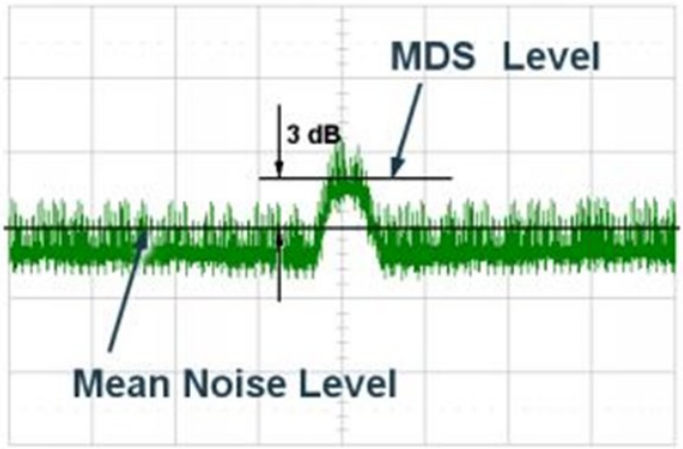

Fig. 1.6: Comparison of noise and P_{MDS} levels.

Typical radar values of the P_{MDS} echo span range from -80 dBm to -113 dBm. Eq. 1.5 is exploited to calculate the maximum range detectable and, of course, depends on the SNR at the receiver that, in turn, depends on the characteristics of the receiver itself. In order to increase the R_{max}, it is generally preferable to increase the gain of the antennas or improve the sensitivity of the receiver section in terms of a lower noise figure, rather than increase the transmitted power. Indeed, due to the fourth root, e.g., to simply double the maximum range, it is required to increase the transmitted power by a 16 factor, which is very expensive. Therefore, it is usually most convenient to increase the antenna gain or decrease the noise figure of the receiver.

All these reasons confirm that the target detection is a very complicated task. Basically, a target can be detected by setting the threshold at least 3 dB above the noise level and below the

signal level related to the target itself. Any echoes above the threshold are assumed to be the targets, instead of signals under the threshold, which are ignored. The thresholding detection procedure is illustrated in Fig. 1.7. In detail, any signal or each data sample in the digital domain is compared to a threshold. If the sample overcomes the threshold, it is supposed to be due to the presence of the target plus the interference, as in sample 50 in Fig. 1.7; otherwise, it is supposed to be due only to the interference. The choice of words "it is supposed to be" is not casual, because the assumption can be wrong. Indeed, should a peak due to a strong inference cross the threshold, this will lead to a false alarm. This is the case of sample 20 in Fig. 1.7.

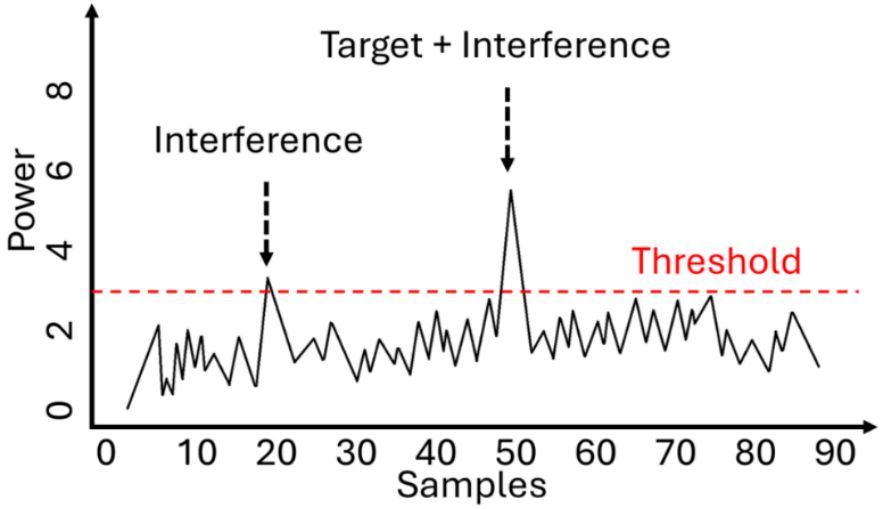

Fig. 1.7: Threshold detection example.

Consequently, increasing the value of the threshold in turn decreases the probability of false alarm. On the other hand, a sample coming from a weak echo cannot overcome the threshold and thus it is undetectable. For this reason, a trade-off should be selected according to the specific application. Indisputably, increasing the SNR by reducing the noise power is a key point. Another possible solution exploits dynamic thresholds based on different principles reported in the literature [19], [20], [21]. A very famous example is the cell-average constant false alarm rate (CA-CFAR) detector, which is based on tracking the main level of interference to dynamically set the threshold with a fixed probability of false alarm.

1.2 Doppler radar

The radar transmits an electromagnetic signal and can receive a reflected signal from the object. Based on the time delay of the received signal, the radar can measure the range of the object. If the object is moving, the frequency of the received signal will be shifted from the frequency of the transmitted signal, known as the Doppler effect. The Doppler frequency shift is determined by the radial velocity of the moving object, that is, the velocity component in the direction of the radar line of sight (LOS). Based on the Doppler frequency shift of the received signal, radar can measure the radial velocity of the moving object. If the object or any structural component of the object has an oscillatory motion in addition to the bulk motion of the object, the oscillation will induce an additional frequency modulation on the reflected signal and generate sidebands about the conventional Doppler shifted frequency caused by the translational motion of the object. The additional Doppler modulation is called the micro-Doppler effect [22]. The main goal of CW radar is to measure the speed of a target and its diverse speed components if the target is performing a complex movement. Doppler radars are not used for range measurement because they lack the timing mark. Considering a monostatic radar where the transmitter and receiver are at the same location and do not move and supposing a target is moving in the radar's FOV with a radial velocity component, v, in the direction of the radar. The theory of special relativity affirms that the frequency f_r of the received echo will differ from the transmitted or carrier frequency f_c due to the Doppler effect as highlighted in Eq. 1.6 where c is the speed of light.

$$f_r = f_c \left(\frac{1 + \frac{v}{c}}{1 - \frac{v}{c}} \right) \tag{1.6}$$

It is worth noting that if the target is approaching the radar, the received frequency increases; otherwise, if the target is moving away from the radar, the received frequency decreases. A parallel can be drawn for the case of sound waves, when the sound from moving ambulance sirens or train whistles appears distorted for a subject stationary or moving at different speed. Therefore, Doppler shifts can be exploited in radar systems to detect echoes from moving targets in the presence of much stronger reflections from stationary clutters and, thus, to separate moving from stationary targets. The difference f_D between the transmitted and received frequencies is called the Doppler frequency or Doppler shift and can be calculated as in Eq. 1.7.

$$f_D = \pm f_c \left(\frac{2v}{c} \cos\theta \right) \tag{1.7}$$

where θ is the angle between the velocity vector of the target and the radar LOS, so the $\cos\theta$ contribute gives the radial velocity component. Of course, if the target is exactly in the LOS ($\theta = 0°$), then the radial velocity is simply v. The Doppler shift is zero if the target is stationary or when the target is crossing orthogonally to the radar boresight ($\theta = \pi/2$). Therefore, Eq. 1.7 confirms that the Doppler frequency shift is proportional to the emitted frequency f_c of the wave source and the relative velocity v between the source and the observer. A typical block diagram of a CW radar sensor is illustrated in Fig. 1.8.

Basically, a local oscillator in the transmitting section generates a single-tone frequency signal that is contemporary divided into two parts: the first half is sent to the receiving section for future demodulation by means of a splitter and the second half is radiated by the transmitting antenna after amplification and filtering.

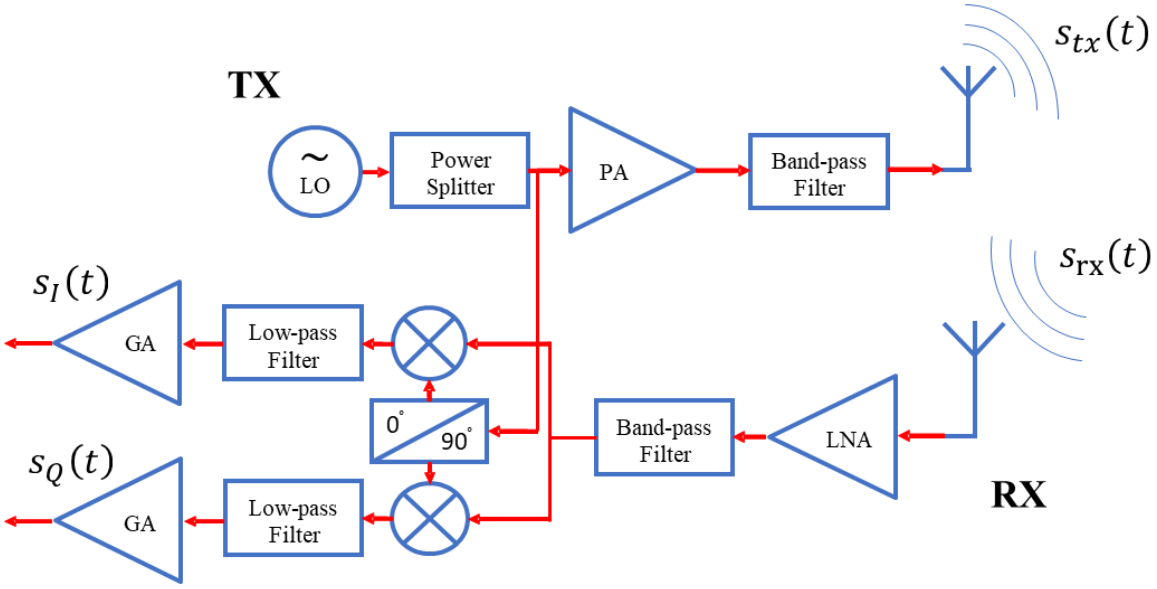

Fig. 1.8: Block diagram of a CW radar system architecture.

Later, the reflected signal is captured by the antenna in the receiving section. The first element of the receiving channel is the low-noise amplifier (LNA) since the echo signal is weak and, thus, it is essential to increase the noise figure as little as possible. This amplifier category is characterized by the introduction of very little noise during the amplification phase of the received signal, therefore, the LNA will be the first element to be inserted in the reception chain to keep the cascaded system noise figure low [17].

The intention is to measure the displacement of the target and its movement direction. In Fig. 1.8, the quadrature mixer positioned after the band-pass filter in the receiving, known as I/Q detector, exploits a two-channel quadrature receiver to split the incoming signal into two channels, enabling the estimation of target direction in addition to the speed detection. This concept will be explained better in the following pages. The mixers are 3-port devices with 2 inputs, the transmitted signal generated by local oscillator and the received one, and one output whose frequency is directly related to the Doppler shift. Neglecting the mixer non-linearities and considering the low-pass filters at the output of the mixers, the output signal is characterized by a frequency equal to the difference between the frequencies of the two inputs and a phase

equal to the phase difference between the phase of the two inputs. The upper channel signal is mixed with a cosine reference, instead of the lower channel mixed with a sinusoid reference. The lower oscillator is therefore 90° out of phase with the upper one, a condition referred to as being in quadrature. They are typically exploited by coherent receivers, to obtain both modules and phases of the received signals. In mathematical terms, the transmitted signal originated by the local oscillator can be expressed as in Eq. 1.8:

$$s_{tx}(t) = \mathrm{A} \cdot \cos(2\pi f_c t) \tag{1.8}$$

where:

- f_c is the carrier/operative frequency.
- A is the signal amplitude.

If at least one target is present in the scenario, the transmitted signal will be reflected and captured by the receiving antenna. The received signal can be expressed as in Eq. 1.9:

$$s_{\mathrm{rx}}(t) = \alpha \cdot \cos\left(2\,\pi\, f_{\mathrm{c}} \left(t - \frac{2d(t)}{c}\right) + \phi_0\right) \tag{1.9}$$

where:

- α is the received signal amplitude considering the path loss, the radar cross-section of the target and the circuit gain and loss.
- $2d(t)/c$ is the time delay due to the target range.
- ϕ_0 is the residual phase that is negligible in a coherent system [23].

Equation 1.9, in other words, is the delayed and scaled version of the transmitted signal. The delay is due to the range of the target. Considering the delay as the sum of starting distance plus the distance shift, the received signal can be rearranged as reported in Eq. 1.10:

$$s_{\mathrm{rx}}(t) = \alpha \cdot \cos\left(2\,\pi\, f_c t + \frac{4\,\pi R_0}{\lambda} \pm \frac{4\,\pi x(t)}{\lambda} + \phi_0\right) \tag{1.10}$$

where:

- R_0 is the starting detection distance of the target.
- $x(t)$ is the time-varying distance shift due to the moving target.

Given the quadrature receiver as shown in Fig. 1.10, the received signal is divided into the in-phase I channel, Eq. 1.11, and quadrature Q channel, Eq. 1.12, components:

$$s_I(t) = \alpha \cdot \cos\left(\Delta\varphi \pm \frac{4\pi\ \cdot x(t)}{\lambda}\right) \tag{1.11}$$

$$s_Q(t) = \alpha \cdot \sin\left(\Delta\varphi \pm \frac{4\pi\ \cdot x(t)}{\lambda}\right) \tag{1.12}$$

in which $\Delta\varphi$ is the phase component resulting from the round-trip distance R_0. Therefore, the quadrature receiver in Fig. 1.10 allows to exploit the complex nature of the received signal to detect not only speed and small displacements, but also the target movement direction. In other words, the quadrature mixer enables understanding of whether the target is moving toward or away from the radar. The phase variation is estimated through the arctangent operator, as frequently occurs in the scientific community [24]. Therefore, the arctangent operator is applied on the in-quadrature part over the in-phase part of raw data as it is expressed in Eq. 1.13.

$$\varphi(t) = tan^{-1}\left(\frac{s_Q(t)}{s_I(t)}\right) = \Delta\varphi \pm \frac{4\pi x(t)}{\lambda} \tag{1.13}$$

Since $\Delta\varphi$ is constant and useless for the instantaneous phase extraction, it is usually removed by subtracting the average value. The arctangent operator has been chosen to eliminate the optimum/null detection point problem by combining the I and Q signals [24], [25].

Thus, each measured data (I/Q couple) has a single absolute phase $\varphi(t)$ in which the in-phase signal represents the real part of the corresponding complex signal, instead of the quadrature signal which represents the imaginary part of the complex signal. To measure the displacement (or speed, it is considered equivalent), two measured data are needed. If the phase difference between a phase sample and the subsequent one is greater than zero radians, then the target is approaching the radar. If the phase difference is lower than zero radians, then the target is moving away from the radar, as remarked in Fig. 1.9. In other words, the phase difference suggests the motion direction.

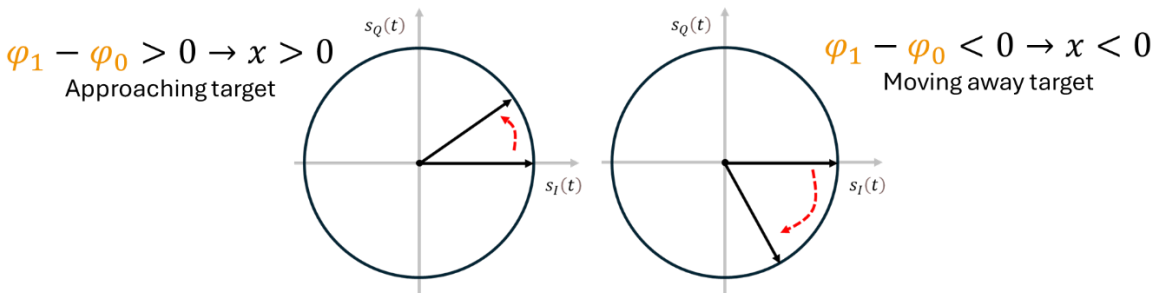

Fig. 1.9: Couples of sampled data translated in a target motion approaching and moving away from radar.

The measurement of the displacement is unambiguous only if the phase change between two consecutive samples (I/Q couples) received from the selected target is less than π. It is important to point out that a phase variation may be equal to or higher than π, but this would produce an incorrect result since a target movement towards or away from the radar will generate ambiguity. Therefore, just to clarify, Fig. 1.10 shows the location of two simulated consecutive samples on a constellation graph during an ambiguous movement, i.e., when the real phase variation is larger than π.

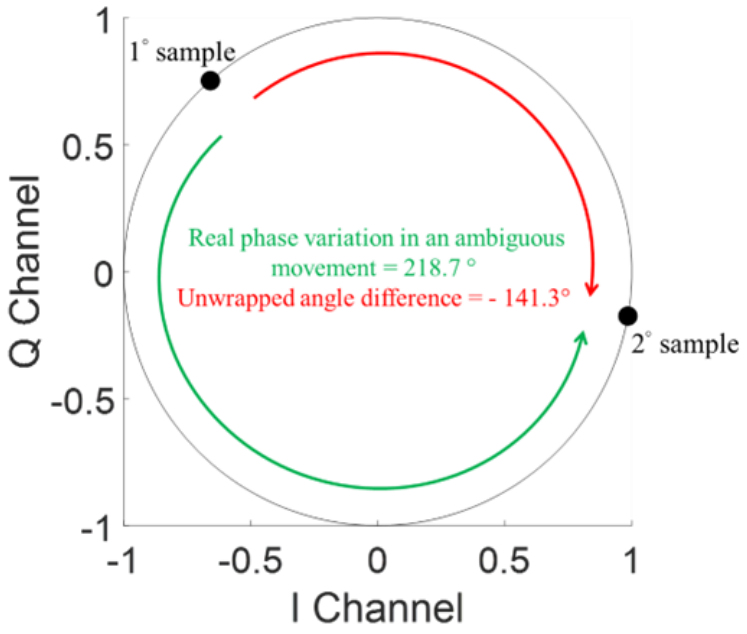

Fig. 1.10: Effect of an ambiguous velocity measurement.

Although the correct movement is the one indicated by the green arrow, the unwrap function, explained soon after Eq. 1.15, returns an angle difference of $-141.3°$, thus considering the wrong direction (red arrow). Therefore, the unwrapping operation cannot resolve the ambiguity due to exceeding phase variation and, thus, the π-limit translates into a maximum measurable displacement in Eq. 1.14 between two samples:

$$x(t)_{max} = \frac{\lambda}{4} \tag{1.14}$$

This expression directly imposes a maximum measurable velocity that could be trivially derived from Eq. 1.14, divided by T_m, which is the time interval between two measurements, as underlined in Eq. 1.15, and depends on the type of radar system, i.e., CW or FMCW. Indeed, all these considerations are valid for both radar types, regardless of whether or not modulation is present. In any case, to accurately track the phase variation of the radar received signal, the radar transmitter must be driven by a highly stable frequency source to maintain full phase coherency.

$$v(t) = \frac{x(t)}{T_m} \tag{1.15}$$

As a consequence, the radar performance must match the maximum velocity of the objects within the monitored scenario; otherwise, an intrinsic error occurs during the data processing. On the other hand, the absolute phase can exceed the limit of $\pm\pi$ because of the target motion in the same direction, i.e., phase accumulation; in other words, when the total phase history is not enclosed within the interval $[-\pi; \pi]$ as the reported example in Fig. 1.11. A phase variation of a target moving in the same direction along the entire measurement is shown in Fig. 1.11. The π threshold is not overtaken by exceeding the speed limit, but due to the natural change of the phase (displacement), which can increase or decrease without any limit during the measurement; instead, the phase of a single sample can take a value between $-\pi$ and π. We need to "unwrap" the phase.

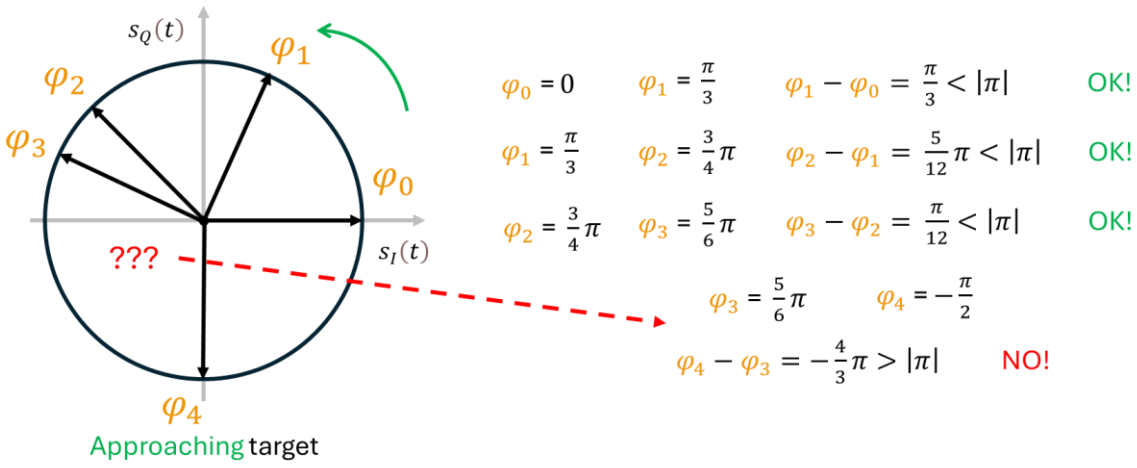

Fig. 1.11: Phase variation that follows the approaching path of the target.

This is a different case from that due to velocity ambiguity and can be solved by unwrapping the phase. Indeed, in these cases, the ambiguity actually does not exist because the target speed

is under the maximum velocity and the great difference between two consecutive phase values is due only to the accumulated phase. To summarize, the unwrap function works as follows:

- If the phase variation is equal to or greater than π, the unwrap function adds multiples of -2π until the jump is less than π.
- If the phase variation is equal to or less than $-\pi$, the unwrap function adds multiples of 2π until the jump is greater than $-\pi$.

Consequently, the unwrap function resolves the possible phase ambiguity and permits to extend the phase history values in order to correctly reconstruct the target motion for extents larger than the 2π limit. Thus, the unwrapping operation permits to reconstruct the phase variation in Fig. 1.11 properly, as shown in Fig. 1.12.

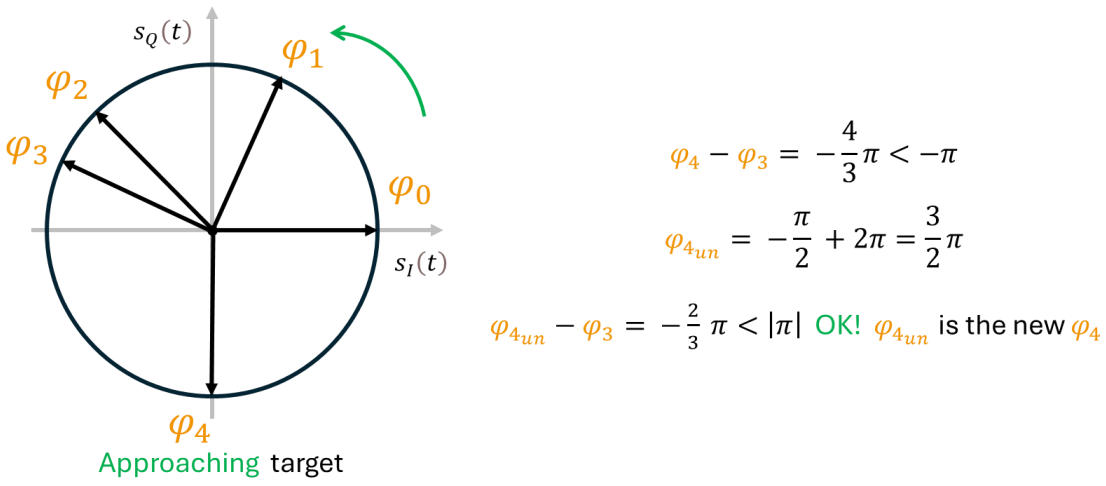

Fig. 1.12: Correction of the phase history by means of unwrapping.

In summary, for two different reasons, an absolute phase jump equal to or greater than π could be produced:

- The first is due to the speed of the object in case of velocity exceeding the threshold, as discussed previously. In this case, the unwrap function makes an intrinsic error that cannot

be prevented because the radar itself cannot detect the target regardless of elaboration methods.

- The second is due to the phase history related to the target motion during measurement, i.e., in case of movement in the same direction exceeding the $[-\pi;\pi]$ limit. Indeed, the phase increases or decreases continuously without exceeding the speed limit and the phase unwrapping algorithm between a reconstructed value produced by phase history and the new one works properly.

Recalling Eq. 1.11, 1.12 and 1.7 in case of $\theta = 0°$ and considering simply that the velocity is the displacement by the time, Eq. 1.16 and 1.17 highlight the information about the target speed within the I/Q signals.

$$s_I(t) = \alpha \cdot \cos\left(\Delta\varphi \pm \frac{4\pi \cdot v \cdot t}{\lambda}\right) \tag{1.16}$$

$$s_Q(t) = \alpha \cdot \sin\left(\Delta\varphi \pm \frac{4\pi \cdot v \cdot t}{\lambda}\right) \tag{1.17}$$

The two expressions of I/Q signals are equivalent, indeed, if a target is moving, then it has a speed v. Moreover, a linear phase variation is translated at a constant speed, which makes sense by analyzing the phase. In fact, an identical angular phase rotation can correspond to positive or negative phase shifts involving positive or negative speeds, respectively. A complex-valued signal can be formed from the I and Q signals as written in Eq. 1.18.

$$s_b(t) = s_I(t) + js_Q(t) = e^{j\left(\Delta\varphi \pm \frac{4\pi \cdot v \cdot t}{\lambda}\right)} = e^{j(\Delta\varphi \pm 2\pi f_D t)} \tag{1.18}$$

The frequency content of a time-domain signal is analyzed by calculating its Fourier transform resulting in a frequency-domain representation, a spectrum, of the time-domain

signal. The Fourier transform applied to Eq. 1.18 results in a Dirac delta function centered in the Doppler shift frequency as expressed by Eq. 1.19.

$$s_b(f) = e^{j(\Delta\varphi)}\delta_D(f - f_D) \tag{1.19}$$

Thus, the Doppler frequency shift is usually measured in the frequency domain by taking the Fourier transform of the received signal. In the Fourier spectrum, the peak component indicates the Doppler frequency shift induced by the radial velocity of the object. Contextually, the speed of the target is proportional to the Doppler frequency shift as already mentioned in Eq. 1.7. In the processing units, the transform is calculated by discrete Fourier transform (DFT), which is usually implemented in the form of the fast Fourier transform (FFT). Setting a long observation time, the speed resolution is improving, which is, of course, related to the frequency resolution of the FFT.

In terms of displacement and Doppler detection, the phase analysis considers the target to be either a single point or a parallel plane. However, in many cases, the target should be considered a rigid or non-rigid body. Each subcomponent moves independently, requiring a different kind of analysis. A rigid body has a finite size and each subcomponent moves without deformation. In other words, the distance between any two points on the body remains constant during movement. A non-rigid body, however, is deformable, thus changing its shape. In fact, treating the target as a rigid body is an idealization, but it simplifies the analysis compared to the case of non-rigid bodies [22]. The term micro-Doppler signature refers to a distinctive expression of the target movement in terms of Doppler components, and it is represented in Doppler domain by means of a joint time-frequency analysis (JTFA) which is a technique used to analyze how the frequency content of a signal changes over time. Since it is related to a specific characteristic of the target, it can be exploited for object identification, movement analysis and similar

purposes. In fact, the term “micro” refers to a large class of cases such as target oscillations, vibrations, rotations, swinging and flapping of small extents. The micro-Doppler effect can be used to determine kinematic properties of an object. For instance, in Eq. 1.20 a relationship is reported to calculate the maximum Doppler frequency shift if the target is vibrating with a D_v and f_v vibration amplitude and frequency, respectively [22].

$$max\{f_D\} = \frac{2}{\lambda} f_v D_v \tag{1.20}$$

It is worth noting that Eq. 1.20 implies that even in systems characterized by both low vibration rate and amplitude, employing microwave or millimeter-wave radars, thus with very small wavelength, is very beneficial to detect the Doppler shifts induced by motion. Since the micro-Doppler effect is sensitive to the product $1/\lambda$, a radar engineer could operate at higher frequencies to observe tiny movements of the target, e.g., vibrations.

As will be discussed in the third chapter, human body movement analysis is an important topic benefiting from micro-Doppler research. Of course, it is also a complex field due to the complex human motion, due to the articulation and deformability of the body. Hence, the micro-Doppler effect observed in the radar received signal from an object can be characterized as its signature. Thus, the micro-Doppler signature is the distinctive characteristic of the object that represents the intricate frequency modulation generated from the structural components of the object and represented in the joint time and Doppler frequency domain. The radar architecture required to measure the time-varying frequency shift is the same employed for Doppler radars, but the required signal processing is different. Indeed, even though the Fourier transform is a great tool to analyze the frequency behavior of the target, it is not suitable for measuring time-varying frequency features. Hence, FFT is not suitable for this purpose because it lacks time-dependent frequency information as it is applied to the entire signal.

On the other hand, the short-time Fourier transform (STFT) is used to compute the instantaneous frequencies for each harmonic component, thus displaying the spectral density of time-varying signals with a spectrogram. The spectrogram is calculated by STFT, which is necessary to estimate how the frequency content of the signal changes over time. It is represented by the squared magnitude of the STFT, most of the time in decibels. The STFT is applied on the down-converted signal to recognize the characteristic micro-Doppler signature resulting from different micromovements [26]. The STFT of a signal is computed by sliding a window of a fixed length over the signal and by computing the FFT on every single part of the windowed signal as elucidated in Fig. 1.13.

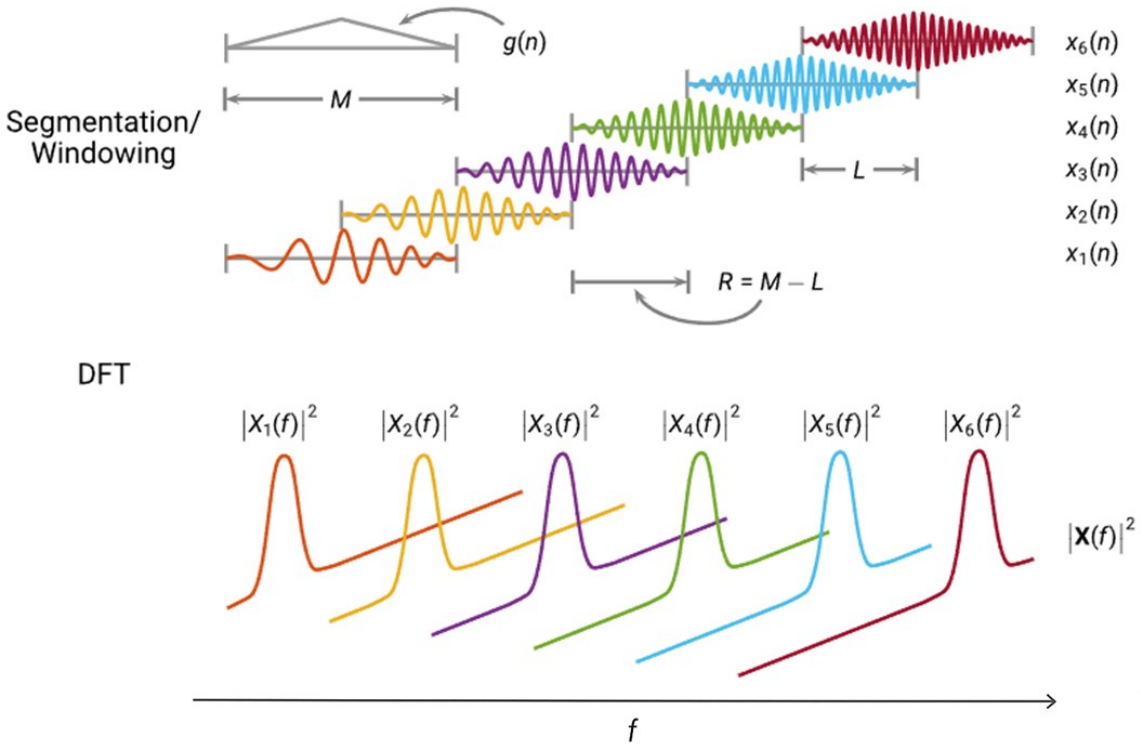

Fig. 1.13: Detailed application of the STFT to a time-continuous, frequency-varying signal.

Specifically, during the STFT processing, a limited time-window of size M is considered instead of the entire measuring time as occurs in case of FFT. Thus, the signal is partitioned into many segments according to the selected window typology and the windowed data are

overlapped by an L-quantity at the edges to ensure a better spectrum reconstruction. The algorithm adds a complex value in a matrix for each windowed signal; thus, each value is characterized by magnitude and phase for each point in time and frequency. The length of the window, M, is a key parameter to set both the time and the frequency resolution. The longer the window size, the finer the frequency resolution but the poorer the time resolution. Instead, a reduced window is the better choice if the analysis is focused above all on the frequency variations over time. Therefore, a short window permits to capture the temporal instant in which the Doppler frequency of the signal has been changed. A radar engineer must find a trade-off between frequency and time, playing on different parameters like window type, window length, number of FFT points, overlap length of consecutive windows and so on; it depends on the purpose of every application. In fact, the third chapter will discuss a deep analysis of micro-Doppler signatures derived by applying the STFT algorithm properly.

1.3 FMCW radar

The next step is to estimate the distance to the target and its speed by taking advantage of continuous wave radars and introducing frequency modulation, thus talking about frequency-modulated continuous wave radars. The range measurement is related to an additional frequency measurement due to the modulation. In fact, the main difference in the diagram block with respect to the CW schematic is the presence of a chirp generator instead of a simple local oscillator, as evidenced by Fig. 1.14. In this basic architecture, there are only some adjustments for the cutoff frequency of the filters and the VCO input is not a constant voltage as in CW radar, but it is a sawtooth signal.

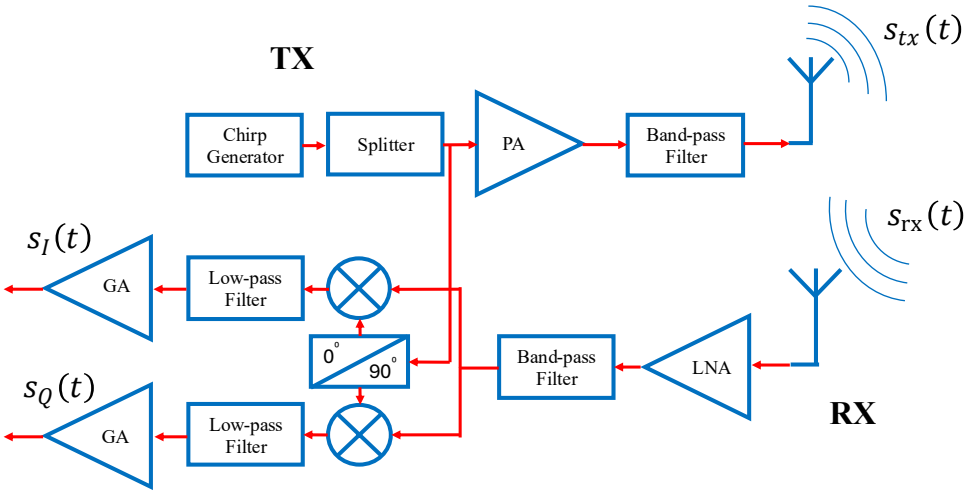

Fig. 1.14: Block diagram of an FMCW radar system architecture.

A frequency-modulated continuous wave radar transmits a series of signals called chirps. A chirp is a sinusoidal signal whose frequency changes over time. It is possible to employ different modulation waveforms, which can result in performance changes [27]. The sawtooth waveform is one of the most frequently used types of modulating signals and it has been used during the doctorate, as will be discussed in the third chapter. In Fig. 1.15, a signal that is linearly modulated by a sawtooth waveform is shown in both an amplitude versus time plot and a frequency versus time plot, which is a convenient way to represent the time evolution of a chirp.

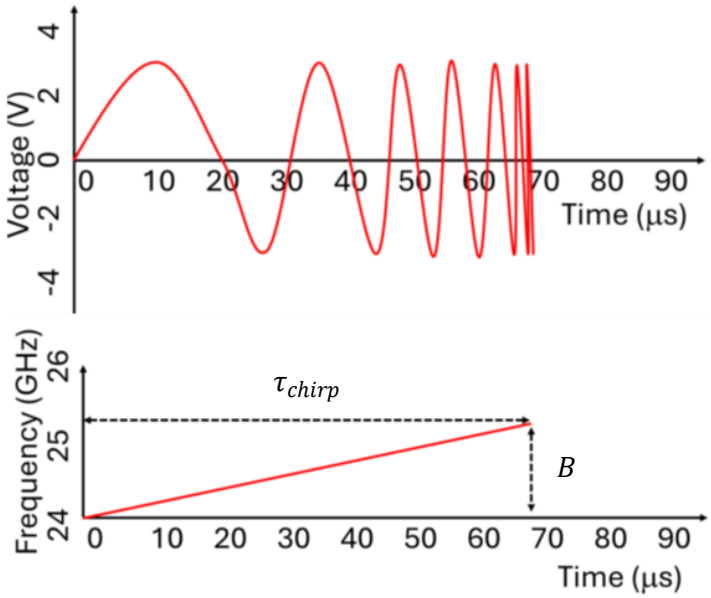

Fig. 1.15: Amplitude and frequency representation of a chirp over time.

Given the modulation bandwidth B and time duration τ_{chirp} of the chirp, the slope S of the chirp, written in Eq. 1.21, is defined as the rate at which it ramps up.

$$S = \frac{B}{\tau_{chirp}} \tag{1.21}$$

Thus, the transmitted signal $s_{tx}(t)$ can be expressed as in Eq. 1.22.

$$s_{tx}(t) = \mathrm{A} \cdot \cos\left(2\pi f_c t + \pi \frac{B}{\tau_{chirp}} t^2 + \phi_0\right) \tag{1.22}$$

where:

- t is the so-called "fast time".
- f_c is the operative frequency.
- ϕ_0 is the residual phase and is neglected as for the case of Doppler radar.
- A is the amplitude of the signal.

Simplifying the amplitude as unitary, the instantaneous frequency can be calculated from the derivative of the cosine argument in Eq. 1.22 and expressed as in Eq. 1.23.

$$f_T(t) = f_c + \frac{B}{\tau_{chirp}} t \tag{1.23}$$

If at least one target is present in the scenario, even if stationary, the transmitted signal will be reflected and captured by the receiving antenna. The received signal can be expressed as in Eq. 1.24.

$$s_{rx}(t) = \alpha \cdot \cos\left(2\,\pi\, f_c\,(t - t_d) + \,\pi\,\frac{B}{\tau_{chirp}}\,(t - t_d)^2\right) \tag{1.24}$$

in which α is the amplitude factor considering the path loss, the radar cross-section of the target and the circuit gain/loss that it will be neglected later. Therefore, the received signal is the delayed and scaled version of the transmitted one and can be rearranged as in Eq. 1.25.

$$s_{rx}(t) = \cos\left(2\pi \frac{B}{\tau_{chirp}} t \cdot t_d + 2\pi f_c t_d\right) \tag{1.25}$$

in which t_d is the round-trip time that can be separated into two terms as shown in Eq. 1.26.

$$t_d = \frac{2\big(R + x(\tau)\big)}{c} \tag{1.26}$$

Thus, the value of t_d depends on the distance of the target R and the time-varying distance shift $x(\tau)$ which has been extensively discussed in the paragraph dedicated to CW radar. However, from this point forward, the symbol R will indicate the entire distance between the target and the radar. The transmitted/received signal pairs are graphically shown in Fig. 1.16, where a single stationary target is represented.

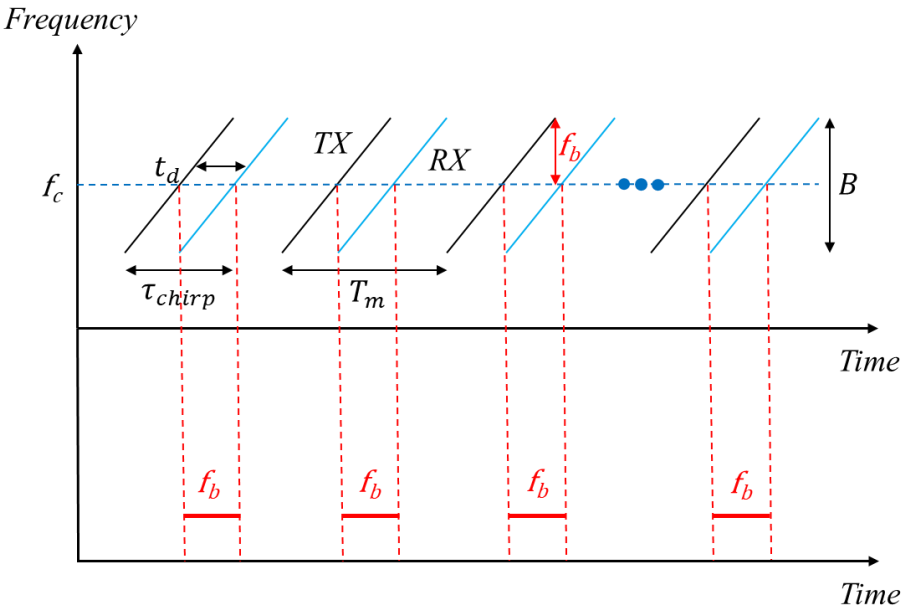

Fig. 1.16: Sequence of transmitted (black curves) and received (blue curves) frequency pairs in the case of a stationary target. The beat frequency is the difference between them.

In fact, typical FMCW configuration consists of a sequence of chirps followed by idle time, which is the difference between measurement time and chirp duration. In turn, chirp sequences are often packaged into groups called frames. The data samples are elaborated in these frames to reduce the computational load. It is interesting to observe that the beat frequency f_b is obtained as the frequency difference between the frequency of the transmitted signal by that of the received one.

Moving the received signal right is equivalent to having a more distant target, whereas moving the blue curve left is equivalent to having a nearer target. In other words, for an FMCW radar, measuring the range is equivalent to measuring the frequency difference f_b, because f_b is directly proportional to the target range according to Eq. 1.27.

$$f_b(t) = \frac{2R \cdot B}{\tau_{chirp} \cdot c} \rightarrow R = \frac{c \cdot \tau_{chirp} \cdot f_b}{2B} \tag{1.27}$$

Multiple objects in front of the radar involve multiple reflected chirps at the RX antenna. A frequency spectrum of the beat signal, typically performed by means of an FFT, will reveal multiple tones. The frequency of each tone is proportional to the distance of the corresponding object from the radar.

A graphical view of this case is shown in Fig. 1.17 where the frequency vs. time and the spectrum of the beat signals are represented. Figure 1.17 recalls that multiple targets can be present in the same scenario and their range separation will be required. The output of the mixer is characterized by beat signals from the time the first echo is received until the current chirp is transmitted.

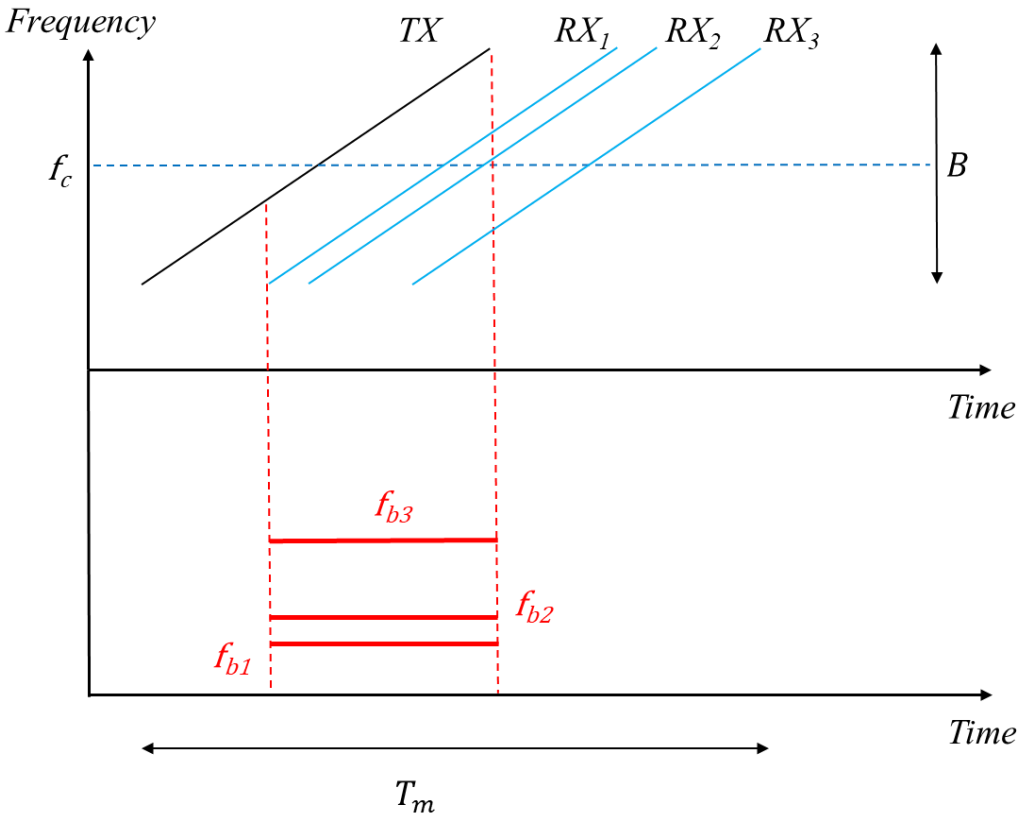

(a)

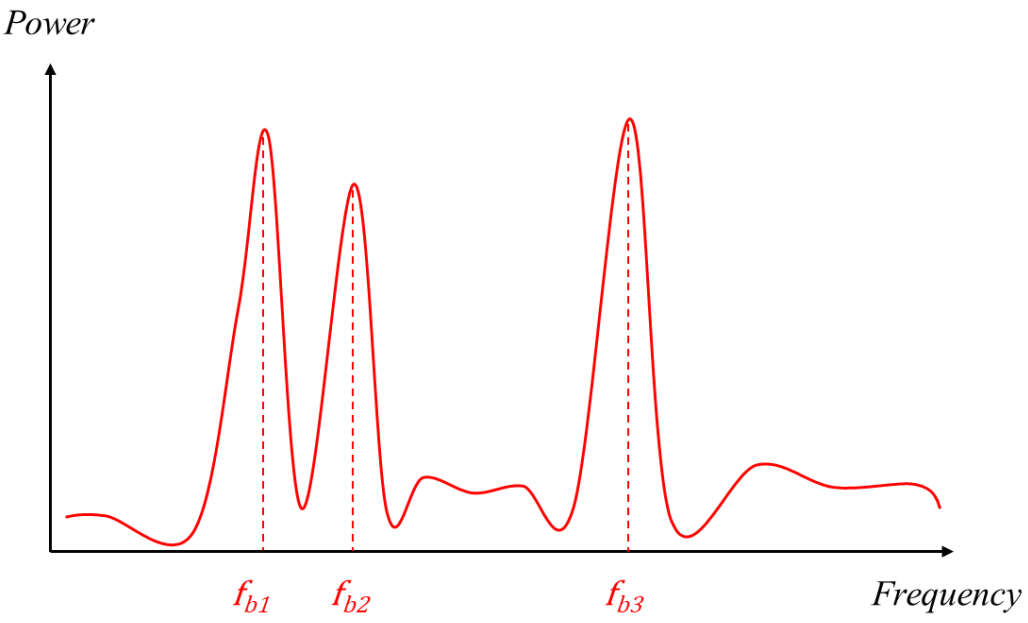

(b)

Fig. 1.17: Transmitted (black curve), received (black curves) and difference between transmitted and received frequency (red curves) for the case of multiple targets and (b) power-frequency spectrum of the related beat signals.

The range resolution is the radar ability to separate two targets in the same scenario which are closely spaced. Analyzing the range resolution is very important to understand what the minimum distance between two targets is to allow their separation, i.e., the two targets are not detected as a single target. The range resolution expression is in Eq. 1.28.

$$\delta_R = \frac{c}{2B} \tag{1.28}$$

Clearly, higher bandwidth means better resolution. Thus, increasing bandwidth is very beneficial for radar engineers. Recalling the concepts expressed in the introduction, it is evident the necessity to move to higher operative frequencies for having a larger bandwidth. If the range resolution is not good enough, two single targets are detected as a single target.

On the other hand, the range accuracy is the radar capability to measure the correct range of the target. According to [28], the radar accuracy can be calculated by exploiting Eq. 1.29.

$$\sigma_R = \frac{c}{3.6B \cdot \sqrt[2]{2SNR}} \tag{1.29}$$

Comparing Eq. 1.28 and 1.29, it is worth noting that accuracy is a fraction of the range resolution and, for a fixed range resolution, it can be improved by increasing the SNR. If the accuracy is not good enough, the difference between measured and true range value is excessive.

For FMCW short range radars, the maximum detectable range may be imposed not by the radar range equation, but by the radar parameters themselves such as the modulation bandwidth, chirp duration and the sampling frequency set during the conversion of the beat signal through the analog-to-digital converter (ADC) located after the gain amplifiers in the radar architecture, as in Fig. 1.14. This is a direct consequence of digitally analyzing radar returns, which are usually acquired using an ADC. Since the range detection relies on a frequency measurement,

the maximum detectable range R_{MAX}, in turn, depends on the maximum detectable frequency $f_{b_{MAX}}$, which is limited by the sampling frequency f_s in a digital system according to the Shannon-Nyquist theorem, i.e., $f_{b_{MAX}} < f_s/2$.

Thus, Eq. 1.27 can be elaborated in Eq. 1.30 to highlight the relation between maximum detectable distance and the radar parameters.

$$R_{MAX} = \frac{f_s \cdot c \cdot \tau_{chirp}}{4B} \tag{1.30}$$

Thus, the maximum unambiguous range is finally defined by the maximum beat frequency that the receiver system can measure.

Reformulating the previous equations, the in-phase and quadrature components are derived here too in Eq. 1.31 and 1.32.

$$s_I(t) = \cos\left(2\pi f_b t + \frac{4\pi f_c \cdot x(\tau)}{c}\right) \tag{1.31}$$

$$s_Q(t) = \sin\left(2\pi f_b t + \frac{4\pi f_c \cdot x(\tau)}{c}\right) \tag{1.32}$$

The first term of both equations is the beat frequency, which is used to extract the distance of the target as already indicated and illustrated, in Eq. 1.27 and Fig. 1.16, respectively. The same considerations made in the previous section for the phase analysis are drawn for the second term. As for the case of Doppler radars, the phase of the received signal can be exploited to extract the target displacement $x(\tau)$, i.e., the distance traveled by the target within the time duration between two consecutive transmit chirps. The only important difference is that T_m is the time interval between two measurements including, this time, the duration of the chirp τ_{chirp} and the inter-chirp time. In detail, the term T_m is usually called pulse repetition time (PRT) and

indicates the inter-chirp period, i.e., the time between the start of two consecutive chirps and its inverse, the so-called pulse repetition frequency (PRF), indicates the chirp rate. This aspect imposes a more restricted limitation on the maximum detectable velocity because T_m, in case of CW radar, is only the sampling time ideally.

Whereas in FMCW radars, the speed detection is based on the effective temporal distance between consecutive chirps, so the higher the time between chirps, the lower the maximum detectable target speed. This is one of the main disadvantages of CW radar with or without modulation. Besides, the measurement is unambiguous only if the phase change between two chirps of the selected target is less than π, like in Doppler radar. As a consequence, the maximum calculable displacement is a quarter of a wavelength as in CW radar; instead the maximum detectable velocity is expressed in Eq. 1.33.

$$v_{MAX} = \frac{\lambda}{4PRT} \tag{1.33}$$

It is worth noting that, according to Eq. 1.30, increasing the chirp duration increases the radar maximum range, but from Eq. 1.33 it decreases the maximum speed. For an FMCW radar, evaluating speed resolution is very important. Indeed, if multiple targets with the same range but different speeds are present in the scenario, they can be resolved only if the speed resolution δ_v is enough as written in Eq. 1.34 assuming the idle time as null.

$$\delta_v = \frac{\lambda}{2M\tau_{chirp}} \tag{1.34}$$

in which M is the number of chirps in a frame. As for the case of the range accuracy, the speed accuracy is a fraction of the velocity resolution and depends on the SNR as can be observed in Eq. 1.35.

$$\sigma_R = \frac{c}{3.6M\tau_{chirp} \cdot \sqrt[2]{2SNR}} \tag{1.35}$$

The more the number of chirps within a frame, the better the speed resolution and accuracy. From a computational point of view, the range throughout the time is calculated by applying the FFT on each chirp and the result is subsequently stored in a row/column of a matrix. The time domain within a chirp is usually referred to as fast time. In fact, the term "fast" refers to the short duration of a single chirp compared to the time interval between measurements, which is usually equal to the PRT. Sequences of chirps fill a data matrix and the time domain across multiple chirps is referred to as slow time because the PRF is much lower than the sampling rate in range. The data matrix is the so-called range profile.

Again, another frequency domain analysis can be performed to highlight the frequency peaks corresponding to the target speed. Therefore, a second FFT is applied on the range profile, that is one FFT for each column/row of the matrix. In other words, the second FFT is applied to the opposite dimension from the first. The first FFT reveals the distances of the targets and the second, performed across different chirps, reveals their velocities, obtaining the so-called range-Doppler map. Thus, a 2D FFT can be directly implemented to obtain range and Doppler information within milliseconds, which is an essential requirement for real-time applications that require a high update rate and low latency.

In summary, fast FMCW radars can detect the range of objects by measuring the frequency shift of a single received chirp. If the target is moving, the beat frequency will change slightly, but this shift is too small to be noticed in the frequency spectrum. By analyzing the phase of the received signal, the range shift of the target and, consequently, its speed can be obtained.

In conclusion, the FMCW radar enables the estimation of both the range and the velocity of target beyond the phase history reconstruction. The application of the first FFT inside every

chirp serves for the calculation of the range. The second FFT is applied within the frames, i.e., among the chirps, to track phase variations between them. This exploits the radar's sensitivity to calculate velocity and range shifts/displacements. Therefore, FMCW provides more information about the targets, but has a lower maximum detectable speed than Doppler radar. As always, a trade-off is necessary, and the most suitable radar depends on the application and monitored environment.

1.4 MIMO radar

Even though FMCW radars enable the possibility to a more detailed description of the targets in the examined scenario than Doppler radars, only the MIMO radars can estimate the target precise location thanks to their capability of measuring the AOA, i.e., angle of arrival, of the received echoes in the azimuth and elevation planes. The main additional characteristics of MIMO radars rely on peculiar hardware architectures that, as the acronym suggests, involve multiple transmitting and receiving sections, transmitting orthogonal waveforms. Other options for measuring the AOA include mechanically scanning the antenna or electronically scanning the antennas. These differ from the MIMO radar in that the direction of the main lobe of the radiation pattern is fixed. A typical architecture of a MIMO radar equipped with two transmitters and four receivers is sketched in Fig. 1.18. Each transmitting channel requires frequency multiplication and amplification stages, as well as the corresponding antenna. Different receiving stages are responsible for amplifying and down converting the received signal. The processing unit is typically responsible for generating the required transmitted waveform and processing the down-converted signals. The reason for using multiple transmitters and receivers will become clearer.

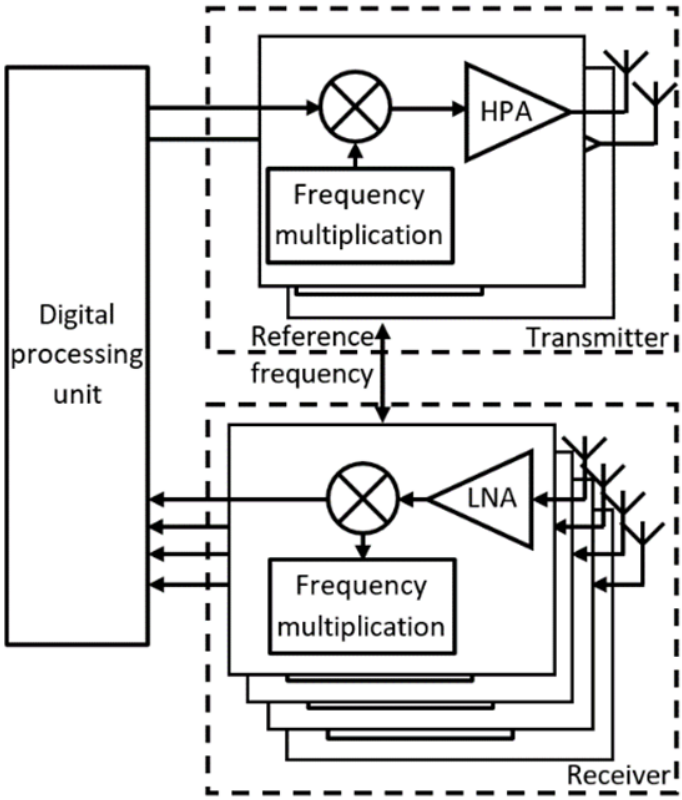

Fig. 1.18: Typical 2TX × 4RX MIMO radar architecture [29].

In addition to the angle estimation, MIMO radars exhibit improved SNR compared to SISO systems due to the higher number of transmission and receiving sections. The theoretical description of the MIMO radar implies that certain hypotheses are true [30]. In order to ensure constant propagation properties relative to the AOA of the received signal, the transmission medium must be isotropic and linear. This allows treating the received signals as a linear superposition of the signal wave fronts generated by the targets. If the target is in the far-field region, the received signals can be considered parallel to each other. It is usually a reasonable assumption if the distance between the targets and the radar is much larger than the dimension of the antenna array. A rule of thumb to check the subsistence of the far-field condition can be found in [31] and expressed in Eq. 1.36 hereafter.

$$R_{FF} > 2\frac{D^2}{\lambda} \tag{1.36}$$

where:

- R_{FF} is the minimum range to ensure the far-field condition.
- D is the maximum antenna dimension.

Moreover, the assumption of an additive white Gaussian noise (AWGN) channel ensures that the noise is uncorrelated, and the narrowband assumption guarantees that the characteristics of the received signals do not vary with the frequency, i.e., received signals are grouped around the carrier frequency.

The simplest architecture for detecting the angle of arrival consists of a single transmitting antenna and multiple receiving antennas. This is known as a single-input-multiple-output (SIMO) radar system. A signal, in the form of Eq. 1.22 if a sawtooth modulation has been chosen, is radiated by a transmitting antenna and, if a target is present in the scenario, the signal is captured by each antenna present in the receiving section as illustrated in Fig. 1.19.

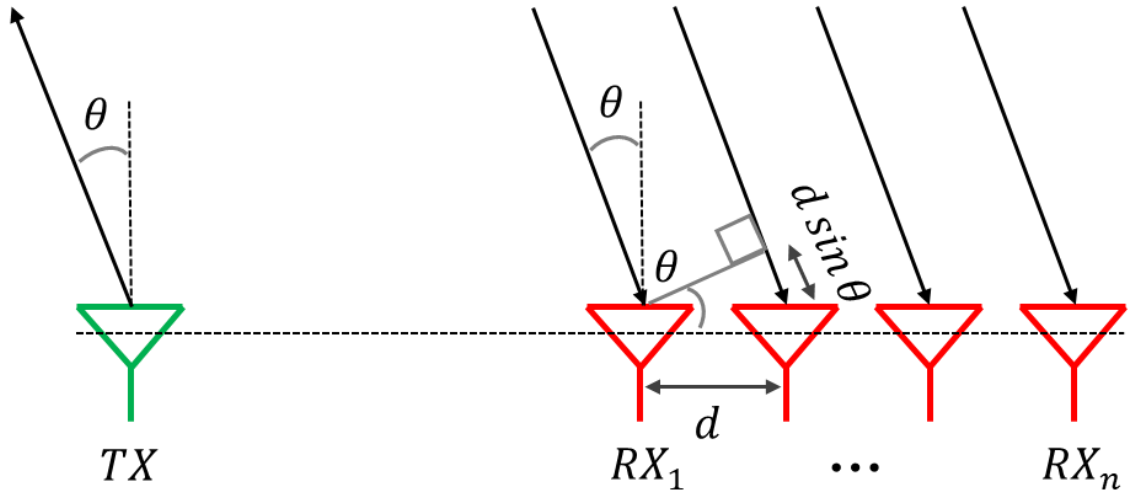

Fig. 1.19: Angle estimation with a simple SIMO radar.

The target is positioned at an angle θ to the radar and the antenna array is composed by N_{array} receiving antennas, each separated to each other by a distance d. In other words, the presence of TX and RX antennas at a defined distance is the main requirement to evaluate the spatial position of the target across the room around the radar itself. Assuming θ as the angle that must be estimated, at least one transmitting antenna and two receiving antennas are necessary. Indeed, the task is to calculate the extra distance $d \sin\theta$ that the received echo related to a subsequent antenna travels compared to the received echo of the previous one. Thus, the AOA can be calculated as in Eq. 1.37:

$$\theta = \sin^{-1}\left(\frac{\varphi \cdot \lambda}{2\pi \cdot d}\right) \tag{1.37}$$

where φ is the phase shift, i.e., the phase difference as seen in the previous paragraphs, between two received echoes of consecutive received antennas due to the extra distance. Thus, estimating the angle of arrival of an object requires at least two RX antennas. As for the case of Doppler and FMCW radars, an FFT can be applied to the different receiving elements to isolate the target angular position. Indeed, after range and Doppler processing, the remaining phase of the received signal is directly related to the angular location of the target with respect to the radar position, assuming zero phase noise.

Two important merit criteria in the MIMO field are the field-of-view and the angular resolution. It is worth noticing that the unambiguous FOV is defined as the angular volume in which the radar is able to detect a target, and the angular resolution is the minimum detectable angular difference between two different targets at the same range and speed. The π-limit, to warrant an unambiguous measurement, affects the FOV of MIMO radar system and it can be expressed as in Eq. 1.38 by, thus, replacing φ with π.

$$FOV = \pm \sin^{-1}\left(\frac{\lambda}{2 \cdot d}\right) \tag{1.38}$$

Normally, the inter-antennas distance is restricted to $\lambda/2$ to limit the presence of grating lobes in the spectrum. It follows, generally, that the FOV is the maximum and equal to value range from $-90°$ to $+90°$. Whereas the angular resolution can be defined in degrees as in Eq. 1.39.

$$\theta_{res} = \frac{180°}{\pi} \frac{\lambda}{N_{array} \cdot d \cdot \cos\theta} \tag{1.39}$$

where N_{array} is the number of elements in the array; this expression can be made easier by means of two assumptions: the inter-antennas distance equal to $\lambda/2$ and $\cos\theta = 1$ in case of a boresight view, i.e., $\theta = 0$. In this way, the angular resolution is dependent on the number of elements exclusively and a good resolution is necessary to discriminate more targets within the scenario. These equations are valid in the case of uniform array; otherwise, different considerations should be drawn. To deeply understand how to improve these performance parameters, the concept of virtual array must be introduced. In summary, each transmitted signal will be captured by every antenna in the receiving section. As can be trivially noticed in Eq. 1.39, the higher the number of receiving elements the better the resolution. At first glance, increasing the number of antennas in the receive section could be a good choice as highlighted in Fig. 1.20.

In this case, physical and virtual arrays coincide, and this aspect will become clearer shortly. Thus, each subsequent RX antenna experiences an additional phase shift relative to the preceding one.

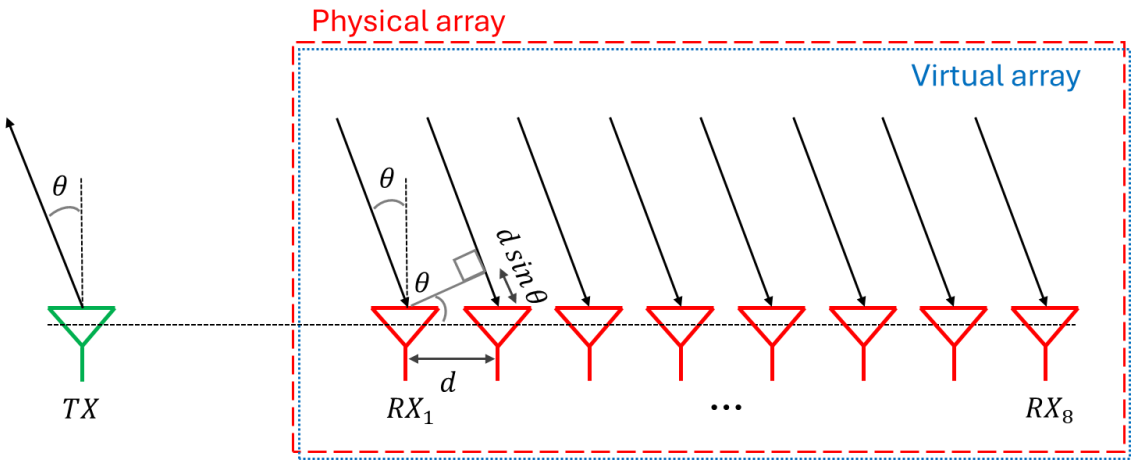

Fig. 1.20: Example of physical array.

Consequently, a linear progression of phase occurs with reference to the first receiving antenna and across the entire array. The corresponding phase differences are $[0, \varphi, 2\varphi, 3\varphi, 4\varphi, 5\varphi, 6\varphi, 7\varphi]$, the so-called steering vector. The phase can be estimated by sampling every echo signal from each antenna and performing an FFT on this phase sequence, known as the angle-FFT, between the range-Doppler matrix of every transmitter/receiver pair that is across the channels. The elaboration steps create a 3D matrix in this way. Unfortunately, the increasing number of elements has a huge impact on size, cost and complexity of the receiver due to the increasing number of low-noise-amplifiers (LNAs), mixers, filters and analog-digital-converters (ADCs) for each receiving channel. In fact, for each RX antenna the entire receive channel must be replicated. Until this point, the radar system is still SIMO-type. Consequently, the best solution is to increase the number of transmitting antennas too by defining a real MIMO radar system as illustrated in Fig. 1.21.

In this manner, the physical array in Fig. 1.21(a) consists of two transmission antennas and four receiving antennas. The transmission from the first antenna results in four received signals, each φ out of phase from the previous one. The second transmission antenna is placed at $4d$ from the first one, thus any signal from TX_2 travels an additional path of length $4d \sin\theta$ respect

to the path due to TX_1. The signal phase of the first receiving antenna due to the second transmission is 4φ, but only φ more than the phase of the last echo generated from the first transmission because of the d distance between the last antenna of the first transmission and the first antenna of the second one. Concatenating the phase sequences from the first transmitter $[0, \varphi, 2\varphi, 3\varphi]$ and from the second one $[4\varphi, 5\varphi, 6\varphi, 7\varphi]$, the same sequence of the SIMO radar is produced $[0, \varphi, 2\varphi, 3\varphi, 4\varphi, 5\varphi, 6\varphi, 7\varphi]$. In fact, Fig. 1.21(b) shows the virtual array that has been created with the identical structure and characteristics of the physical array in Fig. 1.20.

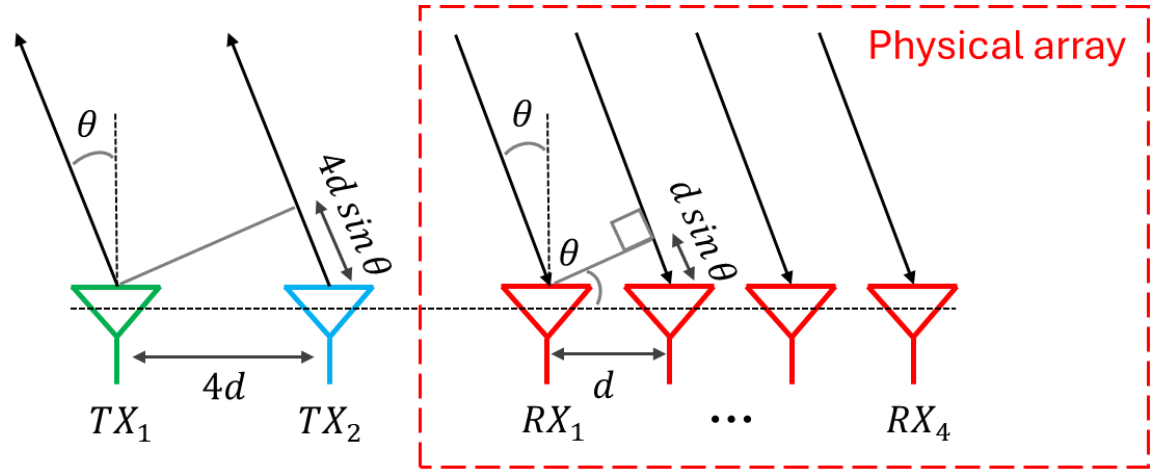

(a)

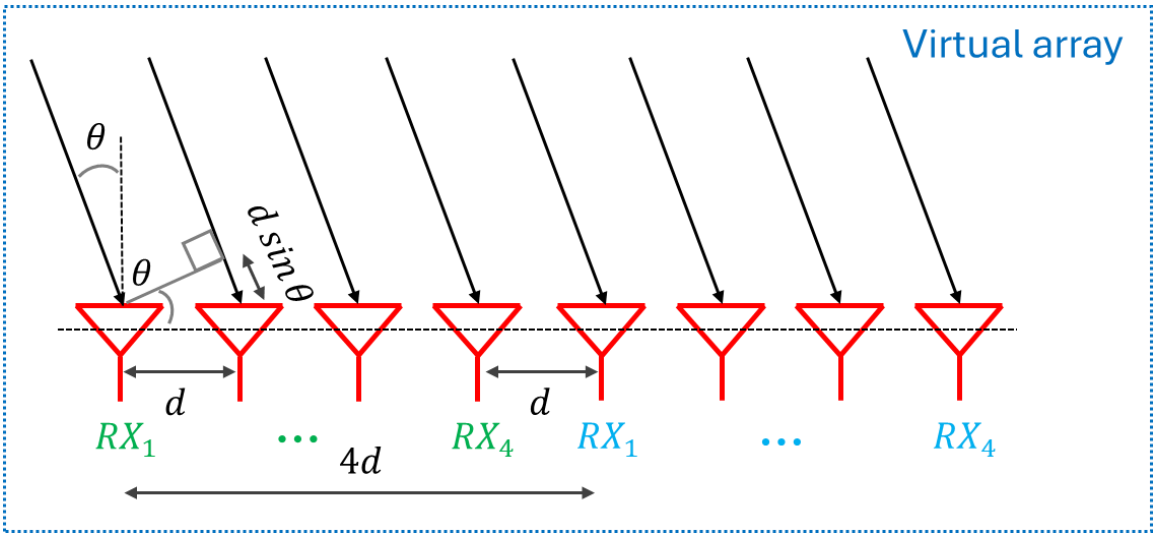

(b)

Fig. 1.21: Physical array (a) and corresponding virtual array (b).

Thus, the number of physical receiving antennas is four, but the addition of a second transmitting antenna permits to simulate the presence of four different receiving antennas if they are placed in the array properly. By this way, the angle resolution capability can be enhanced by adding virtual antennas and keeping relatively low the hardware complexity, in fact, the system in Fig. 1.20 presents nine path channels (one transmitting and eight receiving), three more than the other introduced by means of the addition of a second transmission antenna.

If the first array were composed of only four receiving antennas instead of eight, the angle resolution of the virtual array would have been better than the physical one. Trivially, the aperture of the virtual array would have been larger than the physical size of the real array.

This affirmation instills the idea that the angular resolution can be thought of as depending on the size of the array, instead of its number of elements. This finds confirmation considering that the increasing number of array elements leads to an extension of the array size.

Therefore, according to [32], [33], the Rayleigh criterion can be used to determine the virtual array length and, thus, the angular resolution as in Eq. 1.40.

$$\theta_{Rayleigh-res} \approx \frac{180°}{\pi} 1.22 \frac{\lambda}{d_{virtual}} \tag{1.40}$$

where $d_{virtual}$ is the array total aperture and it can be calculated by summing the distances among each element of the virtual array or the addition of the position of the last physical transmitter plus the last physical receiver's one minus the position of the first physical receiver. This expression is valid for both the uniform array and the non-uniform one. Generally, a larger antenna aperture must be designed to achieve a better angular resolution, and, for instance, this can be achieved using element spacings of λ instead of the conventional $\lambda/2$ at the cost of a reduced FOV. In summary, virtual antennas behave like additional physical antennas, keeping hardware complexity to a minimum, thus providing a cost-effective way to enhance the angle

resolution capabilities. The same virtual array can be realized by combining different distances between the TX and RX antennas. Therefore, the final choice may depend on how easily the array can be arranged on the radar board. Moreover, a multidimensional array can be realized by placing TX or RX antennas on different levels, enabling the detection of AOA in the elevation plane too and not only in the azimuthal one, as illustrated in Fig. 1.22.

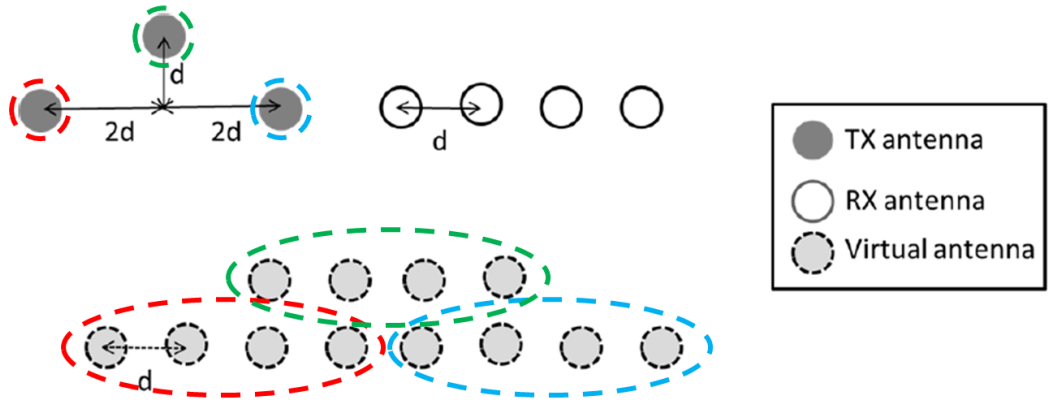

Fig. 1.22: Example of a two-dimensional MIMO array.

Thus, in the multidimensional array, the array elements are arranged both horizontally and vertically, creating a two-dimensional array to estimate azimuth and elevation angle at the price of a higher complexity in the AOA processing.

However, to properly estimate the AOAs, the received signals should be separated depending on the transmitter, thus involving orthogonality between the transmitting channels. The scientific literature has investigated several approaches, including those based on time division multiplexing (TDM), frequency division multiplexing (FDM), and binary phase modulation (BPM) [27], [34].

2 Radar board and data acquisition

This chapter lists the employed radar systems, highlighting their main features and differences. The increasing number of new applications in different fields demands radar sensors be adapted to each application. It has been considered valuable to have experience with radar produced by various companies such as Infineon, Texas Instruments and Indie Semiconductor, formerly Silicon Radar. After a brief description of each radar system, the final paragraph includes a comparison table.

2.1 Radar by Infineon

The BGT24MTR11 is a silicon germanium (SiGe) monolithic microwave integrated circuit (MMIC) used for signal generation and reception. It operates from 24 GHz to 26 GHz (K-Band). It is based on a 24 GHz fundamental voltage-controlled oscillator. It includes switchable frequency pre-scalers with output frequencies of 1.5 GHz and 23 kHz to monitor the frequency of oscillation. The main radio frequency (RF) output delivers a typical signal power of 11 dBm to feed an antenna according to the ISM regulations. An auxiliary local oscillator (LO) provides an LO signal to separate receiver components. An LNA provides a low noise figure (12 dB), and an RC polyphase filter (PPF) is used for LO quadrature phase generation of the homodyne quadrature down conversion mixer. The intermediate frequency (IF) frequency range is from 0 Hz to 10 MHz. Output power sensors, as well as a temperature sensor, are implemented for monitoring purposes. The device is controlled via SPI and the MMIC is packaged in a 32-pin leadless RoHS compliant VQFN package. The MMIC transceiver is depicted in Fig. 2.1 below.

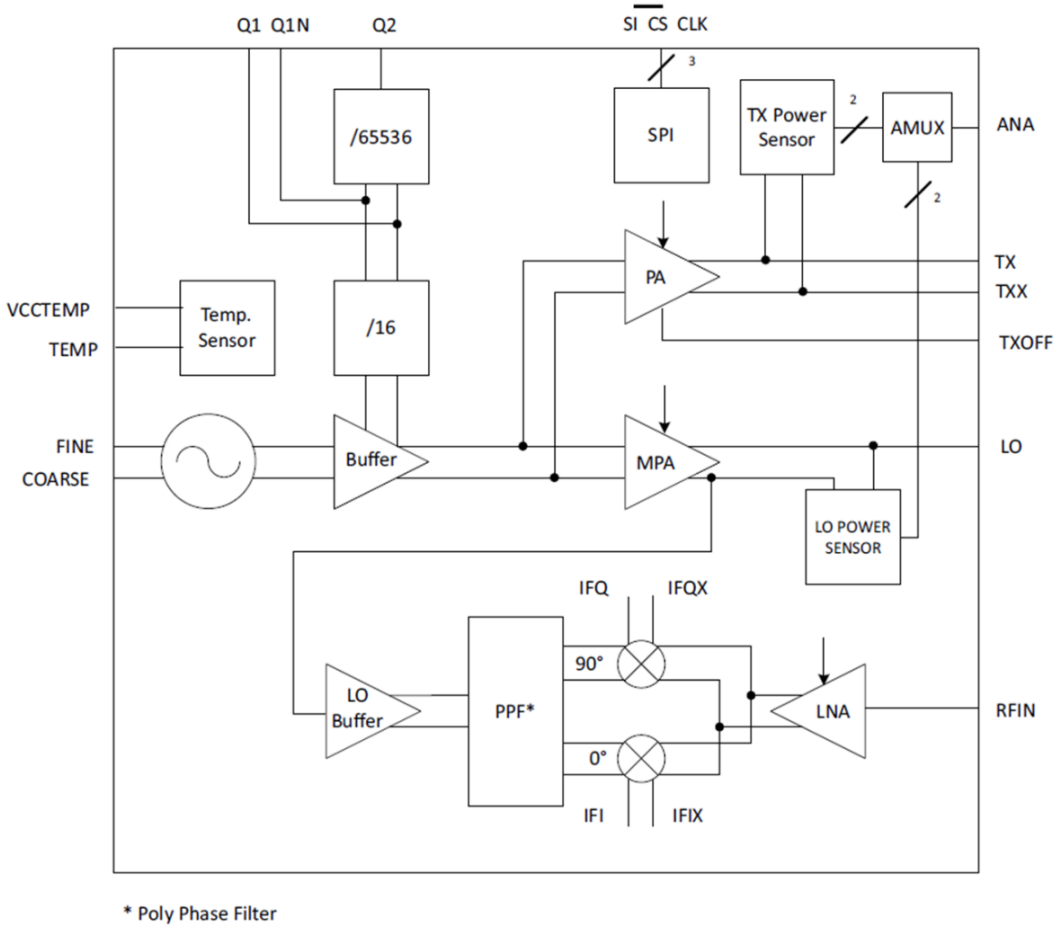

Fig. 2.1: The internal block diagram of BGT24MTR11 [35].

The operating temperature ranges from −40 °C to 105 °C and the supply current and voltage are 150 mA and 3.3 V, respectively. This transceiver has been designed to be used in monostatic radars. These radars are only capable of detecting a target's distance and speed, but not the angle of the target's position relative to the antenna because they are composed only of one transmitter and one receiver with I/Q outputs. Anyway, it is possible to detect the AOA using additional external RX antennas and receiver chains picking up the local signal from BGT24MTR11's LO output. This chipset is inserted into the Sense2GO2 board, which is one of the radar systems used during the doctorate course. Moreover, it is equipped with the 32-bit ARM® Cortex™-M4 based on XMC4200 microcontroller and microstrip patch antennas for the transmitter and receiver. The module is powered via micro-USB connector, when used with a

PC, through a low noise voltage regulator. The board is ideal for implementing radar applications such as motion detection and direction of movement analysis using Doppler radar, as well as distance measurement using the FMCW technique. Thus, the Sense2Go2 module is split into an RF part, an analog amplifier part and a digital part. The analog amplifiers provide the interface between RF and digital part of the board and their gains are configurable. The I/Q signals, i.e., the outputs of the BGT24MTR11 chipset, are differential and usually their amplitude is low, so it is necessary to amplify them. Besides, the IF amplification stage can be configured via setting resistor and capacitor values. The digital part consists of the mentioned microcontroller to sample and process the analog data from the RF frontend and to configure the BGT24MTR11 chip too. Its CPU frequency is 80 MHz, contains 256 kB flash and 40 kB RAM memories, two ADC and one DAC with 12-bit resolution are present. The block diagram of the entire system is in Fig. 2.2(a) and an overview of the components on the demo board is given in Fig. 2.2(b).

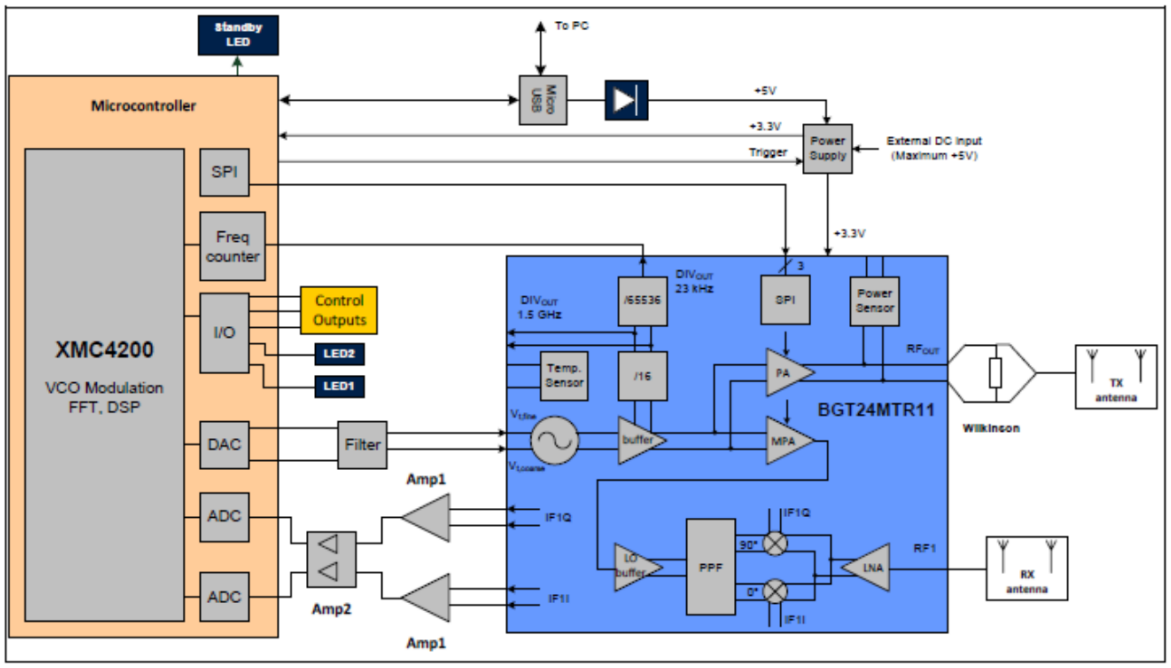

(a)

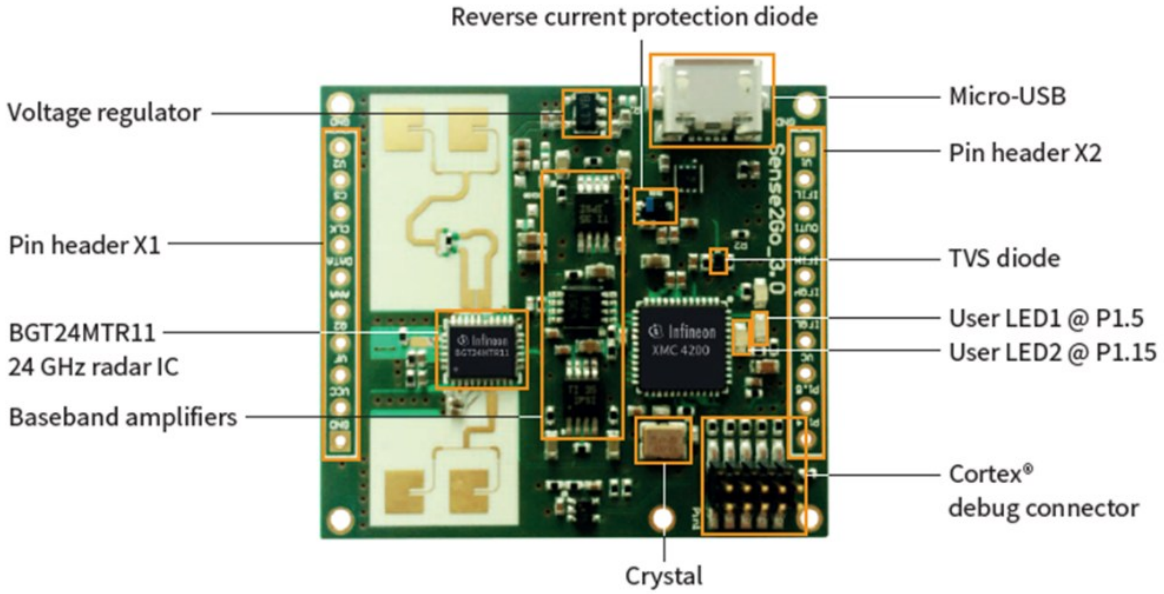

(b)

Fig. 2.2: Block diagram (a) and location of different building blocks on Sense2Go2 demo board (b) [36].

As previously mentioned, the board has integrated microstrip patch antennas as illustrated in Fig. 2.2(b), and a Wilkinson combiner is used to combine the differential transmitter output power from the radar IC before feeding it to the antenna. Instead, the receiver channel is connected to a dual analog amplifier stage located in the middle of the board. In the default setting, the demo is configured for a continuous wave operation and filters with low cut-off frequency are recommended for this mode. In any case, the value of the low-pass filters can be changed according to other modulation requirements.

The BGT24MTR11 chipset has not only been used in the form just shown. Another configuration is presented in Fig. 2.3. The transceiver is characterized by different transmitting and receiving antennas consisting of four patch elements each one to increase the gain, which are realized on the Rogers RO4350B substrate.

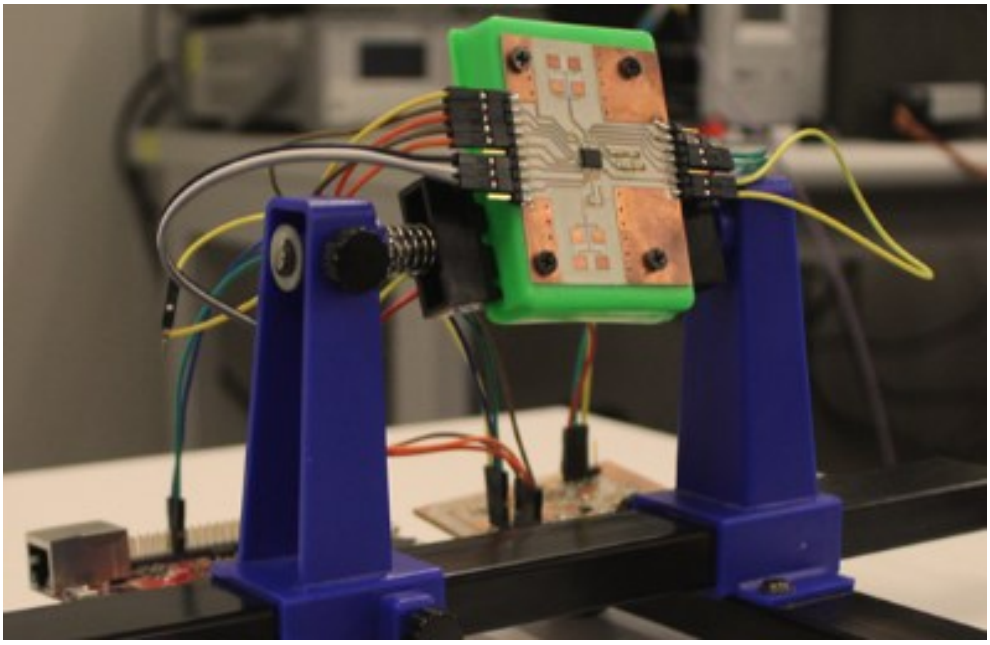

Fig. 2.3: Picture of the in-house realized radar system.

This system has a higher total gain than the previous one, thanks also to the ad-hoc two-stage differential alternating current (AC)-coupled baseband amplifier that was developed using internal laboratory facilities, i.e., an S103 Protomat high-precision milling machine by LPKF Laser & Electronics SE. The baseband board mount INA827AIDGKR instrumentation amplifier [37]. In addition, a custom ADC interface has been developed by exploiting a microcontroller unit (MCU) board based on the Infineon XMC4500 ARM® Cortex™-M4F microcontroller [38] to drive the front-end board, acquire signals and send the raw data to a personal computer. With the current system setup, it is possible to measure target maximum speeds up to 31 m/s which is higher than the previous system setup.

Custom MATLAB scripts were developed and used to properly process the raw data from the ADC. The work performed using this radar system will be presented in the next chapter.

2.2 Radar by Texas Instruments

The IWR6843 is a highly integrated single-chip mm-wave sensor based on FMCW radar technology and with the possibility to sense the AOA too. Its frequency coverage ranges from 60 GHz to 64 GHz (V-Band) generated from a 40 MHz input reference crystal oscillator. The IWR6843 includes the entire mm-wave blocks and an analog baseband signal chain for three transmitters and four receivers, as well as a customer-programmable MCU and a digital signal processor (DSP). This device is applicable as a radar-on-a-chip in use-cases with modest requirements for memory, processing capacity and application code size. At the same time, the IWR6843 device could be paired with a low-end external MCU to address more complex applications that might require additional memory for faster interfaces.

The RF section contains four parallel receive channels and three parallel transmit chains as sketched in Fig. 2.4.

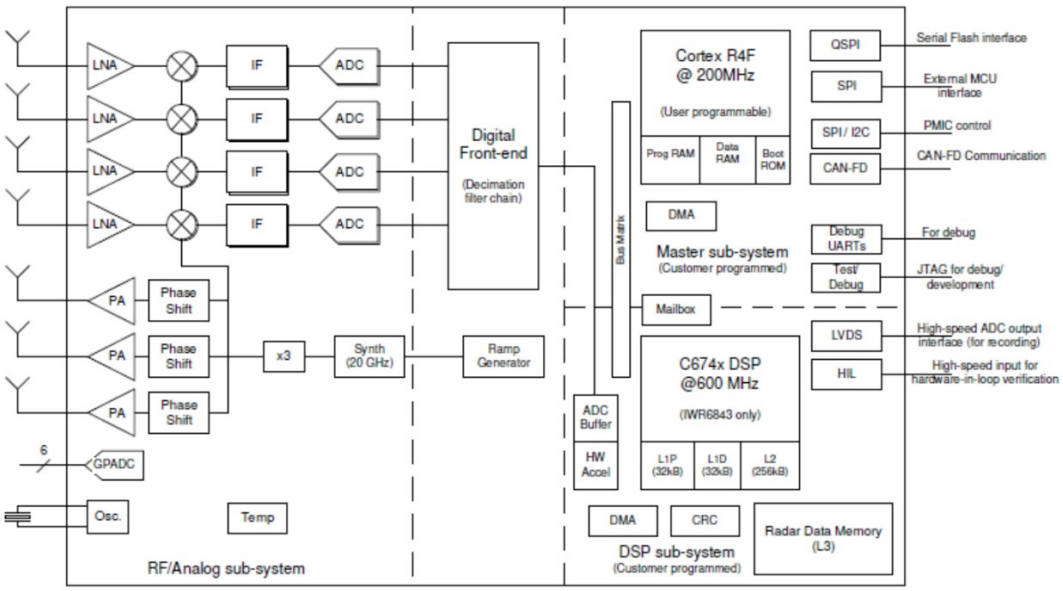

Fig. 2.4: Functional block diagram [39].

Each transmitter has an independent phase and amplitude control, and the device supports 6-bit linear phase modulation for MIMO radar. The transmitters can be simultaneously used,

and the ramp rate is equal to 250 MHz/µs. The transmission power is equal to 12 dBm, and the noise figure is 12 dB. The maximum intermediate frequency is 10 MHz. The device contains six ADCs with a maximum sampling rate for complex signals equal to 12.5 Msps and a resolution of 12 bits. The maximum current consumption and supply voltage are 2000 mA and 3.3 V respectively, and the average power consumption depends on the numbers of enabled transmitters and receivers and can reach the value of 2 W. The digital part has more CPUs, flash memories and RAMs to manage a complex system. The operating temperature is from −40 °C to 105 °C and the entire transceiver is encapsulated in a flip-chip ball grid array (FCBGA) package.

In any case, during the Ph.D. program, the IWR6843 was paired with the mmWaveICBoost, which is an add-on board used with the millimeter wave sensor. The mmWaveICBoost provides additional interfaces that enable configuration of the radar device and PC connectivity to the sensor. Thus, the entire system, used in the research activity, takes the name of IWR6843ISK-ODS. This radar system is characterized by an azimuth and elevation FOV of ±60° and an angular resolution of 29° in both directions. The system is furnished with onboard-etched short range wide field of view antennas, and the virtual array is shown in Fig. 2.5.

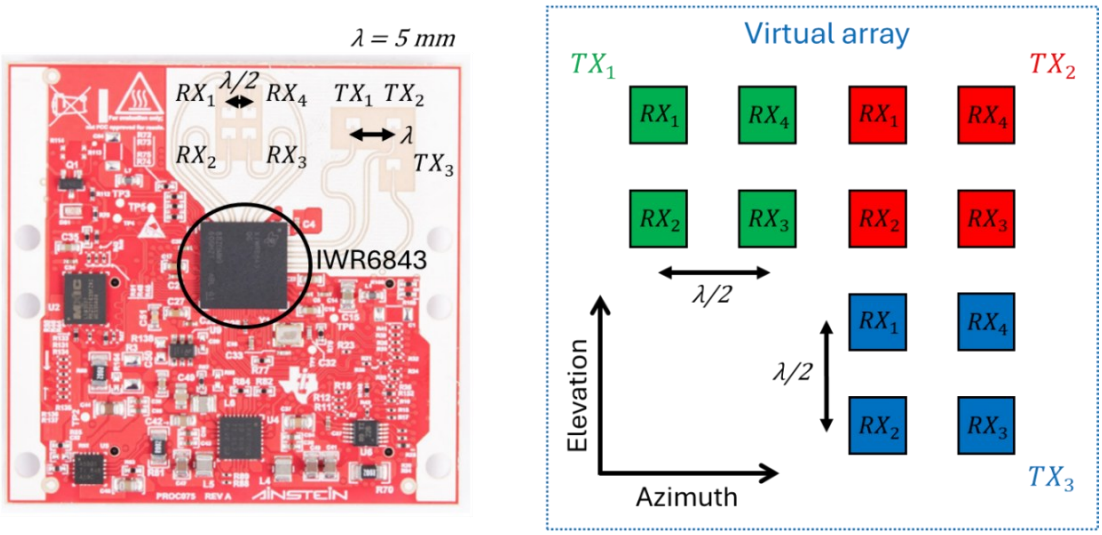

Fig. 2.5: PCB antennas and virtual array.

The IWR6843ISK-ODS has a printed circuit board (PCB) antenna gain of about 5 dBi. The disposition of the antennas in the virtual array confirms what was stated before, i.e., the system is characterized by equal angular resolution both in azimuth and elevation directions. The radar system was used during the research activity to gain initial experience with MIMO radar. It was used in modular mode to monitor the environment with the demo visualizer. The antenna module, visualized in Fig. 2.5, has been stacked on top of the mmWaveICBoost board as illustrated in Fig. 2.6 hereafter.

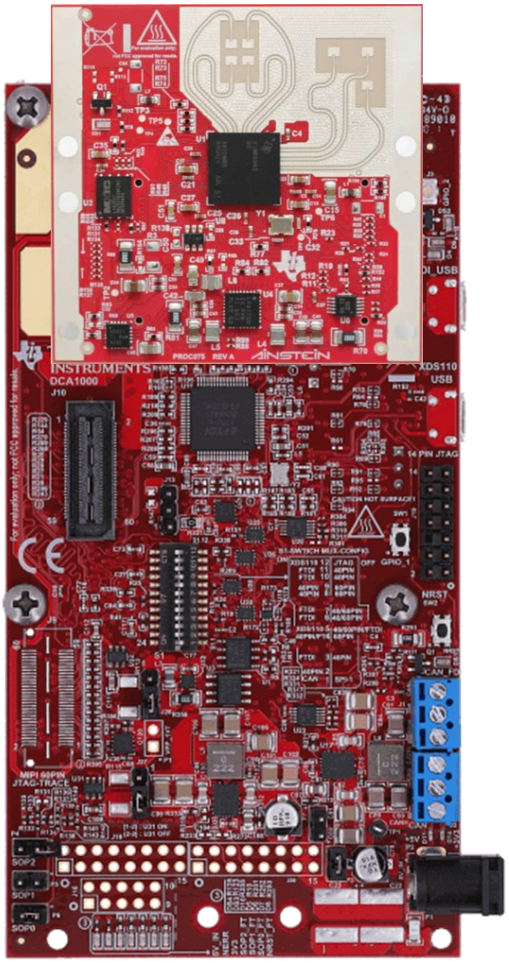

Fig. 2.6: Integration of the mmWaveICBoost and the antenna module with IWR6843 chip [40].

The Texas Instruments (TI) app [41], i.e., the demo visualizer browser-based app, was used for configuring the mm-wave sensor and visualizing the information obtained by elaborating the raw data. The sensor configuration permits, for instance, to set range and radial velocity

resolution, maximum unambiguous range and radial velocity and so on. Moreover, the demo permits to select the desired plots to be seen, such as range profile, range-Doppler map, scatter plot or range azimuth heat map. The work performed using this radar system will be presented in the third chapter.

2.3 Radar by Indie Semiconductor

The last sensor employed during the PhD program is the TRA_120_002 [42] by Indie Semiconductor, formerly Silicon Radar GmbH. Its frequency coverage ranges from 117.8 GHz to 127.3 GHz (D-Band). In detail, the TRA_120_002 is a highly integrated I/Q transceiver with antennas on-chip in SiGe technology. The radar front end (RFE), sketched in Fig. 2.7(a), includes an LNA, quadrature mixers, a poly-phase filter, a voltage-controlled oscillator (VCO) and transmit and receive dipole antennas. All these components are encapsulated in a 5 × 5 mm² QFN32 leadless plastic package. The dipole arrangement is visualized in Fig. 2.7(b).

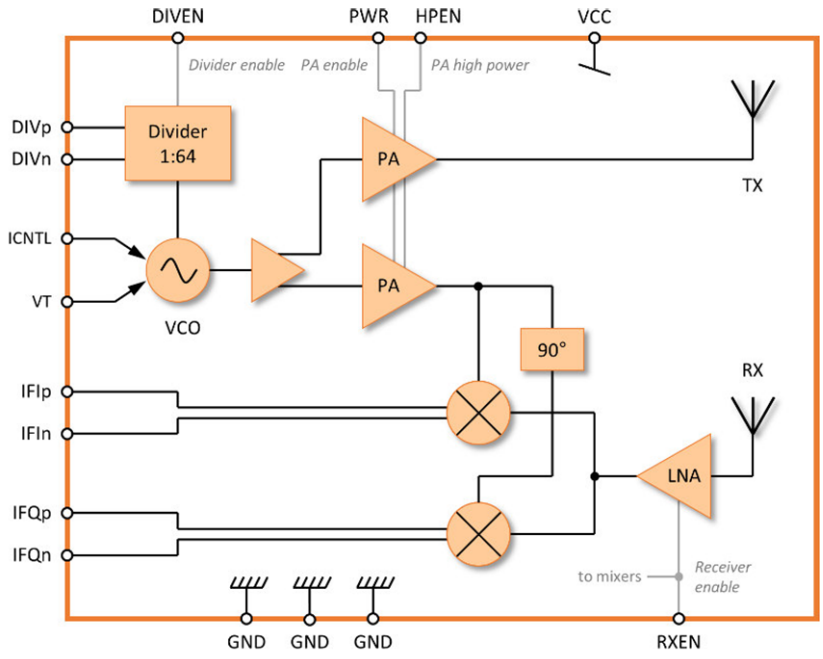

(a)

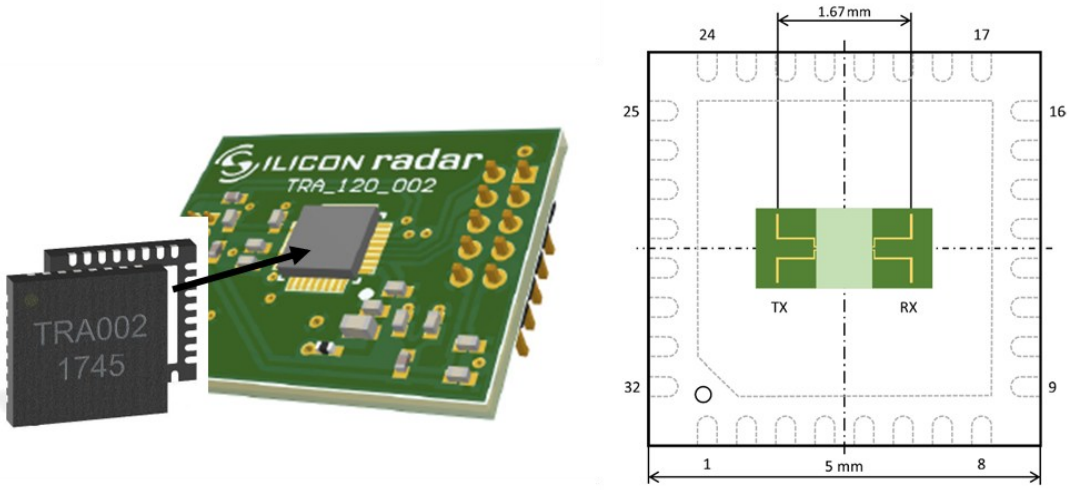

(b)

Fig. 2.7: Block diagram (a) and location of the on-chip dipole antennas (b) [43].

The 120-GHz LO has four analog tuning inputs with different tuning ranges and tuning slopes. These inputs can be combined to achieve a broad tuning frequency range. Together with the integrated frequency divider and external fractional-N phase-locked loop (PLL), the analog tuning inputs can be used for FMCW radar operation. Alternatively, with a fixed oscillator frequency, it can be used in CW mode. Other modulation schemes are also possible by utilizing the analog tuning inputs. The main field of application for this RFE is in super-short range radar systems. By using dielectric lenses, the range can be increased considerably.

The operating ambient temperature is from −40 °C to 85 °C, the supply voltage is 3.3 V and the supply current consumption is about 130 mA. The measured transmitter output power without antennas can reach the value of 1 dBm, and the receiver gain and the noise figure are 10 dB and 8.7 dB, respectively. The IF frequency ranges from 0 Hz to 200 MHz and the simulated gain of the dipole antennas can reach 10 dBi at an angle of 30°.

For a quick and easy start into the use of this radar system the SiRad Easy® evaluation kit [44], developed by Indie Semiconductor, can be used. It is an evaluation board system that provides a complete design environment which can be configured via a browser-based graphical

user interface and a communication protocol turned into enhanced development projects. The kit consists of an evaluation baseband board and an ST Microelectronics Nucleo-64 microcontroller board [45], and the entire system can be powered by a standard 5 V supply. All the stacked boards with lens assembled for a more directional beam are visualized in Fig. 2.8.

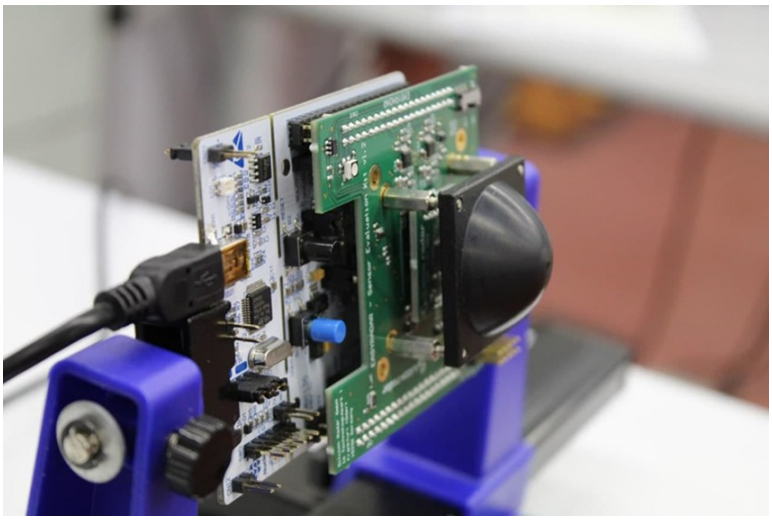

Fig. 2.8: Modular evaluation kit.

The whole system can be operated via an optimized graphical user interface on the web or through a terminal program, such as RealTerm, to configure the radar sensor and acquire the ADC raw data frame in the form of tab-separated values (TSV) to import them into third party software, for instance MATLAB.

In any case, to achieve a higher total gain, the ad-hoc two-stage baseband amplifier introduced in the first paragraph of this chapter was used. In addition, a custom analog-to-digital converter (ADC) interface has been developed using the DE10-Lite hardware design platform, which is built around the Altera MAX 10 field-programmable gate array (FPGA) [46]. This interface drives the front-end board, acquires signals, and sends data to a PC ensuring superior maximum detectable speeds for CW mode applications with respect to the system of Fig. 2.8. Thus, the TRA_120_002 has been employed as represented in the configuration shown in Fig. 2.9.

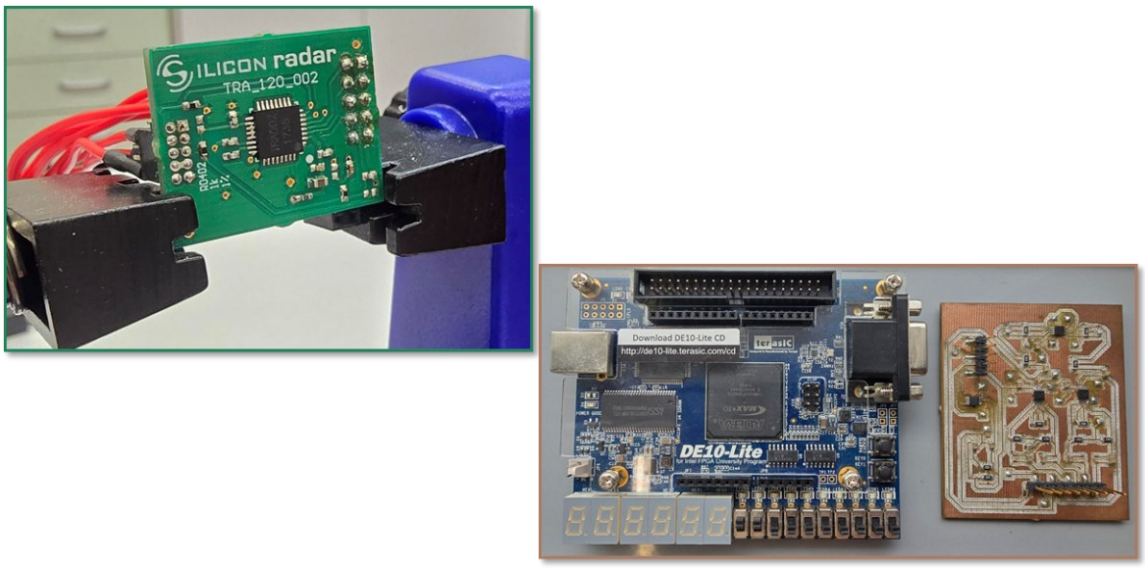

Fig. 2.9: A different radar system: the RFE board on the left, the FPGA and baseband amplifier on the right.

Of course, custom MATLAB scripts were developed to acquire data and optimize the elaboration steps also for real-time measurements. As will be shown in several paragraphs of the subsequent chapter, this new system has been used for different purposes. Finally, new TRA_120_002 chips were needed for a specific research activity which will be discussed in the second paragraph of the Chapter 3 detailly. Consequently, the updated version, TRA_120_045 [47], was purchased. This up-to-date transceiver version is characterized by a very large frequency bandwidth, from 111.5 GHz up to 137.2 GHz (D-band). Two tuning inputs with different tuning ranges and slopes allow the bandwidth to be extended to the full tuning range. The supply voltage is 3.3 V, and the current consumption is approximately 170 mA. Without antennas, the measured transmitter output power can reach a maximum value of 3.5 dBm. The receiver gain and noise figure are 11.5 dB and 9 dB, respectively. The IF frequency ranges from 0 Hz to 200 MHz just like the previous version. All these new characteristics have increased power consumption up to 560 mW with respect to 380 mW of the other transceiver, albeit manageable via controlling the duty cycle.

2.4 Comparison of listed radars

In the previous paragraphs of the current chapter, a variety of radar sensor systems have been introduced. For the sake of clarity, the main characteristics of each radar system are listed hereafter, Tab. 2.1, to highlight the necessary information for leading to a choice regarding the appropriate radar for every application of interest.

Tab. 2.1: Main features of the radar sensor systems used during the PhD activity.

	Radar by Infineon	Radar by TI	Radar by Indie
Operative frequency	24 GHz – 26 GHz	60 GHz – 64 GHz	111 GHz – 137 GHz
Bandwidth	K-band	V-band	D-band
Intermediate frequency	0 Hz – 10 MHz	0 Hz – 10 MHz	0 Hz – 200 MHz
Number of transmitters	1	3	1
Number of receivers	1	4	1
Type of antennas	Patch	Patch	Dipole on-chip
CW mode	✓	✗	✓
FMCW mode	✓	✓	✓
MIMO	✗	✓	✗

In short, radar with higher operating frequencies has been favored for micro-motion detection because it is more sensitive to phase variations, which are, in turn, caused by micro-displacements of the target. Instead, bandwidth is important if range accuracy and resolution should be enhanced. A higher IF frequency is crucial to extend the maximum detectable range. The number of antennas in the transmitting and receiving sections is fundamental to estimate the AOA and improve the angular resolution. The type of antenna is not a discriminating factor because all of the radars used have antennas with a relatively low gain. Finally, the CW mode

is crucial if elevated speed must be estimated because the FMCW mode limits the maximum speed due to the higher time measurements.

All these aspects have been considered in order to make an informed decision about which radar is appropriate for each application as will be discussed in the final chapter.

3 Case studies

Following the discussion of radar theory and the radar systems used during the research activity, this chapter will present all case studies for short-range applications. A variety of topics will be addressed, ranging from CW to frequency-modulated radar and the initial design steps for a MIMO radar with single radar front ends. Transitioning from space and navigation to safety car interiors, all the way to the detection of vital signs and eyelid movement to help the communication of patients with neurodegenerative disorders.

In Chapter 3.1, the need to detect and track the position of small boats and space debris is discussed, suggesting the use of FMCW radars. On the other hand, Chapter 3.2 explores cutting-edge solutions in the D-band spectrum, offering an innovative approach to MIMO radar designing. During Chapter 3.3, there will be some key moments to delve into the details of how to improve I/Q data elaboration and exploit it to give prominence to particular features. All improvements to signal processing will be used in Chapter 3.4 to estimate rapid speed variations for gesture recognition and, in Chapter 3.5, enable meticulous real-time reconstruction of chest displacement during normal respiratory activity by means of different CW radars. Finally, Chapter 3.6 avails of every progress presented in previous chapters to recognize eye blinking and discern eye closing and opening, aimed at permitting people with paralyzed body parts to communicate comfortably and with privacy-preserving by means of radar. Furthermore, the eyelid movements will be calculated by taking advantage of the superior displacement detection sensitivity in case of radar operating at very high frequencies.

Therefore, the remainder of this dissertation wants also to underscore that radar is becoming a ubiquitous tool for advanced, reliable and comfortable motion detection, as demonstrated by practical and tangible case studies.

3.1 Space and navigation

This paragraph focuses on research activities involving FMCW radar systems. In detail, two main applications will be discussed: maritime in-harbor navigation [15] and debris detection in the spatial environment [16].

The former investigated the feasibility of a short-range ship collision avoidance system. This system, which uses microwave and mm-wave radars, aims to accurately detect possible obstacles and their distances inside the harbor. While ships are usually equipped with long-range radars for open-sea navigation, in-harbor navigation relies solely on the captain's manual ability. An accurate model of the real scenario was proposed by considering obstacles of interest, such as small ships and shore structures. Different operating frequencies were considered and evaluated to develop a reliable system that can effectively assist with navigation. This work paves the way for autonomous ship navigation by exploiting advanced sensing technologies.

The latter describes a preliminary project for a radar system designed to detect space debris. Unlike conventional debris detection systems, which rely on ground-based radar or optical instruments, the proposed radar would be mounted on a satellite. Due to the peculiarities of the space environment, several technical constraints arise in addition to the classic target detection requirements. The technical characteristics of the radar payload together with the expected performance will be discussed later.

The interest of commercial and military ship owners, nowadays, is directed towards increasing the security of in-harbor navigation [48], [49]. Due to globalization, the number and size of shipping vessels, as well as the density of navigation within ports, are dramatically increasing [50]. Higher traffic volumes increase the risk of collisions, which are mainly due to human error or the absence of assistance systems [51]. A great effort was devoted by the

scientific community to address this concern, trying to increase the automation level during ship handling [52], [53], [54]. One of the main issues is represented by the collisions with other objects including shore structures [55]. This situation is particularly delicate in near-coastal areas, e.g., during berthing operations. The presence of vessels moored in the harbor and other small boats such as pencil-ducks and ski-boats is a frequent cause of collision and all the related dynamics deserve to be investigated.

One possible approach is to calculate the safest and best trajectories for the ship before it enters the port. In [56], a two-step optimization-based motion planner for the autonomous maneuvering of ships in the harbor was proposed and validated in a simulated model of the Cape Town harbor. However, this method has the great limitation of being static, since it does not take into account the unexpected presence of small ships. In [57], a collision avoidance dynamic critical area (CADCA) was introduced for the case of ship allision. The CADCA geometrically delimits the required maneuvering space of a ship. It is dynamic in the sense that the shape of the maneuvering space depends on the main characteristics of the ship, i.e., rudder angle, and initial forward speed.

Another approach is to equip the ship with sensors aimed at assisting the navigation. This concept is not novel, indeed radars, for example, represent the standard sensor used in marine navigation environments. However, they are employed for long-range detection and regulations dictate that radar systems must be turned off in the harbor [58].

In [59], a navigation system based on laser technology was described and tested in inland navigation scenarios. Different targets of interest were detected and tracked, thus showing promising results. However, laser technology has a limited minimum detectable distance and requires good light conditions. In addition, performance falls down in snow, fog, rain, and dusty weather conditions [60].

In this scenario, although the beneficial features of radar technology were demonstrated in different areas of interest, they were not adequately investigated for short-range ship navigation systems [61], [62], [63], [64]. Radars ensure excellent performance in terms of spatial resolution and immunity to different lighting and temperature conditions. Due the low required computational resources and the absence of privacy concerns they can be exploited as monitoring systems in a wide range of scenarios [65], [66].

In [67], a preliminary study on radar-based navigation systems was reported. It is based on a 24 GHz commercial radar and shows encouraging results concerning the radar capability to detect targets in such a kind of scenario. Therefore, the intention was to demonstrate the beneficial features of radar technology for navigation assistance. The FMCW operating mode has been selected for the premium spatial resolution with limited operating bandwidth. The cost-effectiveness of the system has been considered as a key element for designing a successful navigation aid. Therefore, the operating frequencies were selected based on commercially available radars, from the industrial to automotive sectors. Real operating scenarios were investigated to ensure reliable detection of small ships and shore structures. The entire radar system was modeled by reproducing the channel behavior, including both the targets and the sea clutter. As extensively discussed in Chapter 1.3, the output of the range processing step is typically displayed as a power spectrum graph extracted by applying the FFT. To demonstrate the feasibility of the system, a real scenario will be simulated using a computer-aided design platform, i.e., National Instruments AWR Design Environment®. Three radar operating frequencies were considered among commercially available devices, in detail:

- 24.00 GHz – 24.25 GHz;
- 60.00 GHz – 64.00 GHz;
- 77.00 GHz – 81.00 GHz.

Consequently, three different simulations, each with specific parameters depending on the hardware characteristic of commercial devices, have been set. The block diagram of the simulated scenario is reported in Fig. 3.1. It includes the transmitting and receiving sections of the radar, as well as the channel model.

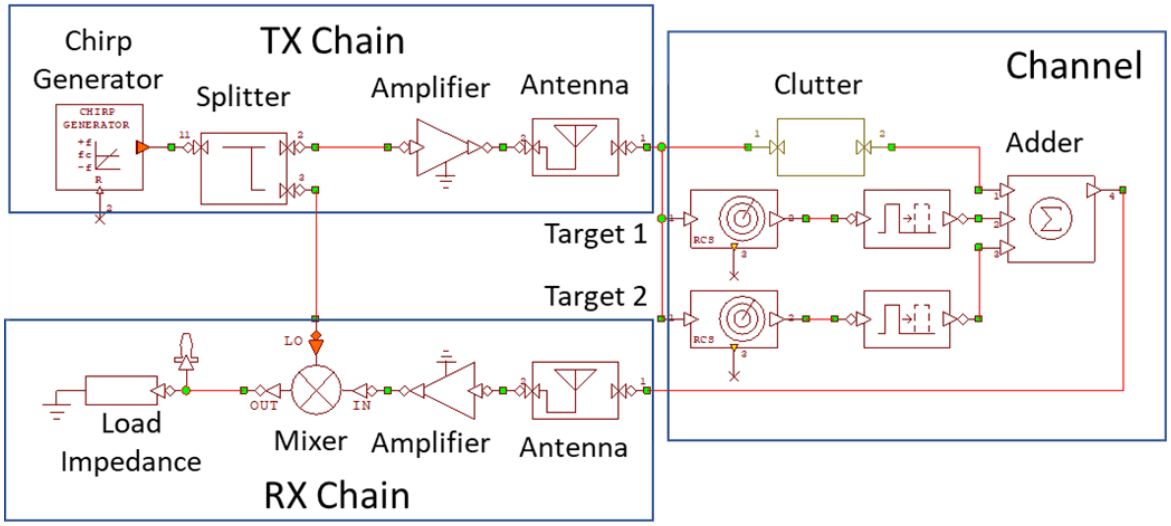

Fig. 3.1: Block diagram of the simulated scenario, including radar and channel models.

The entire transceiver section retraces the one sketched in Fig. 1.14. The same antenna parameters are used for both the TX and RX chains. The gains of both the power amplifier and the antenna have been set by fixing their values according to the effective isotropic radiated power (EIRP) defined by the ISM regulations. A low radar duty cycle was considered to save power by reducing the time when the transmitter sends a signal. Keeping the duty cycle low means the radar uses less power on average. The RRE, Eq. 1.4, was used to estimate the received signal power and compare it with the simulated results. The channel considers both the possible presence of targets and the clutter introduced by the sea. The target presence was modeled by using a delay block for reproducing the time-delay due to the round-trip signal. Moreover, a block that takes into account the target RCS has been used. Since the goal of this contribution is to detect small boats, such as pencil-ducks, and the dock distance, typical RCS

values have been considered. Specifically, RCS values of 1 m^2 and 316 m^2 were used for the pencil-ducks and docking structures, respectively [68], [69]. Finally, the presence of the sea has been simulated by considering an average RCS of 0.032 m^2 distributed throughout [68].

Considering the maximum range resulting from the maximum available EIRP for the different operating frequencies, the 24 GHz system has only been tested for very short ranges, i.e., a few tens of meters. The aim of this radar, operating in the microwave range, will be the detection of docking structures. On the other hand, radars operating in the mm-wave range have been tested for long-range scenarios within the harbor, up to 200 m. In this scenario, the targets of interest are small boats, like pencil-ducks or ski-boats. The design choice to use different radar frequencies for short and long-range detection is also due to the different location of the radars aboard the vessel. In detail, long-range radars will be mounted on top-edge of the ship, whereas short-range radars will be mounted a few meters above sea level on the hull. Their only task is to detect docks.

The first simulation involves the 24 GHz radar, whereby the presence of a concrete dock at 6 m has been considered. The spectrum of the beat signal is shown in Fig. 3.2.

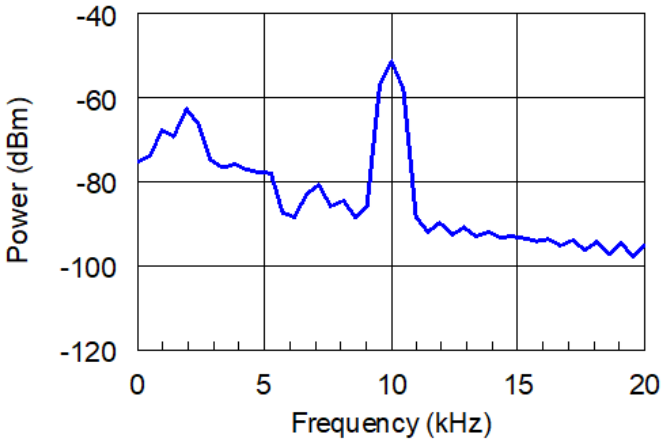

Fig. 3.2: Spectrum of the beat signal for the 24 GHz radar.

By observing Fig. 3.2 there is a peak at a frequency of 10 kHz, which is characterized by a power level of approximately -50 dBm. Despite the sea clutter, the dock has been properly

detected, and the peak frequency corresponds to the expected distance of 6 m according to Eq. 1.27. Long-range simulations were performed using mm-wave radars to detect small boats in the harbor. The result for the 60 GHz industrial radar is reported in Fig. 3.3.

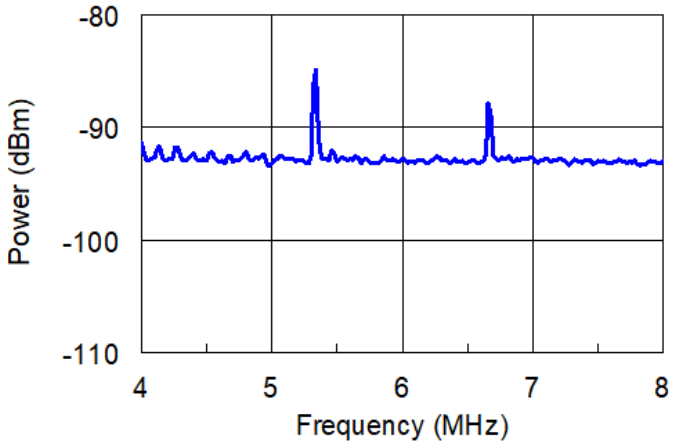

Fig. 3.3: Spectrum of the beat signal for the 60 GHz radar.

The presence of two pencil-ducks at different ranges has been simulated. In Fig. 3.3, there are two power peaks, centered at the frequencies of 5.33 MHz and 6.67 MHz. They correspond to the pencil-ducks at 200 m and 250 m, respectively. Of course, the power peak of the latter is lower due to the higher simulated attenuation. Despite the presence of sea clutter, which generates additional small power peaks, the two ships are successfully detected. Similar results can be obtained by investigating the case of the 77 GHz radar case, as highlighted in Fig. 3.4.

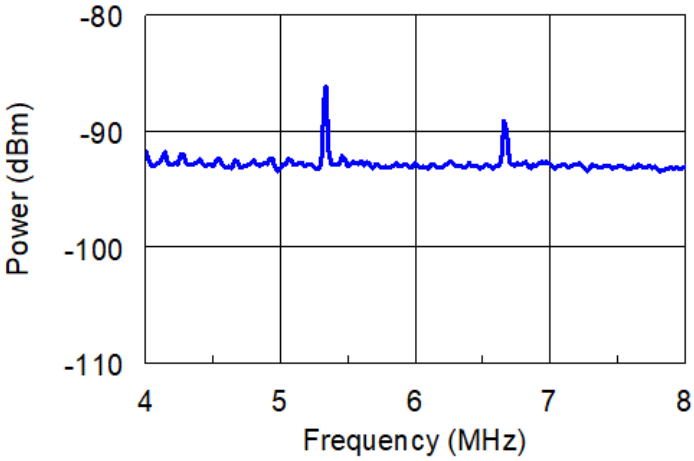

Fig. 3.4: Spectrum of the beat signal for the 77 GHz radar.

Also in this case, the detection of pencil-ducks is feasible. Only the operating wavelength was modified in the simulation, thus affecting both the free-space attenuation and target gain values. Thus, the use of an industrial radar or automotive radar is almost indifferent to successfully detecting objects of interest.

Therefore, a radar-based sensing system for ship collision avoidance has been tailored for in-harbor scenarios. Operating frequencies ranging from the microwave to the mm-wave have been investigated by analyzing the feasibility of the different solutions. A real scenario has been simulated by considering different boats and shore structures. The simulated results demonstrated the effectiveness of the proposed system.

As mentioned at the beginning of the first paragraph of the current chapter, another research activity involving FMCW radar systems and related to space applications is presented in this thesis.

The number of new space missions and satellite launches is continuously growing to address the very high demand for satellite-based services and applications, e.g., communication, deep space exploration and Earth observation. Concurrently, the amount of space debris is also increasing. Space debris refers to both natural meteoroids and artificial orbital debris. Artificial debris include abandoned launch vehicle stages, obsolete satellites, and fragmentation debris. Currently, more than 129 million objects with dimensions starting from a few millimeters are orbiting around the Earth. Despite their small size, anything traveling at speeds slightly lower than 60,000 km/h in an orbit around Earth is potentially dangerous. One of the most considered problems concerns the possibility of collision with operating satellites. Although some recent missions require de-orbiting procedures to prevent an increase of space debris, particular attention is now paid to remove existing debris, especially the larger ones [70].

The European Space Agency (ESA) is planning to launch the first mission in the world to remove space debris. ClearSpace-1, which is the name of the mission, is planned for launch in 2025 [71], but at this moment it has been postponed. The purpose of the mission is to rendezvous, capture and allow for the reentry of the upper part of the Vega secondary payload adapter (VESPA). It is a part of the rocket launched in 2013 that weighs more than 100 kg. ClearSpace-1 will capture the VESPA by exploiting a robotic arm and will finally carry out a controlled atmospheric reentry. Among the different involved aspects, the debris detection approach varies depending on the sensing system location, i.e., the novel on-satellite or classic ground-based systems. The trajectories of debris in low-Earth orbit (LEO) can be predicted to some extent, but they are not usually stable over long periods of time. Therefore, their precise positions require continuous updating. Ground-based radars and optical measurement systems are among the most used space debris detection technologies from the Earth [72], [73]. Of course, the a-priori debris trajectory information is exploited to point the main beam of the radar to a predetermined coarse position. Optical-based systems, such as telescopes, are mainly used for higher-altitude observations, e.g., targets in geostationary orbits (GEOs). On the other hand, on satellite systems are raising a continuously growing interest [74], [75], [76], [77]. In the scientific literature, the typical detection distance may be as low as 500 m because the radar has the task to detect the debris without enabling a satellite to rendezvous. In contrast, the radar presented in these pages should be able to effectively detect the VESPA target from a very short range of a few meters to one kilometer.

The goal of the project is to detect space debris such as the VESPA. Particular attention is paid to the constraints arising from the target of interest. Moreover, the system is designed for a specific type of miniaturized satellite: CubeSats. This is an important consideration because, although CubeSats are characterized by several advantages that have made them popular, they

have more demanding requirements, particularly with regard to size, weight, and power consumption [78], [79]. The schematic representation of the scenario, just described, is illustrated in Fig. 3.5.

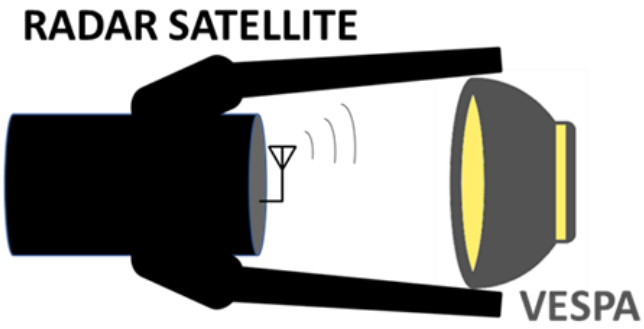

Fig. 3.5: Satellite approaching the VESPA with the help of the radar.

In detail, the radar is mounted aboard the satellite, pointing towards the VESPA target. A-priori information concerning the debris and the VESPA trajectory allows launching the radar satellite directly in the same orbit as the VESPA. This configuration reduces the issues related to the high speed of the target because, by rotating in the same orbit, the relative speed between target and radar will be near-zero. Consequently, the velocity requirements will only be related to the rendezvous speed. In Tab. 3.1, the system technical specifications are reported.

Tab. 3.1: Technical requirements.

Requirements	Numerical value
Central operating frequency	9.55 GHz
Minimum target range	5.00 m
Maximum target range	1.00 km
Maximum unambiguous speed	3.00 m/s
Minimum speed resolution	0.10 m/s
Measurement data rate	5 Hz

The minimum target range has been fixed to the minimum distance required to capture the target by exploiting the robotic arms. By exploiting the known VESPA trajectory information, it is possible to place the radar in the same orbit of the VESPA with a maximum distance less than 1.00 km. The maximum unambiguous speed is limited to the maximum rendezvous speed, whereas the measurement data rate of 5 Hz is required to allow comfortable satellite maneuvering. The block diagram of the proposed radar payload is reported in Fig. 3.6. The FMCW radar payload, employing sawtooth modulation, mainly embeds the following sections:

- A microwave receiver designed at 9.55 GHz including I/Q mixer, LNA, filtering sections and ADC.
- A microwave transmitter with MMIC waveform generator, the VCO in PLL configuration and the power amplification stage.
- FPGA and processor to extract target information.
- TX and RX antenna array.

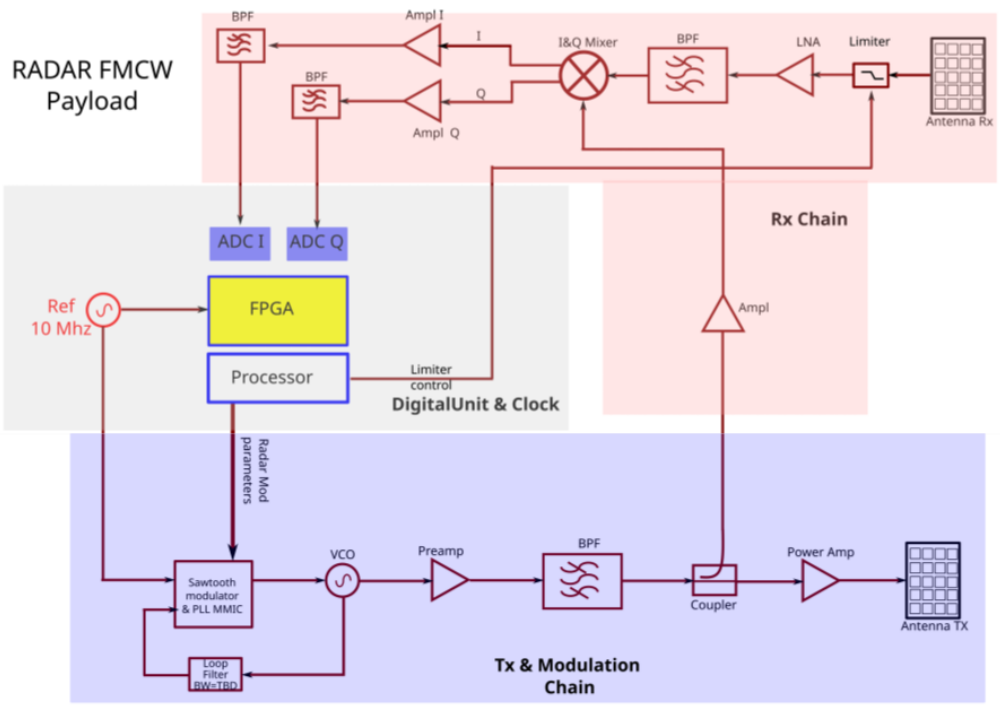

Fig. 3.6: Radar payload block diagram.

Commercial off-the-shelf (COTS) MMIC is exploited to reduce the unit dimension. This is a key requirement for every space system, even more for CubeSat payloads. The co-design of the mixed-signal transceiver with the FPGA-based digital signal processing represents a trade-off between the radar performance and its implementation complexity. The PLL is required to control the VCO frequency output with the task of achieving the accurate frequency modulation of the transmitted signal around 9.55 GHz. Therefore, the typical non-linearity of the free VCO might be reduced to a further extent. The presence of a preamplifier is beneficial to adjust the carrier level to obtain the desired output power level according to the link budget defined later on. The quadrature mixer allows to improve the received SNR and detect the target direction. The amplified down-converted signal is converted to digital domain and processed by the FPGA. The range and speed extractions require implementing a 2D FFT as already discussed in Chapter 1.3.

The first step to designing a radar system with such constraints consists of fixing the modulation bandwidth. This has a great impact on the range resolution, which however is not considered a key requirement due to the probable presence of only a single target. Anyway, according to Eq. 1.28, the bandwidth B is fixed to 500 MHz, thus resulting in a range resolution of 30 cm. The maximum unambiguous speed v_{max}, in turn, fixes the chirp duration τ_{chirp} assuming a null idle time. According to Eq. 1.33, the speed requirement of 3 m/s sets the maximum chirp duration to 2.62 ms. From Eq. 1.27, it is worth noting that increasing the chirp duration decreases also the maximum expected beat frequency with the target range remaining equal. This is of course beneficial because decreasing the beat frequency, in turn, lowers f_s relaxing the ADC requirements and improving the digital SNR. Indeed, the digital SNR is strictly related to the digital resolution that improves by decreasing the sampling frequency, for the same number of samples [80], [81], [82].

Moreover, the product $M \cdot \tau_{chirp}$ with M as chirp-per-frame must be constant and higher than 157 ms to provide the required speed resolution δ_v of 0.1 m/s according to Eq. 1.34. However, increasing this product is not beneficial, indeed, it is worth noting that for obtaining speed information, it is necessary to wait for the full frame time. Thus, the higher the frame time, the slower the measurement time. Due to the data rate requirement of 5 Hz, the maximum total processing time might be equal to 200 ms. Therefore, the τ_{chirp} and M have been set equal to 2.6 ms and 64, respectively, to achieve a suitable measurement time. If required by technological constraints, shorter time duration can be considered, e.g., a chirp duration of 1.3 ms with 128 chirps-per-frame or 0.65 ms with 256 chirps-per-frame. Of course, increasing the number of chirps-per-frame increases the number of data to elaborate for each frame, thus increasing the computational load. Since the total resulting transmission time is 166.4 ms, the maximum remaining time required to perform the signal processing is 33.6 ms.

Upon fixing the bandwidth and τ_{chirp}, the f_s has been set according to Eq. 1.30. To obtain an R_{MAX} of 1 km, a minimum f_s of 2.56 MHz is required. The number of samples-per-chirp is the result of the already set parameters and should be carefully chosen to preserve the theoretical range resolution of 30 cm. Indeed, the fast-time FFT should have a resolution at least corresponding to the minimum radar δ_R. Therefore, the number of samples-per-chirp, set equal to the number of fast-time FFT bins, has been fixed to the value of 4096. The calculated radar payload parameters are summarized in Tab. 3.2.

Tab. 3.2: Radar payload parameters.

Payload Parameters	Calculated values
Modulation type	Sawtooth
B	500 MHz

τ_{chirp}	2.6 ms
Samples-per-chirp	4096
M	64
Total transmission time	166.4 ms
f_s	2.56 MHz

The next step consists of estimating the link budget and the related dynamic range required to detect a target from 5 m to 1 km. The equivalent noise bandwidth of the receiving filter to compute the input noise floor and the minimum detectable signal (MDS) is, in first approximation, the noise enclosed in the single FFT bin [80], [81], [82].

Therefore, the equivalent noise bandwidth B_{eq} to compute the input noise floor is equal to half the f_s divided by the number of samples-per-chirp, i.e., 313 Hz or 25 dB. Considering the characteristics of up-to-date low noise components, the total receiver noise figure (NF) can be set to a reasonable value of 4 dB [19]. Because the antenna beam is oriented towards space, the antenna noise temperature T_A can be considered about 100 K. The same value can be used for the reference receiver temperature, T_{ref}. According to Eq. 3.1, the noise temperature of the receiver chain T_R is 151 K.

$$T_R = T_{ref}\left(10^{\frac{NF}{10}} - 1\right) \tag{3.1}$$

The total system temperature T_S can be, thus, computed from Eq. 3.2.

$$T_s = T_R + T_A = 251\ K \tag{3.2}$$

Finally, it is possible to calculate the input noise power, P_{Noise} as shown in Eq. 3.3 where k is the Boltzmann constant.

$$P_{Noise} = 10\log_{10} kT_S + 10\log_{10} B_{eq} = -149.7\ dBm \qquad (3.3)$$

Considering 6 dB of additional losses from misalignment between the antennas and targets, plus 2 dB from cables, mismatch, and connectors before the LNA, the total additional losses equal 8 dB. With a target at 1 km, TX and RX antenna gains of 20 dBi, and a TX power of 25 dBm, the received signal level will be -136 dBm, assuming a worst-case target RCS of 0.1 m². Consequently, the SNR will be 13.7 dB.

As Fig. 3.7 shows, the SNR value permits to obtain a probability of detection by to 90%, even in the worst-case scenario. It is worth noting that the relationship between the probability of detection and the signal-to-noise ratio is linear only in some parts of the reported graph, not at every point. Additionally, in terms of power consumption a low duty cycle was considered to save power since the transmitter is only active for a very short period of time.

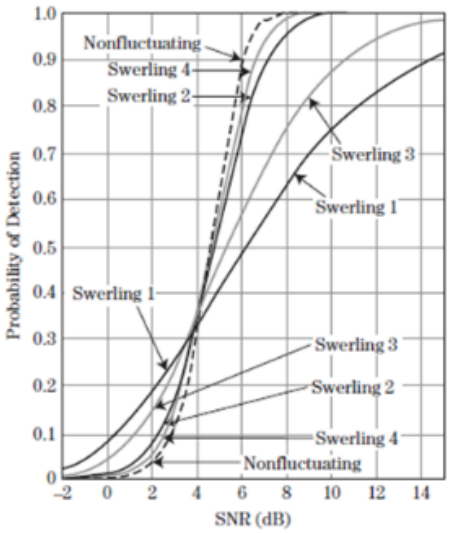

Fig. 3.7: SNR versus detection probability [19].

Summarizing, a preliminary work on an on-satellite radar system designed to detect space debris, such as VESPA, has been described. The technical details of the radar design have been presented, including the system parameters and resulting link budget. This work is part of an

ongoing project. Further activities concerning the design of the complete system, behavioral simulation and measurement will be performed.

3.2 Design of a 120 GHz MIMO radar by combining SISO ICs

This paragraph focuses on research activities involving MIMO radar systems. Initially, the 60 GHz MIMO radar by TI, presented in Chapter 2.2, was used. However, the actual intention was to design a MIMO radar that would fully optimize angular resolution. The next pages will therefore illustrate the main aspects of designing a modular 120 GHz MIMO radar composed of multiple SISO ICs [83]. Indeed, although the scientific literature reports on 120 GHz integrated circuit prototypes, until now, there are no commercial MIMO radars composed of multiple commercial SISO operating in the D-band spectrum. The design involves many challenges, indeed, the necessity to combine multiple chips with fixed dimensions and the presence of transmitting and receiving antennas on chips adds many constraints for the antenna placement and, consequently, for the virtual array design. As an example, the minimum distance between the antennas must obviously be at least equal to the chip width, which is in turn higher than half a wavelength, thus raising many concerns to fix the optimum inter-chip distance. Thus, this work can be considered as pioneering, being focused on the emerging concept of designing D-band MIMO radars by exploiting a modular approach.

As already discussed in many points of the thesis, the angle estimation capability paves the way to an in-depth and accurate analysis of the surrounding area, both on the azimuthal plane and the elevation one thanks to the presence of multiple antennas. Moreover, MIMO radars provide information on the target in a single snapshot, thus overcoming typical cons like waiting time and processing effort to carry out a complete scan in case of synthetic aperture radar [84].

Of course, the use of MIMO radar is restricted to analyzing relatively limited areas in short-range applications, whereas SAR is employed to create large-scale maps of regions on Earth for several different applications [85], [86]. Besides, the higher frequencies allow the miniaturization of antennas, which can be realized on-chip or in-package, thus enabling the implementation of highly integrated and cost-effective MIMO radar systems too.

All these aspects are continuously increasing the interest of the scientific community in the MIMO radar field. In [87], the researchers put efforts into designing an entire MMIC chipset oriented to MIMO radar application, instead, in [88] the authors worked hard to design a multichannel D-band receiver for MIMO radar with an optimized LO distribution. When designing a MIMO radar, one of the most critical sections is the antenna design, especially at higher frequencies. The [89] presents the design of a planar antenna array through a method based on the definition of element array position by a genetic algorithm and the analysis of the ambiguity function associated with the array itself. This work was carried out for a radar system with a center frequency of 76.5 GHz, enabling both the azimuth and elevation environment monitoring. Once again, the scientific interest is also confirmed by several research groups who focused on realizing new microstrip antennas tailored for millimeter-wave automotive MIMO radar sensors, as in [90]. Another example is present in [91] where RF front-end was realized in a modular way, considering 24 transmitters and 24 receivers.

This work wants to formalize the initial considerations and steps necessary to make a modular millimeter wave MIMO radar. This is the first project of a modular MIMO radar operating at 120 GHz and composed of multiple cooperating integrated circuits. Indeed, most commercial MIMO radars work within the industrial and automotive bandwidths around 60 and 77 GHz, respectively. A crucial aspect is to investigate how MIMO radar performance changes in relation to the presence of on-chip antennas and how the restriction due to the antenna

position can be exploited to enhance the radar performance. Last but not least, the willingness to use multiple SISO radar ICs will drastically decrease the design and future realization costs.

Typically, researchers design new array topologies by optimizing the position of each element to improve array performance. Different algorithms can be used [92], [93] and the research community is continuously developing new algorithms aimed at optimizing some particular aspects of arrays or exploiting sidelobes and grating lobes in novel ways, respectively [94], [95]. However, this work is not focused on designing an array by means of a new algorithm. Whereas it follows a different approach trying to elude the physical dimensions of the chips and to optimize any performance parameters in the MIMO radar field.

Keeping in mind the MIMO radar theory discussed in Chapter 1.4 and using the chip TRA_120_045 [47] introduced in Chapter 2.3, two main integrated circuits configurations to determine their best position to optimize the performance have been analyzed. The presence of on-chip antennas eliminates the need for bond wires at this very high operating frequency. The bond wires are practical for frequencies superior to 100 GHz, but the optimum length of the bond wire does not correspond to the optimum radiation pattern as presented in [96]. Therefore, the size of the transceiver has a significant impact on the positioning of the antennas because they are within the chip itself; indeed, FOV and angular resolution are affected by their spatial position. The ideal case is to have the maximum possible FOV and the minimum angular resolution in order to detect more targets in a very wide angular space. Unfortunately, this is not a trivial achievement since the higher the distance among antennas, the better the angular resolution, but the worse the field-of-view.

Thus, the main critical point is the size of every chip because the minimum distance between the antennas, d, must be at least equal to the chip width, i.e., to 2λ in case of 5×5 mm^2 integrated circuit. So, the main constraint is the minimum antenna distance due to chip

dimensions. Indeed, the antenna position is fixed inside the transceiver. This physical and more stringent limit does not permit the application of either two methods proposed in [97] where a two-step synthesis procedure is used to determine antenna array sparsity via convex optimization. The physical limitation makes it difficult to use the stochastic search method to find a very good nonuniform distribution for the array elements as presented in [98] where the goal is to find the distribution and weighting values of the array elements to minimize the sidelobe level.

Generally, the θ_{res} can be improved by increasing the number of elements in the array, as previously seen in Eq. 1.39, while keeping the $\lambda/2$ element gap unchanged. In this contribution, the idea is to exploit the 2λ constraint to achieve a superior angular resolution; however, at the cost of a reduced FOV. In Tab. 3.3, the variation of merit criteria has been reported at varying distances.

Tab. 3.3: Effect of the distance variation on field-of-view and angular resolution.

d	FOV	θ_{res}
2λ	$\pm 14.48°$	$5.73°$
3λ	$\pm 9.59°$	$3.82°$
4λ	$\pm 7.18°$	$2.86°$
5λ	$\pm 5.74°$	$2.29°$

In detail, Tab. 3.3 highlights clearly that the FOV drastically decreases by increasing the distance, instead, the resolution improves but not as clearly. The resolution at 2λ distance is already very good. Therefore, the idea is to maximize target recognition by spacing three integrated circuits of 2λ apart. The choice of three ICs was dictated by the willingness to lower the project complexity and to develop a MIMO radar operating along the azimuth plane at this

first stage exclusively. A preliminary configuration is shown in Fig. 3.8 in which the antennas are illustrated nearly as point-like in a uniform arrangement.

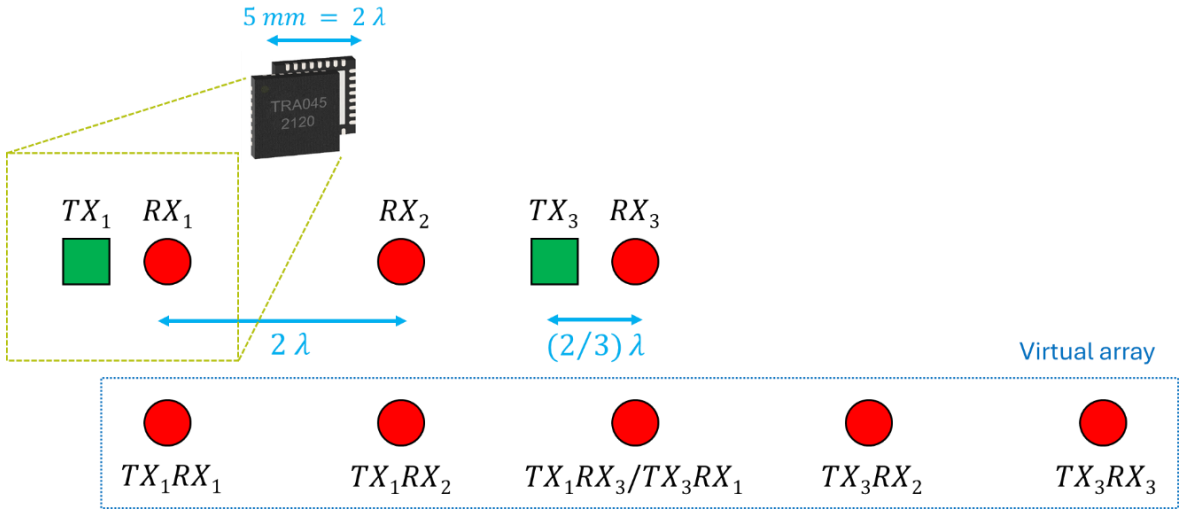

Fig. 3.8: Chips placement and its virtual array. The green squares are the transmitting antennas, the red circles identify the receiving ones. On the top left the tiny representation of the selected chip.

The green square shapes represent transmitting antennas, and the red circles identify the receiving ones. Every shape couple can be assimilated with the antennas inside each chip, which is represented with a gold hatching in Fig. 3.8. The distance between the transmitting antenna and the receiving one within a single transceiver is $2/3\,\lambda$, that is, this value is the distance between the $\lambda/4$ elements of the half wave dipole. In this configuration, there are only two transmitting antennas to avoid overlapping elements in the virtual array. If the second transmitter were used to radiate the signal, the generated virtual elements would be useless because they would present element duplication. Moreover, an energy part is saved by disabling one transmitter. Therefore, the position of each virtual element remains unchanged, the number of overlapped elements has been reduced solely. It is worth pointing out that it will be necessary to increase the distance d a little bit more than 2λ to avoid rubbing the chips. Nevertheless, d is considered equal to double wavelength to simplify calculations and analysis. Therefore, it results a 2λ distance among virtual elements starting from the first element at position 0 to the

last one at position 8λ. The 2λ corresponding FOV and θ_{res} are present in Tab. 3.3, whereas the angle resolution is 8.74° by applying Eq. 1.40. The angular resolution checking will be done in the next section by simulating the array pattern. Another possibility is to investigate a chip arrangement characterized by the alternating 180° rotation of the chips themselves, as shown in Fig. 3.9. The alternating chip 180° rotation changes the inter-antennas distance between odd and even chips but maintains constant the distance between the elements of the virtual array, i.e., the arrangement seems non-uniform only apparently. The position of every virtual element with respect to the first one is reported hereafter: 0, $2\lambda - 2/3\,\lambda$, $2\lambda + 2/3\,\lambda$, 4λ, $6\lambda - 2/3\,\lambda$, $6\lambda + 2/3\,\lambda$, 8λ. Thus, the virtual inter-antennas distance is equal to $4/3\,\lambda$ and the array is still uniform. It is curious to underline that the corresponding virtual array of each transmitting antenna is non-uniform, but all their combination generates an equally spaced array. In other words, it seems as if each singular non-uniform array would cover the non-uniformity of the others, making the entire virtual array uniform.

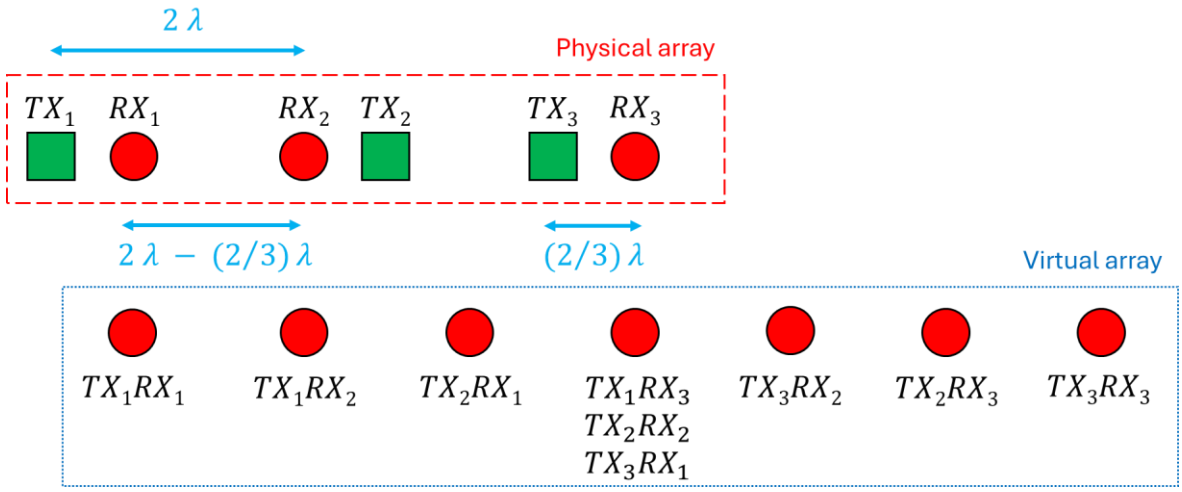

Fig. 3.9: Chips placement and its virtual array in case of the second chip rotation. The green squares are the transmitting antennas, the red circles identify the receiving ones.

It is immediately noticeable that the number of overlapped antennas is less than in the previous arrangement, if the second transmitter is not disabled. This is due to the different spacing between the transmitting and receiving antennas. Therefore, in this configuration the

second transmitter is used because it adds active elements that improve the array performance significantly. For this reason, in the first configuration it is useful to disable one transmitter for saving energy at least, while activating each transmitter to improve performance in the second configuration.

The rotation of the chip changes only the internal arrangement of the elements, but not the total aperture size, which remains equal to 8λ, as in the previous case. According to Eq. 1.40, it is expected to have an identical angular resolution. The resolution is 6.14° by calculating with Eq. 1.39. Notwithstanding the minor virtual element distance, the resolution is very similar to that of the previous antenna disposition, thanks to the increasing number of elements in the virtual array, which partially counteracts the resolution deterioration. According to Eq. 1.38, the FOV is $\pm 22.02°$ which is 50% higher than the first array disposition due to closer antennas.

Therefore, the negligible worsening of angular resolution is acceptable because it implies a significant improvement in field of view, even though it is still relatively small. Hence, a list of main points is reported below:

- Minimum distance among chips equal to 2λ in case of TRA_120_45 transceiver.
- The higher the inter-chip distance, the worse the FOV, but the better the angular resolution.
- There is very little difference in terms of resolution between the two different array topologies.
- A 50% FOV improvement by rotating the second integrated circuit.

A simulation of the array factor is crucial to confirm the calculated angular resolution and estimate the angular position of the grating lobes. Indeed, the angular resolution can also be defined as the 3 dB beamwidth of the array main lobe. It is also correlated with the ratio between wavelength and array dimensions [99].

The element spacing among the antennas directly impacts the presence and location of grating lobes [100], [101]. The expected location of the first grating lobe can be calculated by means of Eq. 3.4.

$$\theta_{GL} \approx \sin^{-1}\left(\frac{\lambda}{d}\right) \tag{3.4}$$

Thus, the first arrangement presented in this contribution will have the top grating lobe at approximately 30°, whereas the 180°-rotation solution will be characterized by a first grating lobe in 48.59° angular location.

The results are corroborated by means of the simulation, and the array factor comparison is shown in Fig. 3.10.

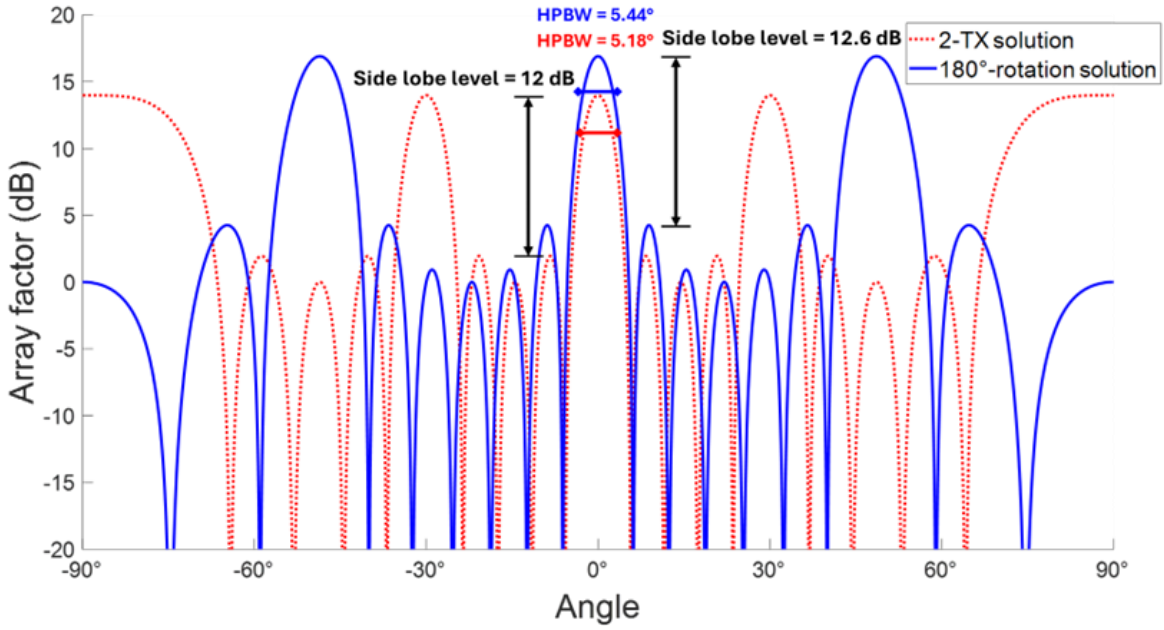

Fig. 3.10: Main lobe width, grating lobes and side lobe level of both uniform arrays.

The red dotted line represents the array factor generated by the two activated transmitters and three receivers illustrated in Fig. 3.8, whereas the blue solid line is related to the solution obtained after the 180°-rotation, where the second chip is rotated with respect to the other two as highlighted in Fig. 3.9. Regarding the side lobe level, the second array exhibits a slightly

lower level, especially near the main lobe. In addition, the blue array factor has a higher gain due to its superior number of virtual elements. Specifically, the red array presents a gain factor equal to 14 dB, instead of 17 dB for the blue array. Thus, even though the sidelobes of the blue array are slightly superior to the red ones, the total sidelobe level is favorable in the case of the blue array by a small margin. It is also characterized by fewer grating lobes that are farther away from the main lobe than the red one. This last aspect is corroborated by the larger the inter-antennas space, the higher the number of grating lobes; indeed, the inter-distance is $4/3\,\lambda$ for the blue array and 2λ for the red one. Besides, the simulation confirms the angular location of the first grating lobe for both array factors, as mentioned just above. Hence, the blue sidelobe section is larger than the red one, which ensures that the grating lobes are more distant with respect to the main lobe in the blue array factor. Furthermore, the red array factor does not have a grating lobe at an angular location of 90°. Instead, the blue array factor does not have another pronounced grating lobe after the first one. Of course, the same considerations can be drawn for the specular sections of both array factors. Depending on the application, grating lobes could be desirable and useful such as in radio astronomy for radio interferometry. For instance, a massive presence of extremely narrow grating lobes allows very small angular resolution of radio sources in the sky.

The angular resolution can be extracted by simulation considering the half-power beamwidth (HPBW) as highlighted in Fig. 3.10. The red beamwidth is 5.18°, the blue one is 5.44°. These widths validate the ones calculated with Eq. 1.39, 5.73° and 6.14°, respectively. At first glance, the Eq. 1.40 does not fit very well with the simulated results. The simulation reinforces the idea that the larger inter-distance of the first solution ensures marginally better angular resolution. Indeed, the higher element number of the second solution covers, partially, the resolution worsening due to the minor inter-antenna span. Therefore, the angular resolution cannot be

considered as a discriminating factor to make a choice between the two factors. To conclude, the best solution involves the second type of arrangement for the following reasons:

- lower side lobe level;
- less cumbersome presence of grating lobes;
- angular resolution comparable to the other presented solution;
- significant increase in terms of FOV.

It can be asserted that the 180° rotation is a smart solution to widen FOV without complicating the project. The next step was designing the board layout. The RO3010 substrate was chosen [102], and the layout was drawn in KiCad, which is the electronic design automation software used for this project. The SISO ICs were placed based on all the considerations made in the previous chapter. Above all, attention was given to the microwave section and the placement of headers and coaxial connectors to ensure mechanical stability. The design layout is sketched in Fig. 3.11.

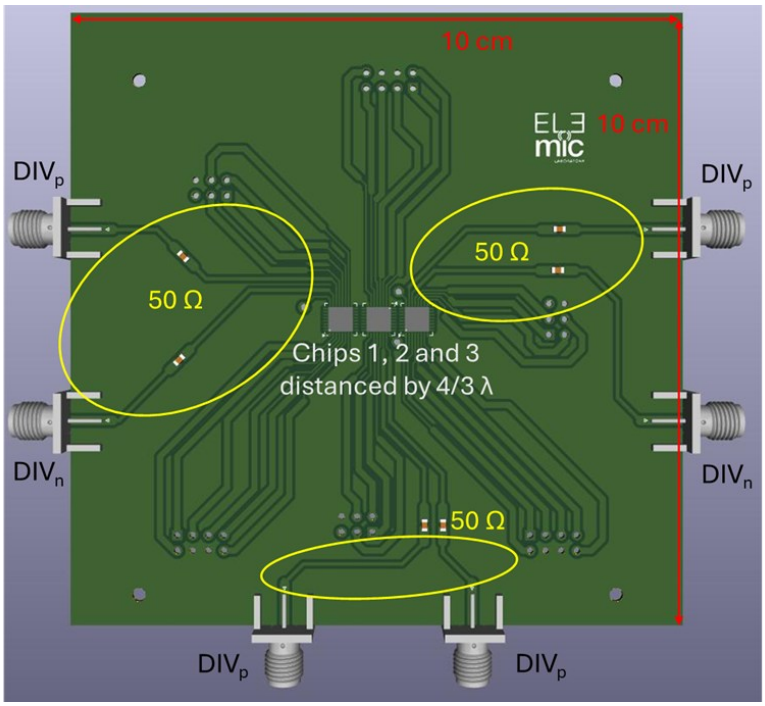

Fig. 3.11: First prototype layout of the MIMO radar system.

Specifically, the board has a length and a width of 10 cm to incorporate the chips and headers, which are not illustrated in their 3D models to only represent the key information in Fig. 3.11. The presence of three vias next to the transceivers highlights the necessity of using the bottom layer to trace a few paths. There are six microwave paths, two for every chip on the board, to make the divider outputs available for each transceiver. These outputs can be exploited to check that every transceiver is working properly when the radar board is realized, for example, using a spectrum analyzer. It is expected that the divider output frequency ranges from 1.73 GHz to 2.15 GHz, as confirmed in [47]. A capacitor is present in every microwave section because an external decoupling capacitor is required, as can be noted in the datasheet. Consequently, these brief microstrip paths were designed by using the AWR Design Environment Platform by Cadence, ensuring a 50 Ω impedance as much as possible along each microwave path to obtain an input reflection coefficient below the value of -10 dB [17]. In fact, the track dimensions of the microwave section were properly selected. Additionally, the microwave connectors were arranged with that orientation to guarantee mechanical stability of the board. The chips were placed in the center to have more space around them to facilitate the paths of each signal. For the sake of brevity, the simulation of the microwave section has not been reported.

Despite being a different contribution, this work and [89] try to design an array for MIMO applications with a different approach and tasks. It is worth noting that this contribution aims at designing a 120 GHz MIMO radar, which is more challenging compared to 76.5 GHz operative frequency in [89] due to the small wavelength that complicates the array design. Moreover, the estimated angular resolution in the azimuth plane is 15.15°, quite higher than 6.14° of this project. Our solution is characterized by a lower side lobe level, around 6 dB vs 12 dB in absolute value. In any case, in [89], the researchers applied a genetic algorithm that is

specialized for a 2D MIMO radar optimization, in which a gene represents the antenna element position on the plane. All the genes represent a single full 2D MIMO array configuration, the so-called chromosome. Consequently, they set some constraints in the algorithm to optimize the performance. Once again, the comparison cannot be deepened further because this contribution focuses on exploiting the physical dimensions of each chip as an advantage to cut design costs rather than designing an array using a new algorithm.

Similar considerations can be drawn comparing this contribution to [98], [101]. In [98], the nonuniform distribution of the array elements was optimized by means of a stochastic search method. The goal was to find the distribution and weighting values of the array to obtain the minimal sidelobe level with some constraints for the main lobe location and width.

In [101], a similar MIMO radar is designed. Even here, the researchers positioned the array elements freely, without any physical constraints. Consequently, their work is different from this approach, which addresses the possibility of using already existing transceivers on the market.

In any case, continuous research is conducted to find a balance among several parameters, limitations due to the application and those imposed by the recommended solution. This comparison highlights that the results of this contribution are comparable to the previous research merely in spite of very strict physical limitations and by employing commercial transceivers. Thus, no additional RF design efforts were necessary.

Finally, the large available bandwidth of the transceiver could be exploited to suppress aliases caused by grating lobes, i.e., the use of different sub-bands can allow to distinguish targets due to the main lobe with respect to the ones generated by grating lobes [103] mitigating their effect on this project too.

Therefore, the current paragraph outlines the main steps required to realize a MIMO radar composed of ready-to-use SISO integrated circuits. This work did not follow an existing algorithm for designing the array due to the physical dimensions of the chip and the position of the antennas within the package itself. This different approach permits to cut the costs of designing a MIMO array that operates in the D-band spectrum. Of course, several other aspects must be considered in the next phases of the design like chip synchronization, the design of a suitable base-band board and the acquisition and management of the data samples via a microcontroller or FPGA. Besides, it will be essential to apply a calibration technique to the sparse array in order to compensate for the amplitude and phase offsets among the signals received by each antenna.

3.3 Enhanced phase detection

One of the main issues that arose during the PhD program was to improve the phase detection to make the target displacement reconstruction more reliable. This topic acquires more relevance in the case of AC-coupled CW radars. If measuring the motion extent of a single moving target can be considered a quite acknowledged task [104], [105], the automatic motion detection of a target alternating between stationary and moving intervals gives rise to some concerns. For AC-coupled Doppler radars, the level of the direct current (DC) signal is usually reduced to a fixed bias voltage by means of a high-pass filter stage. Due to the presence of thermal noise fluctuations and the resulting uncorrelated phases, the extracted phase history will evolve randomly. So, a null-Doppler frequency results in a very poor SNR which leads to an incorrect evaluation of the displacement target [106], [107]. In addition, during real-time measurement, the estimation of target displacement is not a trivial task [108], even as the target

is in constant motion as discussed in the last part of the current paragraph. This task has been widely discussed in the literature, but many articles do not deal with the possible incorrect displacement estimation when offline algorithms are applied to real-time measurements, involving inappropriate unwrapping. This generates wrong displacement detection and phase drift that are often solved with post-processing algorithms and erroneously attributed to accumulated noise and hardware imperfections. This contribution aims to investigate the origin of possible errors and give a simple but effective solution to correctly estimate the target displacement. The reported algorithm can be applied to both FMCW and Doppler radars. Therefore, this section provides a thorough analysis of these problems in the trickiest case of portable Doppler radars and offers potential solutions.

The foremost studies are focused on the challenge of phase detection if the target alternates between stationary and moving time intervals. Indeed, the uncorrelated phases, which might be confused with the real target displacement, can be avoided by keeping the radar continuously moving [106], thus exploiting what is usually considered a negative state. Secondly, this problem has been resolved with a new algorithm that recognizes when the target is moving and when it is not, reconstructing the object displacement properly [107].

In [106], the mixing between the LO and the received signal will always be different from zero, except in the unlikely case that the target has exactly the same speed as the radar but in the opposite direction. In the scientific literature, radar motion is often considered a negative state, e.g., for the task of vital sign detection while the radar is mounted on a moving platform, such as an unmanned aerial vehicle [109], [110]. Indeed, when the radar moves, the relative range detection is often many orders of magnitude larger than the desired signal and needs to be corrected. This often requires implementing techniques to obtain the movement of the radar itself which in turn can be subtracted from measured data [111]. On the other hand, a small

number of works deal with intentionally leveraging the radar movement like in [112]. As an example, in [24], the authors take advantage of the radar movement to find the target direction with a single-input single-output Doppler radar. To clarify, the induced Doppler shift involves different Doppler returns from echoes at different angles, which can, in turn, be exploited to obtain angle detection capabilities with small aperture antennas.

Before presenting the two solutions, a simulation was performed to illustrate the negative impact of noise fluctuations on displacement reconstruction. Thus, when the target is stationary, the null-Doppler shift results in a DC level present at the outputs of the mixer. Although theoretically this would result in a flat phase history, the noise fluctuations will generate uncorrelated phases, leading to incorrect displacement detection. The simulation involved a target placed 15 cm from the radar. Initially the target is still, then it starts moving 16 cm away from the radar and, thereafter, 12 cm towards the radar. A radar operating within the 24 GHz ISM bandwidth was simulated, and the SNR was chosen to reproduce a real-life scenario. The extracted phase history, in the case of absence of thermal noise, is reported in Fig. 3.12(a). It is worth noting that in this ideal case, the phase history can be properly detected by applying the arctangent demodulation.

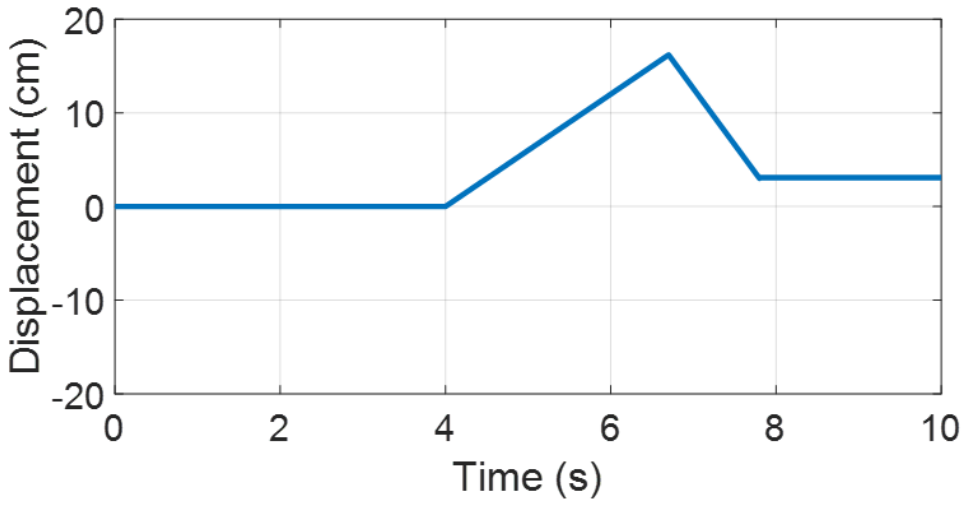

(a)

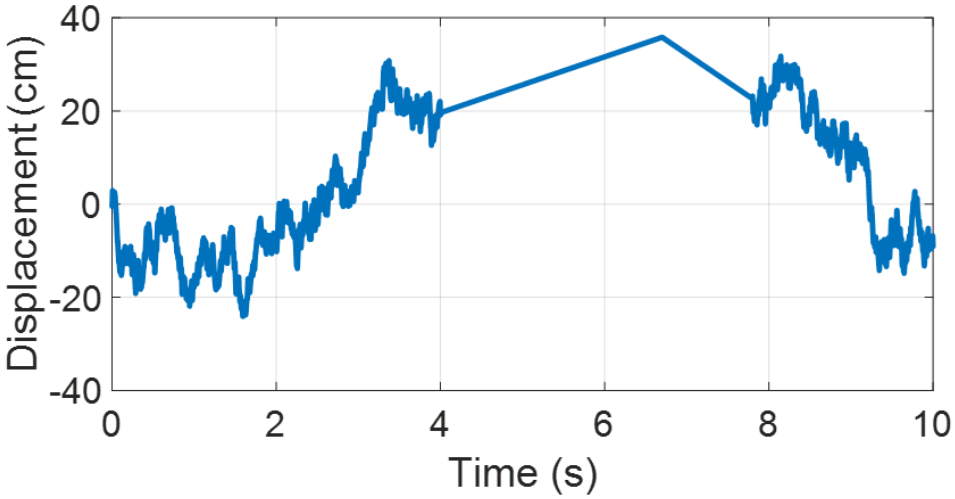

(b)

Fig. 3.12: Simulated target displacement (a) without and (b) with noise.

On the other hand, the introduction of thermal noise leads to an incorrect evaluation as illustrated in Fig. 3.12(b). When the target moves, i.e., between 4 s and 8 s, the relative displacement is properly calculated. Nevertheless, the thermal noise fluctuations generate a wrong and random estimation of the displacement, which instead should be equal to zero when the target is steady. In Fig. 3.13, the I/Q data during non-consecutive stationary and moving intervals are both reported in the constellation graph.

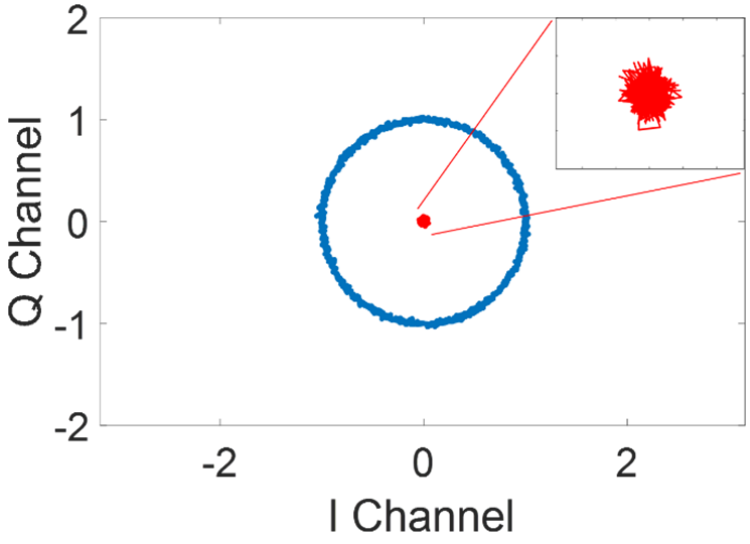

Fig. 3.13: Simulated I and Q channels during movement (blue) and stationary (red) intervals. In the inset, the enlarged detail of the stationary interval.

During the motion interval, the blue samples exhibit noise fluctuations around the ideal value. However, their amplitude is greater than the noise level, so it does not overwhelm the useful signal not corrupting phase information. Whereas the red data during the stationary time, highlighted in the inset, show a random phase. Moreover, a shift of the initial phase is also introduced, thus leading to a wrong final relative position of the target.

After this brief analysis, the first approach was to examine the effect of radar motion during the measurement of small displacements. For this purpose, the TRA_120_002 in Chapter 2.3 is intentionally moved by means of a controlled mini-actuator in CW operation mode, while measuring the target displacement. Thus, the first possible solution is to solve the problem by moving the radar during the measurement.

In this way, recalling Eq. 1.11 and 1.12, the I/Q signal expressions change as reported in Eq. 3.5 and 3.6.

$$s_I(t)' = \alpha \cdot \cos\left(\Delta\varphi \pm \frac{4\pi \cdot x(t)}{\lambda} \pm \frac{4\pi \cdot r(t)}{\lambda}\right) \tag{3.5}$$

$$s_Q(t)' = \alpha \cdot \sin\left(\Delta\varphi \pm \frac{4\pi \cdot x(t)}{\lambda} \pm \frac{4\pi \cdot r(t)}{\lambda}\right) \tag{3.6}$$

where $r(t)$ is the displacement introduced by the continuous radar motion. The presence of the term $r(t)$ imposes an ever-present signal at the output of the mixers, involving the correct measured phase histories. Of course, the radar motion affects the displacement detection by adding an additional apparent target movement which needs to be corrected.

The system, composed of radar, mini-actuator and metallic target, is photographed in Fig. 3.14. The Doppler radar, shown in the inset on the right side, has been mounted on an actuator moving at a constant speed of 10 mm/s for a total measurement time of 5 s.

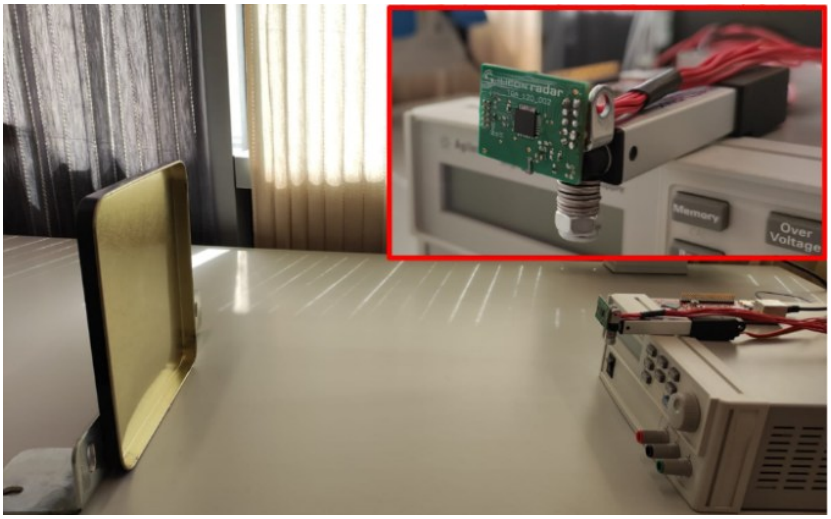

Fig. 3.14: Picture of the experimental setup.

The target is a 20 cm × 20 cm metallic plate. The small dimensions of the radar, due to the high working frequency, are very beneficial for reducing the weight of the system, thus minimizing possible unwanted vibrations during the motion periods.

Due to the presence of the wavelength in Eq. 3.5 and 3.6, it is worth analyzing the performance dependence on the frequency stability. The output frequency of the TRA_120_002 can be controlled by four VCO tuning inputs. The stability of the frequency depends on the supply voltage and temperature. The dependence on the supply voltage can be neglected. Indeed, the supply voltage is the output of a stable voltage regulator, and the chip exhibits an average output frequency shift lower than 100 MHz for a 0.3 V voltage drift, which is of course an overestimate value for a voltage regulator. On the other hand, the temperature dependence is usually considered a critical factor for the output frequency stability. The chip exhibits a 1 GHz average shift for quite a wide temperature range, i.e., from 10 °C to 90 °C. This seriously affects the performance of FMCW radars, but it can be also considered negligible in this scenario [113], [114], [115]. According to the component datasheet, the frequency shift is around 15 MHz for each 1 °C of temperature drift. For instance, by considering an excessively negative scenario, i.e., 1 °C drift per second, since the data are acquired every 10 ms, the

frequency shift will be approximately 150 kHz per measurement. Consequently, the wavelength shift will be approximately 3 nm per measurement. Given the $\lambda/4$ maximum displacement discussed in Chapter 1.2, the resulting displacement error is about 0.76 nm per measurement, which is a negligible value in this context.

The controlled radar movement is measured from the echo of a stationary target and subtracted from the next measurements, thus removing the effect of the radar motion on the displacement and correcting the desired data. Figure 3.15(a) shows two different measurements, performed on a stationary target, to test the procedure effectiveness and repeatability. According to the previous analysis, since the radar is moving for the first 5 s and stationary during the next 3 s, different results on the phase extraction are expected.

To clarify, during the radar movement, i.e., up to 5.2 s, the correct zero-displacement can be extracted after the displacement removal due to the radar motion itself. Instead, when the radar is stationary, i.e., from 5.2 s, both measurements show random and uncorrelated phase histories, resulting in incorrect displacement detection, as evidenced in the final part of Fig. 3.15(b).

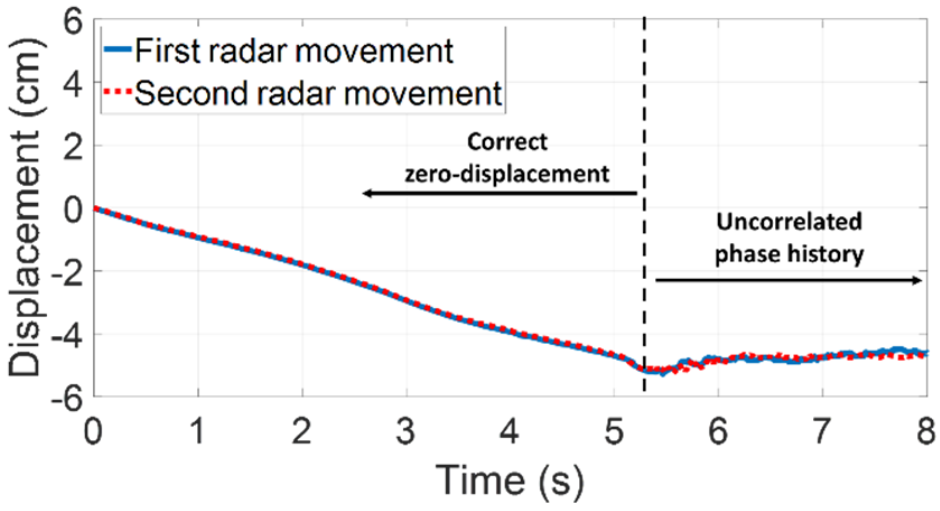

(a)

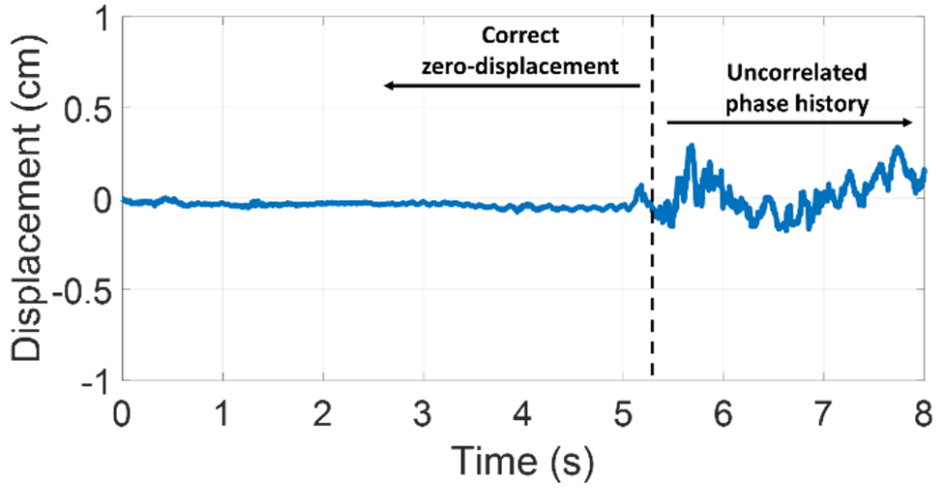

(b)

Fig. 3.15: (a) First (blue solid line) and second (red dotted line) displacement from a stationary target and (b) difference between the two measurements.

Thereafter, the system was tested with a metallic plate moving 1.2 cm back and forth. Due to the continuous radar motion throughout the entire measurement, a down-converted signal with a non-zero Doppler frequency is always present. Consequently, the phase history extraction with the arctangent demodulation always makes sense, as highlighted in Fig. 3.16. After removing the radar motion effect from the data, the desired results are obtained and the markers in Fig. 3.16 highlight the maximum distance covered by the plate.

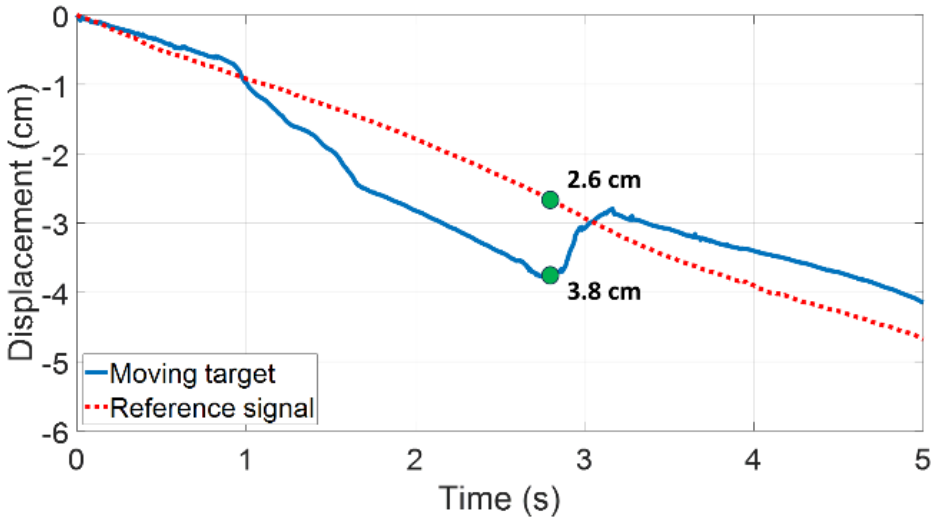

(a)

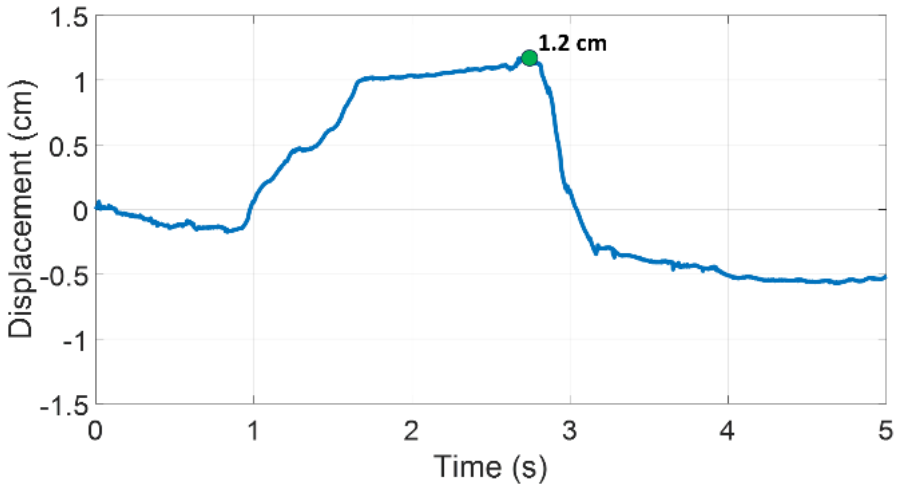

(b)

Fig. 3.16: (a) Reference signal (red dotted line) and measured displacements from an alternating moving target (blue solid line) and (b) difference between the two measurements.

Thus, the intentional radar motion is exploited to extract the real target displacement. Indeed, a noisy contribution is usually present at the output of the receiver for AC-coupled Doppler radars when echoes from stationary targets are received. This leads to incorrect displacement detections, but this negative effect is suppressed by keeping the radar continuously moving, thus positively exploiting what is usually considered a negative condition.

This solution can be very useful because it enhances the phase detection. At the same time, it can be uncomfortable because it requires an actuator or something similar. Sometimes, the radar is placed in an impractical location such as in automotive field for in-cabin detection applications [11], [12], in industrial and civilian applications [82], or on goggles as will be seen in Chapter 3.6 [3], [4]. From this point comes the need to find a more practical solution. In [107], a simple and cost-effective solution is proposed to automatically highlight only the real target movements thus discarding the random phase evolution when the target is stationary. First, this issue is investigated by simulating a possible scenario. Then, the effectiveness of the solution is tested in a real case. Reconnecting to what is shown in Fig. 3.12 and 3.13 via simulation, a solution is proposed with a twofold task:

1. Avoiding wrong phase detections when the target is stationary as shown in Fig. 3.17(a).
2. Realign the initial phase when the target starts to move as illustrated in Fig. 3.17(b).

One limitation of the classical phase analysis is that the phase itself does not include any information concerning the intensity of the received signal. This makes it impossible every attempt to discriminate between the stationary and the moving intervals based on the signal intensity.

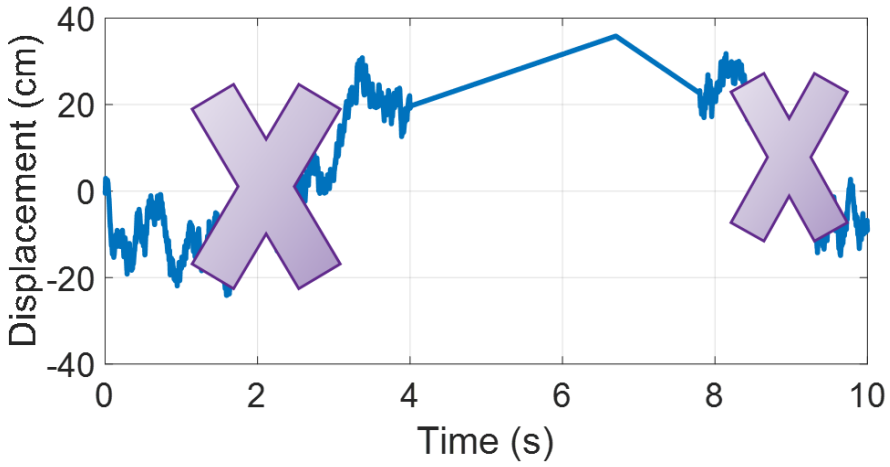

(a)

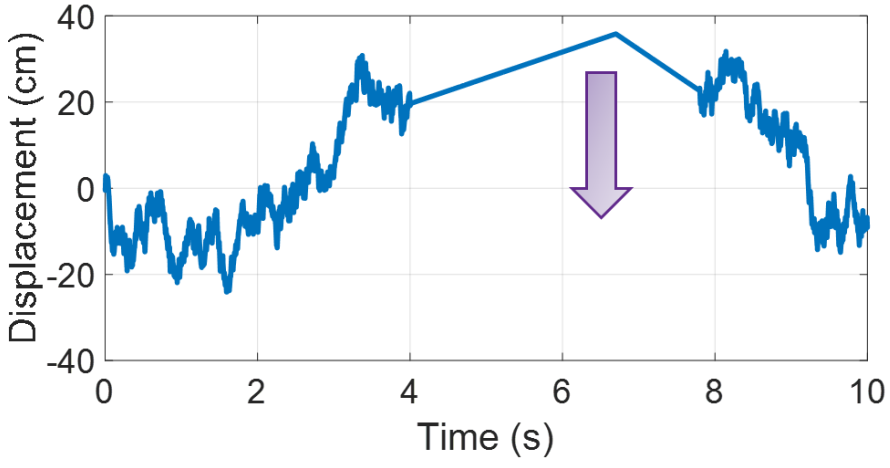

(b)

Fig. 3.17: (a) Elimination of incorrect displacement evaluation during stationary moments and (b) realignment of the entire motion.

The proposed algorithm is based on the idea of creating a new data matrix that includes displacement data and signal intensity information over time. Specifically, the displacement data will be proportional to the absolute values of the I/Q data. This change transforms the phase history vector into a phase history matrix because the signal intensity is now automatically associated with the phase history. Obviously, steady target intervals are characterized by low-level I/Q signals compared to those of moving targets as highlighted in Fig. 3.18, which is a 3D plot for the displacement albeit visualized in a 2D format.

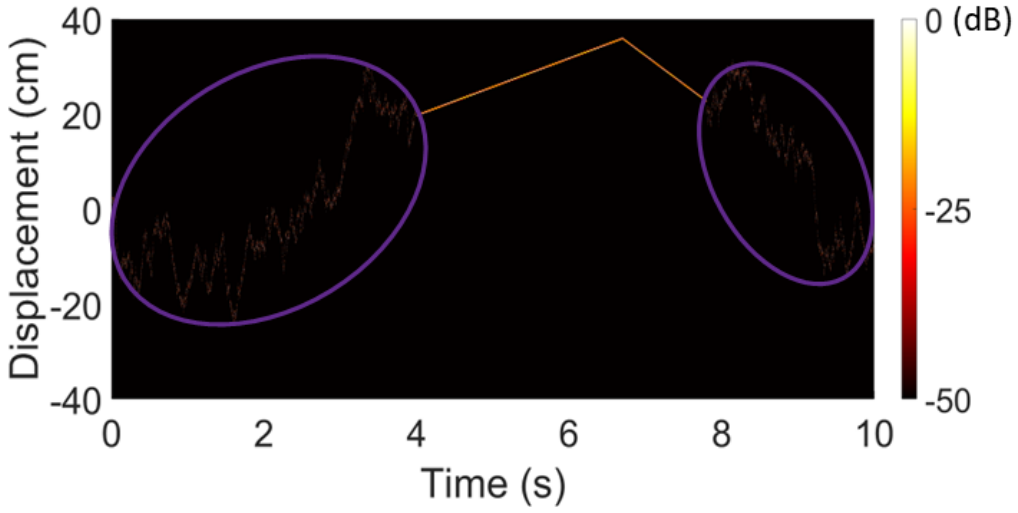

Fig. 3.18: Simulated displacement evaluation after the first part of the algorithm.

Therefore, the output of this step is a matrix whose rows always contain zero except for the rows corresponding to the measured phase history which include the absolute value of the I/Q signals versus time. Up to 4 s and after approximately 8 s, the detected phase history is not reliable due to the lower signal intensity. This first step has the great feature to be fully automatic and independent of a specific application, thus minimizing the computation costs and mistakes due to a wrong selection of the algorithm parameters. Therefore, the difference in signal intensity will be exploited as the key to separate moving moments from stationary ones.

In fact, the second step of the algorithm identifies the correct starting point of the phase history. Contrary to the first step, it requires the definition of a threshold to separate moving

from stationary intervals, which was made easier by the first step of the algorithm. Thus, the optimum threshold is related to the absolute value of the signal allowing to apply one of the many thresholding algorithms available in the literature [116]. At the beginning of the measurement, the first correct phase value is set to zero. Then, the algorithm checks if the next phase intensity overcomes the threshold. If not, the algorithm realigns the data according to the last reallocated element, thus discarding the phase estimation resulting from noise. Indeed, these data have been corrupted by the noise and do not represent the real displacement of the target. Conversely, the data above the threshold are considered correct values because they represent the actual movement of the target and are maintained. These data are realigned with respect to the motion of the target. In Fig. 3.19, the displacement obtained by applying the algorithm is compared with the initial displacement pre-algorithm of Fig. 3.12.

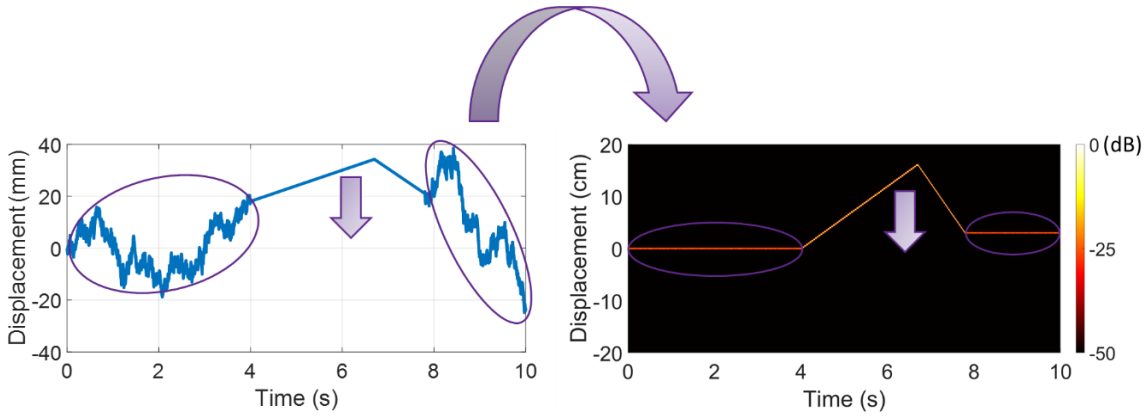

Fig. 3.19: Displacement evaluation after the second step of the algorithm in the simulated scenario.

As discussed previously, the optimum threshold might be selected depending on the case study and the algorithm fits very well with short-range applications. It is worth noting that the negative effects of the thermal noise are limited without altering the information.

Afterwards, the algorithm is applied to a real-world scenario employing the radar by Infineon presented in Chapter 2.1. Its 24 GHz operating frequency is consistent with the simulations. As shown in Fig. 3.20, the displacement estimation is incorrect except when the target is moving,

i.e., approximately from 4 s to 8 s. The user has reproduced a movement like the simulated one moving a hand in front of the radar. Thus, it is characterized by an initial motion away from the radar and, after, towards the radar as sketched on the right side of Fig. 3.20.

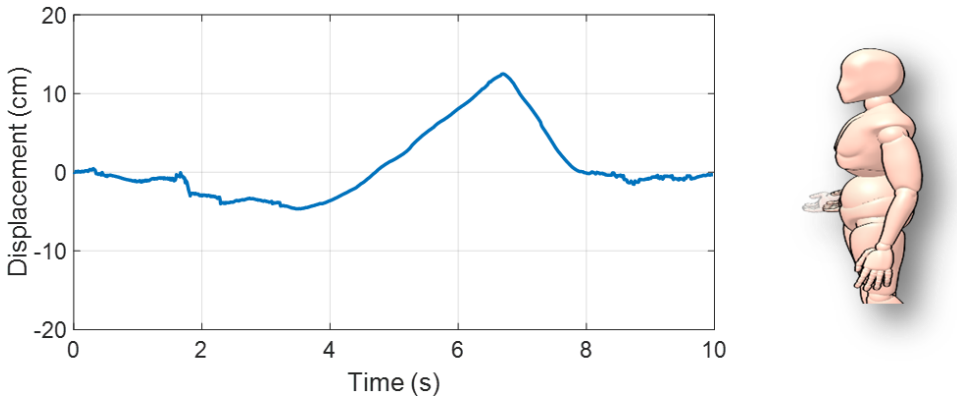

Fig. 3.20: Target displacement in the real-world scenario.

Then, the algorithm is applied to the raw data. In Fig. 3.21, the 3D-displacement obtained after applying the algorithm is compared to the pre-algorithm displacement shown in Fig. 3.20.

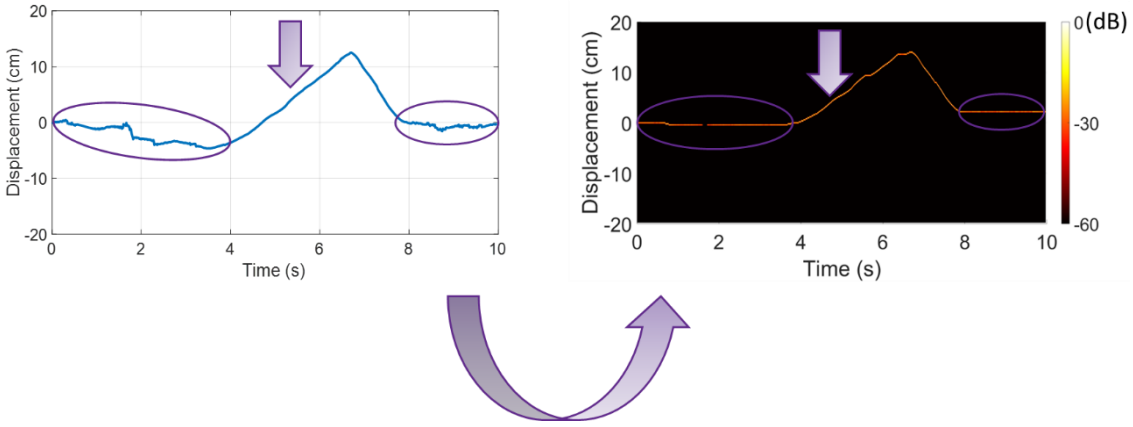

Fig. 3.21: Hand displacement after the application of the algorithm in the real scenario.

Therefore, the algorithm corrects the motion of the target and preserves the undesired random movement and stationary intervals as well. Indeed, in the first part of the measurement there is a tiny but real motion that is detected and maintained because it overcame the threshold. It was probably due to a vibration of the hand. The subsequent elements are reallocated in function of this unexpected small displacement which, in turn, shifts all the successive elements

slightly. As a consequence, the desired hand motion does not start exactly from zero. Besides, the target motion is also characterized by the presence of short stationary time intervals, which are automatically kept unchanged. This algorithm will be reapplied in Chapter 3.6 for eye blinking detection, providing a further example of its validation.

In order to complete the overview of improvements to phase detection, the aspect related to real-time measurements must be analyzed. The next pages will provide some insights on how the target motion can be properly elaborated during real-time measurement [108]. Generally, the elaboration of radar raw data is performed offline to facilitate the measurement process and execute a custom elaboration with relaxed timing requirements; quite the contrary, estimating displacement during a real-time measurement involves possible information loss about the phase of the raw data. In detail, errors can arise if the unwrapping algorithms are applied as in offline measurements. Mistakes lead to the displacement drift, causing a wrong evaluation of the target motion. Although displacement reconstruction is necessary in several different applications [3], [4], [11], [12], its implementation during real-time measurement is not a trivial task. Researchers have extensively investigated displacement estimation, but mainly through offline elaborations. This represents a great lack in literature because many commercial present and future applications related to healthcare sensing are based on real-time and not offline measurements.

As already discussed in Chapter 1, the received and down-converted data are frequently reorganized into data sequences. For instance, in the context of FMCW radar, data is separated into chirps and frames; similarly, in Doppler radar, data is packed to be properly transferred and processed, thus extracting the target phase history. However, phase histories from different frames must be linked to provide the correct and continuous visualization. Arctangent, Eq. 1.13, is often used to extract the phase history but, although the phase is limited between the interval

$[-\pi;\pi]$, the phase history is not; this requires employing the unwrapping function as detailly analyzed in Chapter 1.2. Data division and union may give rise to an incorrect application of the unwrap function: in a nutshell, the phase history of the data may be lost despite every single part of the data being elaborated correctly.

The final part of this chapter aims to investigate the aspect of preserving the phase relationship between the different data blocks. It is worth noting that this error can be relevant or small depending on the case. This can be very detrimental because subtle errors are very difficult to unmask but nevertheless capable of affecting the accuracy of the radar measurement, particularly for micrometer motion sensing [117]. In [118], [119], [120], the authors use an FMCW radar for real-time measurements and try to estimate the displacement due to the small movements of the targets, but their contribution is often confined to the representation of the in-phase and quadrature amplitude over time. In addition, these articles highlight the presence of unknown phase drifts eliminated by using the phase difference procedure, which replaces the outliers with some interpolated values. Outwardly, these works can be affected by the aforementioned errors that the authors corrected with post-processing algorithms, without investigating their origin.

On the other hand, some contributions have already investigated and clearly explained the processing steps required to evaluate the displacement both offline and in real-time, but no examples highlight the importance of maintaining the correct phase relations between different chirp blocks. For instance, [121] presents detailed offline and real-time data processing methods without paying attention to the possible errors arising from an incorrect application of the unwrap function originating from the wrong raw data combination during real-time measurement. In addition, the contribution aims to give a deep description of how the unwrap function works and how it can be applied. The application of the unwrapping steps for offline

detection is considered a consolidated task, but there is a lack of details and precautions to accomplish the different demands of real-time applications, i.e., how it works and how to prevent the possible incorrect displacement estimation.

Therefore, the purposes of this work and its main contributions to scientific literature are:

- Highlighting the difference and particular care required when dealing with real-time sensing compared to offline detection.
- Real-time applications require continuous data stream from packed data. Subtle and hard-to-find errors can arise if the unwrapping step is not properly applied between different sequences. This step is carefully analyzed, and the correct rigorous procedure is described.

The proposed solution allows for displacement reconstruction by avoiding the manipulation or interpolation of phase content, thus preserving the actual information from the radar system towards the elaboration unit. Since this issue does not depend on the radar sensor type, e.g., Doppler or FMCW, in this contribution, it has been investigated for the case of CW radar, to analyze a general case and for the sake of clarity.

Even though the phase/displacement reconstruction steps outlined in Chapter 1.2 are effective during offline processing, additional care is required when applying the unwrapping algorithm during real-time measurement. First of all, the raw data are usually collected and elaborated in blocks for both Doppler and FMCW radar sensors, as illustrated in Fig. 3.22.

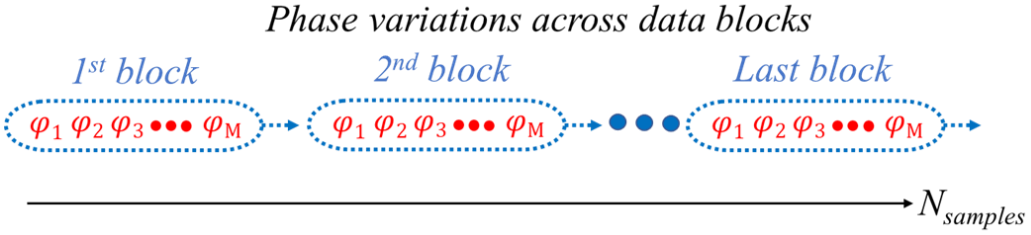

Fig. 3.22: Phase samples collected in data blocks.

After pre-processing the real-time raw data to obtain the phase of each sample, the unwrapping operation is carried out on the first data block. Presuming the absence of speed ambiguities, the phase extraction of the first data block is always correct. Subsequently, the unwrapping operation is carried out exclusively on the second data block without taking into account that the first sample phase of the current data block must be unwrapped with the last unwrapped element of the previous block. Therefore, applying this offline procedure to real-time data, the phase relationship between two consecutive data blocks is lost because, basically, the unwrap function has been applied only on the phase elements inside every block. To highlight the error, an ad-hoc simulation was performed, as shown in Fig. 3.23.

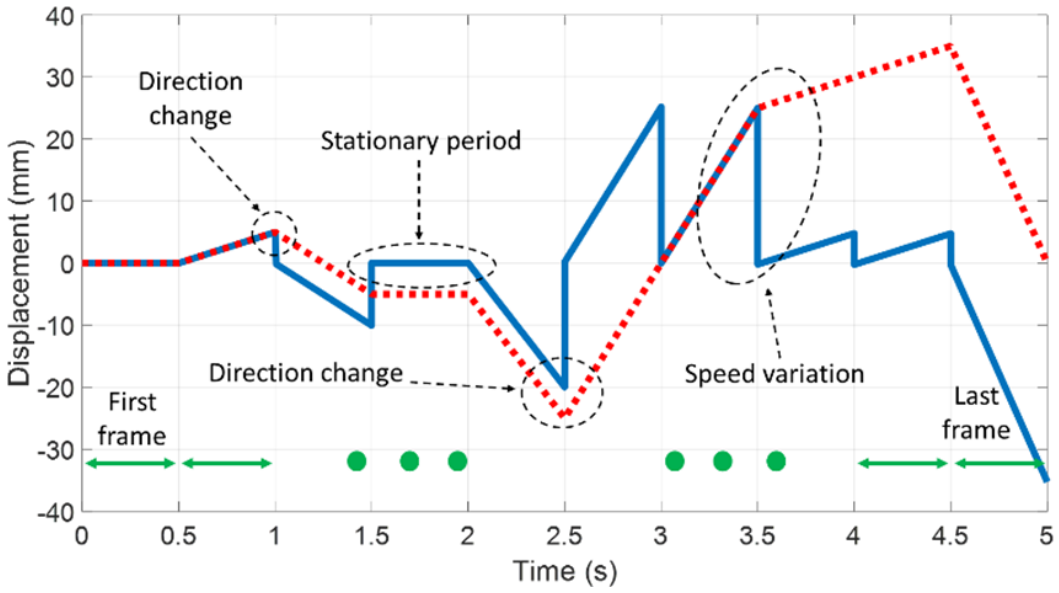

Fig. 3.23: Wrong (blue solid line) and correct (red dotted line) displacement reconstruction.

The simulation is characterized by a generic target motion in front of the radar depicting the comparison between offline and real-time elaboration. The target is initially stationary and later it moves, changing the motion direction multiple times during the simulated time, as illustrated with the red dotted line in Fig. 3.23. This line represents the target motion extracted by means of an offline measurement and the subsequent elaboration. Instead, the blue solid line is the estimated displacement applying the offline algorithm to real-time measurement raw data, i.e.,

block by block. In this simulation, a frame is a collection of phase samples with a duration of 0.5 s, as highlighted by green arrows. The simulation includes different situations: stationary period, approaching target, receding target, direction change and speed variation. The blue solid line is wrong, as can be noticed trivially. Beginning with the first frame couple, the error is null because the target is stationary and, in this case, the phase difference between the last unwrapped element of the first frame and the first element of the second frame is zero or, anyway, minor than π. As mentioned above, the unwrap function is not applied between the frames, but in this first instance, the error is absent because the phase difference is minor than the absolute value of π, regardless of the type of measurement, i.e., offline or real-time. The situation is completely different between the next two frames. Due to the same movement of the target, the phase is continuously increasing and, as a result, the phase difference between the last unwrapped element of the previous frame and the first element of the subsequent frame is higher than the absolute value of π.

When the unwrap is applied on the last frame, the phase relationship with the previous one is lost: the phase of the first sample is calculated as a value between $-\pi$ and π, and the displacement is scaled appropriately. Its value appears to be zero, but it is always different according to the calculated phase value. This sensation is reinforced by the very high operating frequency of the radar sensor in the simulation, i.e., 122 GHz. This frequency has been chosen as the optimum one to highlight the impact of elaboration errors in the displacement evaluation. In fact, the π-limit corresponds to a quarter wavelength and the higher the frequency, the smaller the wavelength itself.

The rest of the displacement extraction is affected by mistakes every time a frame transition occurs and if the phase change is higher than the absolute value of π, and it is completely independent of the target movement typology, as highlighted in Fig. 3.23. It is worth remarking

that the mistake committed is not negligible, indeed, there could be both sensible underestimation and overestimation of the displacement.

The crucial point of the real-time displacement elaboration is the unwrapping between the first element of every frame compared to the last element of the previous frame. Thus, the solution focuses on this aspect, and its key parts can be summarized as follows: a) saving the last unwrapped phase of the previous frame; b) unwrapping only the first element of the consecutive frame with the saved one. This is graphically described in Fig. 3.24.

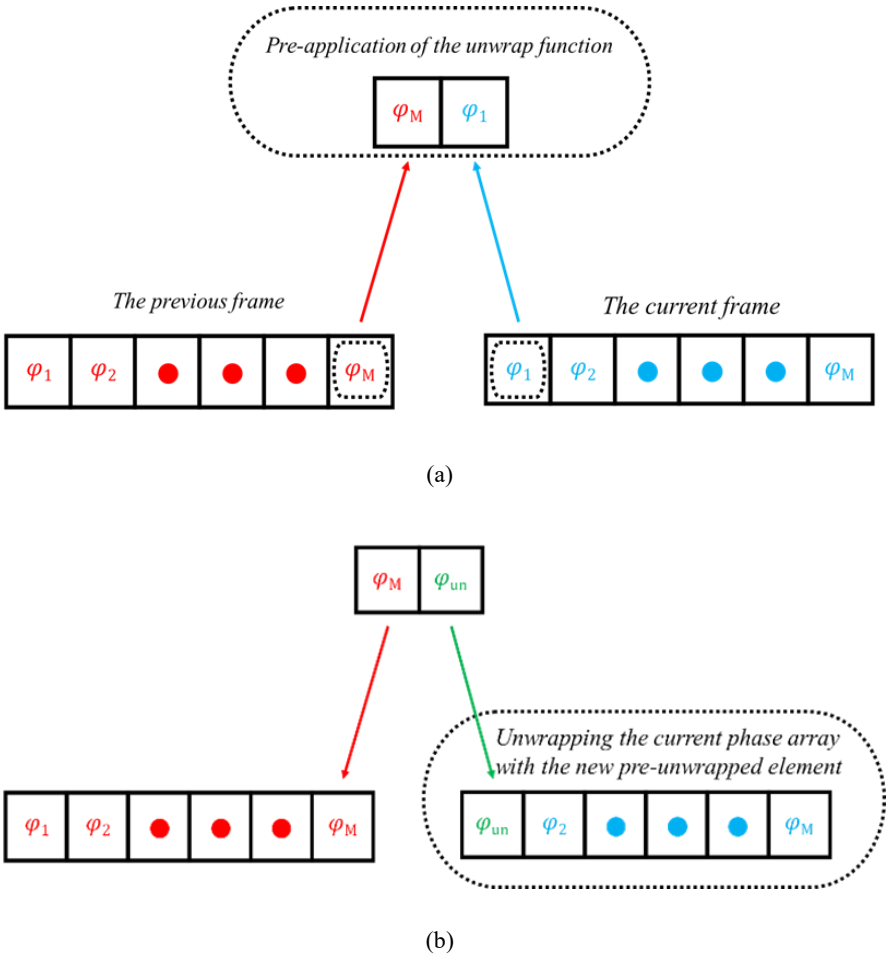

Fig. 3.24: First step of the proposed algorithm (a) and the related second step (b).

Thereafter, the new unwrapped element is the first element of the current frame and the unwrapping function is applied to the remaining elements as usually performed during the classic offline elaboration, as highlighted in Fig. 3.24(b). This solution must be applied to each

block of data, while being computationally light. This is very important, particularly during real-time measurements that require high-speed calculus capabilities. Therefore, this new solution extends the unwrap function also among the frames, tracking their phase relation.

Furthermore, the suggested algorithm does not require any manipulation of the data or change in phase content as occurs, whereas, in [118], [119], [120]. Of course, the methods used in these contributions are valid, but they produce interpolated phase values to rebuild the target displacement rather than preserving the original information, as the just-illustrated new algorithm does. Naturally, the phase content can be distorted by several defects in the circuit and due to disparate motivations [122], [123]. Therefore, the intention is to remove one possible alteration of the phase content and, in turn, target motion.

To verify the effectiveness of the proposed method, the previous ad-hoc simulation is proposed again, now with the unwrap correctly applied. The results are illustrated in Fig. 3.25. The algorithm links the phase information between the data blocks; indeed, the green dashed line obtained by the new method follows the red line perfectly, without any errors.

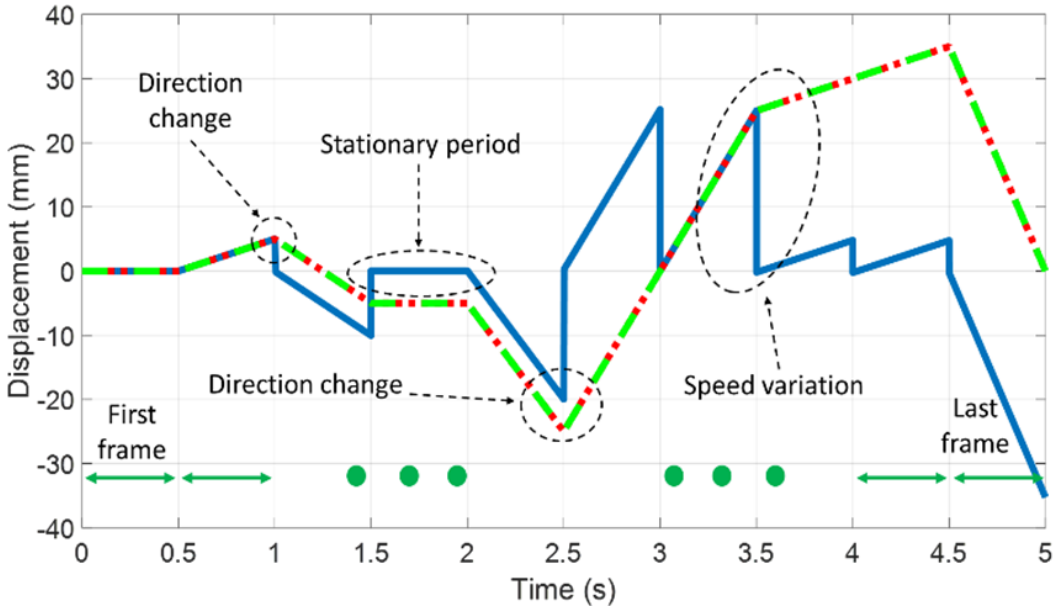

Fig. 3.25: The displacement reconstruction by means of: offline measurement and elaboration (red dotted line), real-time measurement and offline procedure (blue solid line) and by real-time measurement and its ad-hoc processing algorithm (green dashed line).

Therefore, applying the offline procedure to real-time data is like not applying the unwrapping operation between data blocks. As a consequence, the mathematical error will be proportional to the extent of the target movement at the end of the data block itself. The verification of the proposed solution was carried out by applying the algorithm during real-time measurement, but this topic is discussed further in Chapter 3.5 regarding displacement reconstruction during respiratory activity. The algorithm is applicable in any elaboration machine due to its minimum impact in terms of memory and processing requirements. The new elaboration steps are not affected by possible mistakes because they do not alter the radar raw data and phase information, thus ensuring the algorithm robustness is absolute.

Throughout this chapter, new improvements to the displacement elaboration have been presented. Combined with the micro-Doppler signature tool discussed in Chapter 1.2, these new features greatly enhance the detection capabilities of radar sensor systems.

3.4 Gesture recognition

Portable radars are having a disruptive impact on different fields related to contactless sensing. For example, the automotive field is interesting not only for autonomous driving, but for in-cabin detection applications too [11], [12]. Gesture recognition is a key aspect to enable users to interact with objects. Moreover, the accurate tracking of hand gestures is fundamental to enabling interactions in virtual environments [8]. As previously mentioned, combining a micro-Doppler signature with phase history paves the way to a better classification, for example, of gestures. The current paragraph aims to describe their recognition both to increase security in-cabin environment and enable touchless smart interactions with other objects.

The first case study concerns the topic of in-cabin detection. Since the production of the first car, the world has seen an exponential increase in electronic devices within the vehicle aimed at enhancing passenger safety and comfort. In recent years, the concept of the autonomous vehicle has revolutionized the next-generation car mobility, including the driver role. The increased level of automation is not only limited to outside of the car, i.e., the feature of autonomously and safely moving from the starting point to the destination by detecting possible obstacles [124]. Indeed, the interior of the car is equipped with a highly advanced set of sensors aimed at improving the comfort and the safety of the passengers [125], [126]. In this scenario, radars represent the ultimate technology for enabling premium performance with small space occupation and limited privacy concerns [127]. Among the main advantages, radar-based sensing exhibits compact dimensions and consequently high level of integration with the car, together with high spatial resolution, immunity to different light conditions and limited privacy concerns [4], particularly for radars working in the mm-wave range.

Modern cars are equipped with advanced driver-assistance systems (ADAS) to help the driver and the passengers in many activities related to both the safety and the infotainment sphere. The next pages give an insight into the future challenges for the next generation of in-cabin detection systems. The researchers related to the in-cabin detection topic can be divided into three different areas of interest: a) passenger presence detection, b) inattentive driver behavior identification and c) touch-free infotainment system control.

The case a) is one of the most researched in the literature. The simplest systems rely on the radar capability to detect the range differences due to the body presence. Two examples based on 60 GHz and 77 GHz industrial and automotive radars, are reported in [66], [128], respectively. Best performance can be achieved by measuring the very small displacement due to the tiny chest motion associated with the breathing or heartbeat activities. In [129], the

passenger presence detection within the car was demonstrated during the vehicle motion. This is a challenging condition because the car motion generates unwanted phase modulations due to factors such as engine vibrations, road conditions and strong wind gusts, which overlap the signal of interest. The authors proposed a denoising technique based on additional sensors, i.e., accelerometers to separate the car motion.

Monitoring circumstances belonging to case b) is crucial for transportation safety, although it can be considered less important for the autonomous driving field. In any case, there are various situations in which the driver must supervise the car and regain control of it. As shown in [13], [130] common approach consists of considering the head motion that could be associated with real driver behaviors, analyzing the related micro-Doppler effects and classifying the different subject's behaviors. The identification of inattentive driver behaviors is crucial for the driver and passenger safety. Certain head movements can indicate inattention. Different researchers have tried to identify these movements using radar systems. This method does not involve any contact or discomfort for the user and can activate emergency procedures to avoid danger, as proposed in [13]. The challenge is to properly classify the different behaviors in a very cluttered car environment and in the presence of noise generated by car vibrations or other passengers' movement.

Case c) addresses a very sensitive topic. Indeed, the car has plenty of conventional and touch-based buttons that might distract the driver while the car is moving with catastrophic effects. A radar-based, touch-free infotainment control interface might provide a valid alternative to increase the passengers' safety. In [131], this task was accomplished using radar range measurements and convolutional neural networks to recognize specific gestures.

One way to enhance detection effectiveness is to measure the micro-Doppler effect associated with different hand gestures. This approach is adopted in this study. Several

challenges should be faced, from the clutter generated by such confined environments to determining the optimal location of the radar sensor. The chance to control the car infotainment system without any contacts is an advanced feature with great potential for various applications.

As analyzed in Chapters 1.2 and 3.3, from the phase of the reconstructed complex demodulated signal, it is possible to accurately extract the displacement of the target. Furthermore, the STFT can be exploited to have a representation of the Doppler components over time, as widely discussed in the final section of Chapter 1.2. These two radar features enable gesture recognition and, consequently, contactless control of the infotainment system. For this study, the Infineon radar system operating at 24 GHz, which was presented in Chapter 2.1, was used in the homemade version.

The radar capability to detect the passenger presence was tested inside a car. The radar system was placed on the inner roof of the car pointing towards the rear seats where a person was sitting. The key element to recognize the human presence is detecting vital signs. The breathing rate can be determined by observing the alternating positive and negative strips in the micro-Doppler signature, as shown in Fig. 3.26.

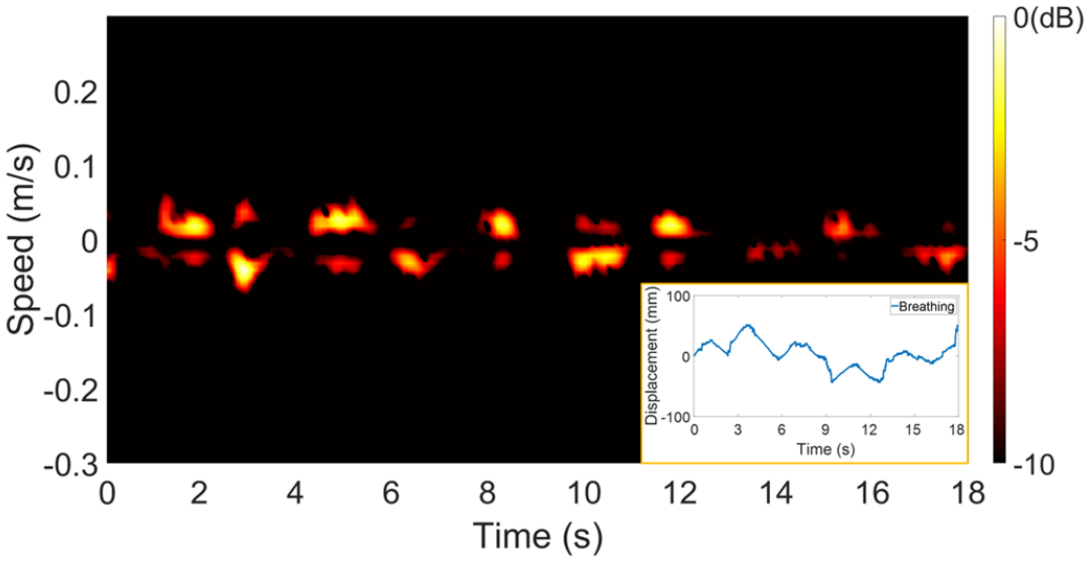

Fig. 3.26: Micro-Doppler signature and related chest displacement of a passenger on the rear seat.

Combining this output with the associated phase history shown in the inset of Fig. 3.26 can make the detection more robust. In this figure, physiological activity is evident.

Next, the radar system was pointed toward the front seat where the driver was sitting. Inattentive driver behaviors can be detected by noticing unexpected movements of the driver's body. For this reason, great attention is devoted to monitoring the driver's head. If the driver's head moves forward and backward, it could mean that the attention is decreasing because he is falling asleep. If the monitoring system detects this, the driver must be alerted immediately.

In Fig. 3.27, the micro-Doppler signature of two consecutive movements forward-backward of the head is shown. It can be classified through a machine learning algorithm thus being properly recognized.

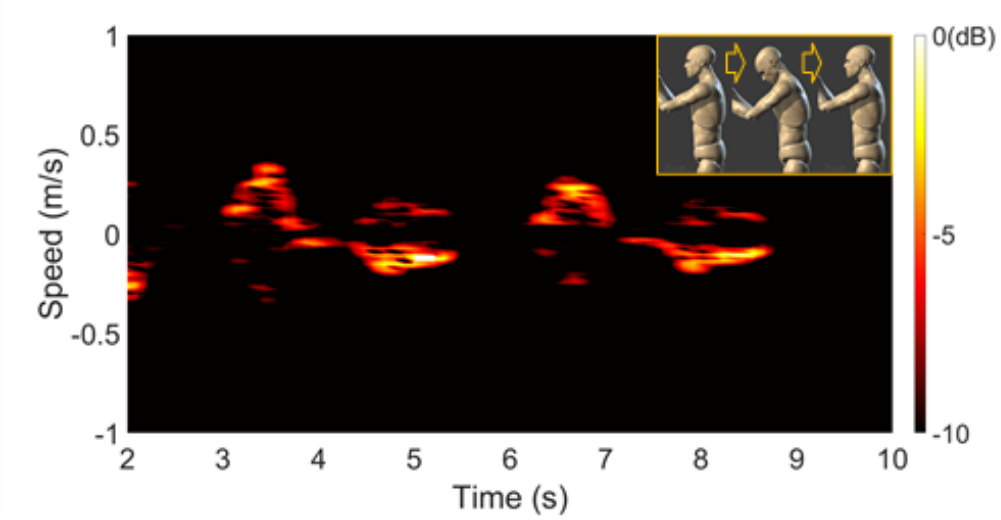

Fig. 3.27: Micro-Doppler signature of a driver falling asleep at the wheel.

The last scenario of interest concerns the touchless infotainment system control. This is probably the most futuristic topic. In the next generation of cars, passengers will be able to control the infotainment system comfortably and without touching anything. In Fig. 3.28., the micro-Doppler signatures related to an example of sound system control is shown. There are four pairs of "next-song"/"previous-song" commands associated with swipe-up and swipe-down hand gestures, respectively. They are characterized by alternating positive and negative

strips as if the user wanted to skip to the next song and then, immediately return to the previous one. This is an example of sound system control, i.e., changing songs, which enables touch-free control of the car infotainment system.

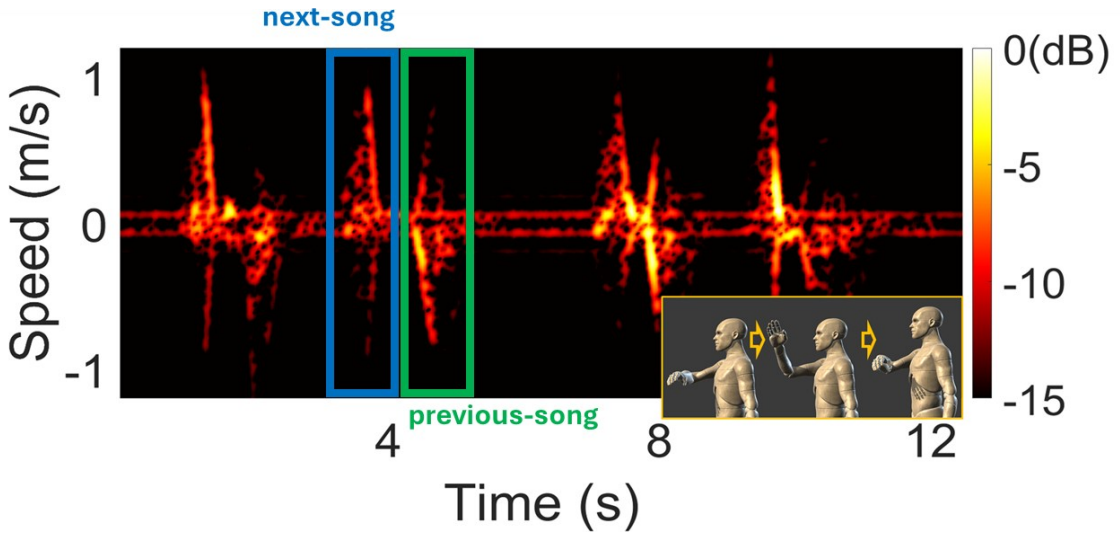

Fig. 3.28: Micro-Doppler signature concerning four couples of "next-song"/"previous-song" gestures.

It is worth noting the differences in the micro-Doppler signatures between the previous two examples and the last one, which are characterized by different speeds and timings.

In these micro-Doppler gesture illustrations, it is worth noting that some artifacts follow the real signature of the movement, that is the I/Q imbalance is present. Another case study was analyzed to investigate enabling touch-free control of the car audio level system control by removing the I/Q imbalance mirroring effect. In detail, the feasibility of the accurate volume adjustment was tested by extracting the micro-Doppler signature associated with finger movements, i.e., extending/reducing the distance between fingers proportionally to the desired audio level. Unfortunately, all quadrature direct-conversion receivers are affected by the signal deterioration due to the in-phase/quadrature mismatch, which generates mirrored signals and destroys the orthogonality of the demodulated data [117]. Therefore, the phase and amplitude imbalance between the two channels was estimated and corrected.

Specifically, the first step is to recognize the gesture, associated with the audio level regulation, via micro-Doppler analysis and, subsequently, to extract the desired volume level from the finger aperture via displacement estimation. For the sake of clarity, the movement is illustrated in Fig. 3.29.

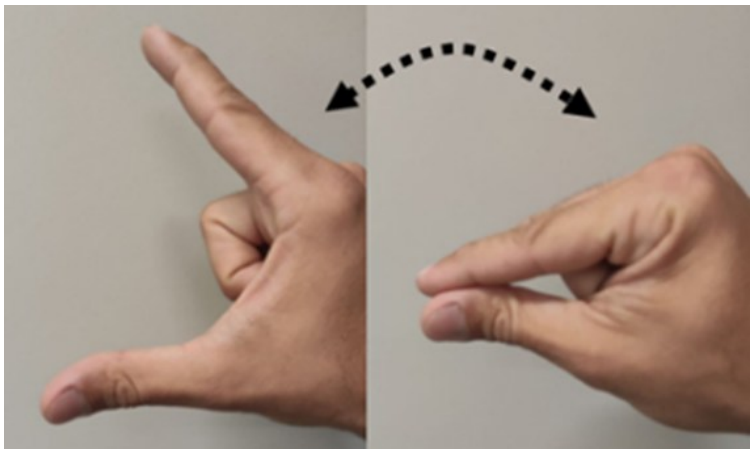

Fig. 3.29: Movement of fingers associated with the audio level.

The characteristic micro-Doppler signature of the gesture is reported in Fig. 3.30(a). In detail, the positive Doppler strips are due to the index finger approaching the radar and the distance between the two decreasing. In the same way, negative Doppler strips represent the index finger moving away from the radar.

However, mirrored signals appear near the Doppler strips of interest, thus making the detection more challenging. As anticipated, this is due to the signal orthogonality deterioration because of the I/Q mismatch.

To improve detection quality, phase and amplitude imbalance between the two channels was estimated by computing the equation of the ellipse associated with every pair of sampled data, and corrected by employing the Gram-Schmidt transformation [132], [133]. The results of the I/Q imbalance correction on the micro-Doppler are shown in Fig. 3.30(b), where the positive and negative strips are clearly visible.

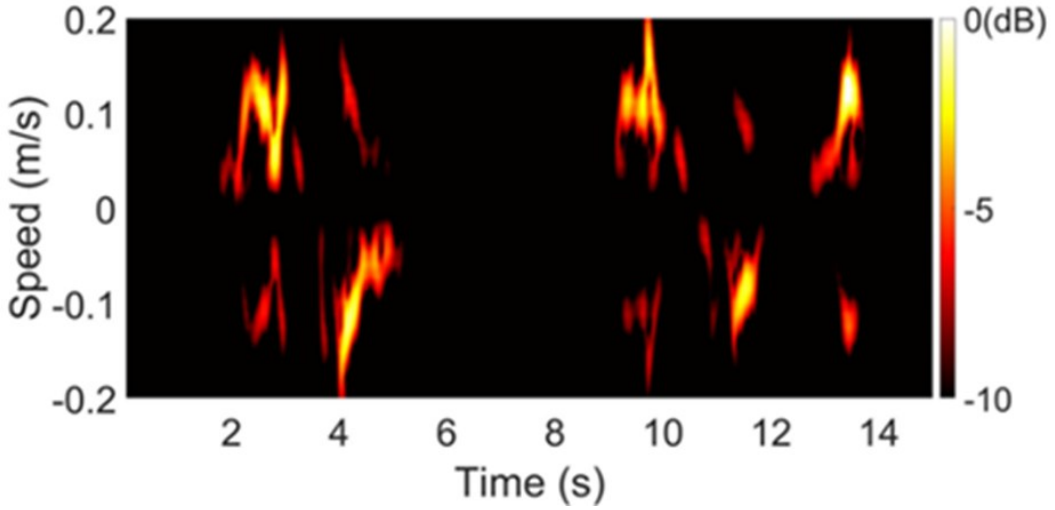

(a)

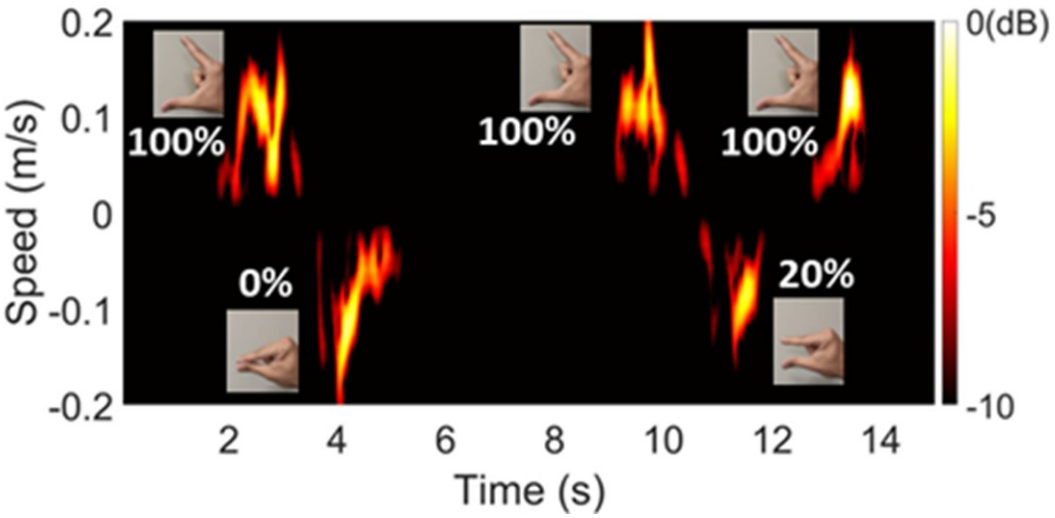

(b)

Fig. 3.30: Measured micro-Doppler signature (a) before and (b) after the I/Q imbalance correction in case of sound level adjustment.

After the first step of gesture recognition, the next goal consisted in measuring the displacement due to the finger motion by extracting the phase of the signal. Figure 3.31(a) shows the displacement related to the total aperture of the fingers, which can be associated with an increase in the audio level of up to 100%. Then, three consecutive movements were tested in order to verify the radar capability to regulate the audio level. In Fig. 3.31(b), a total aperture of the fingers, a partial contraction to 20% and finally a 100% aperture are shown.

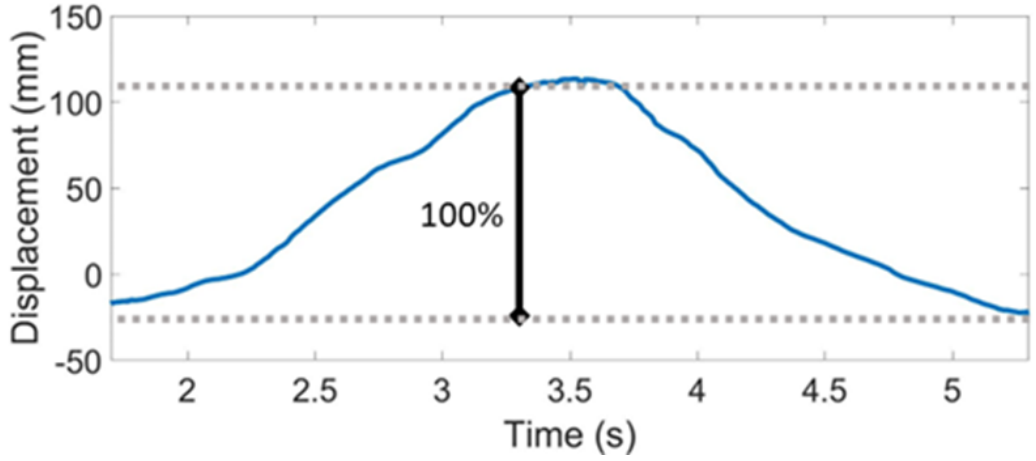

(a)

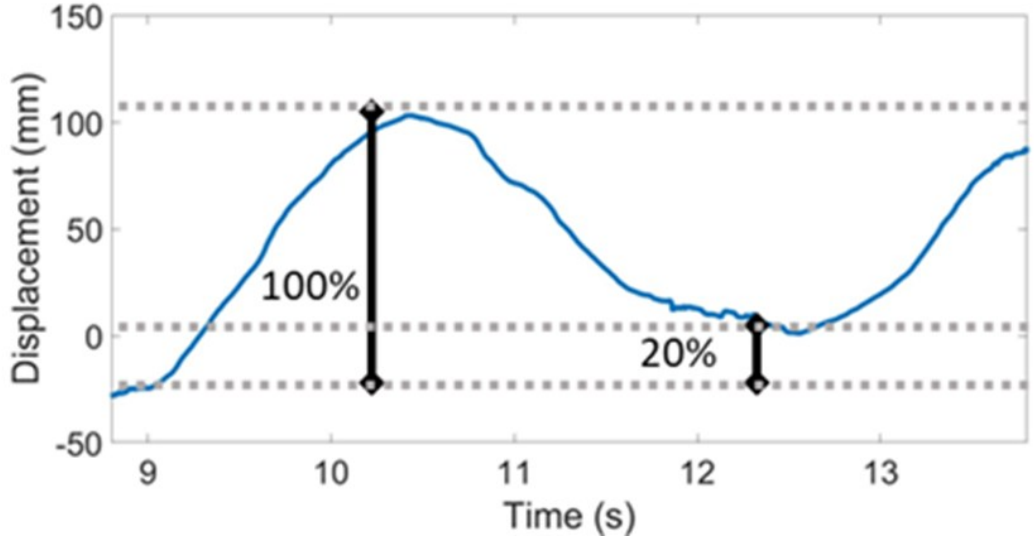

(b)

Fig. 3.31: Displacements measured related to different finger apertures: a) 0% to 100%, b) 0% to 100% to 20% to 100%.

By associating the extension of the fingers with the percentage of the audio level, it will be possible to control the audio system accordingly. However, even though the displacement measurement is correct, the precise measurement of the 100% level at the end of the measurement in Fig. 3.30(b) is not properly accomplished because of the random relative movement between the hand and the radar. An error of 12.75% was estimated for the second 100% level measurement. It is possible to assert that this movement enables accurate volume

adjustment by recognizing the gesture depicted in Fig. 3.29. Thus, measuring different hand apertures allows for volume control. Nevertheless, avoiding the effects of random body motion is one of the main challenges to be faced to enable the next generation of advanced autonomous car management where the driver and passengers will comfortably control different infotainment systems.

The second and final case study, about gesture recognition, focuses on and demonstrates the potential of highly integrated mm-wave radars in the framework of metaverse applications. An impressive growth of the metaverse market is expected in the coming years, which is estimated to rise to $ 800 billion by 2025 [134]. Gaming, social experience, education, and healthcare are among the main technical applications [135]. This work focuses on sensing systems that enable users to interact with virtual objects and environments. Metaverse glasses are designed to provide a collaborative virtual space in which the real and digital worlds converge. Accurate tracking of hand gestures is fundamental to enabling natural interactions with the virtual environment, providing a seamless experience. This is typically achieved using high-quality cameras.

However, cameras have well-known limitations related to the capability of detecting the radial range of the objects and a strong dependence on the light conditions [82]. To overcome these limitations, the 122 GHz radar by Indie Semiconductor and introduced in Chapter 2.3, was mounted on the glass frame to detect hand gestures, as shown in Fig. 3.32. For the reasons discussed in Chapter 1, exploiting radars that operate at very high frequencies ensures their effective integration with the glasses. As an example, in [3], a 24 GHz radar was used to detect eye blinking and head movement. However, it would be difficult to integrate it into the glass frames without affecting the user's comfort because its operating frequency is relatively low.

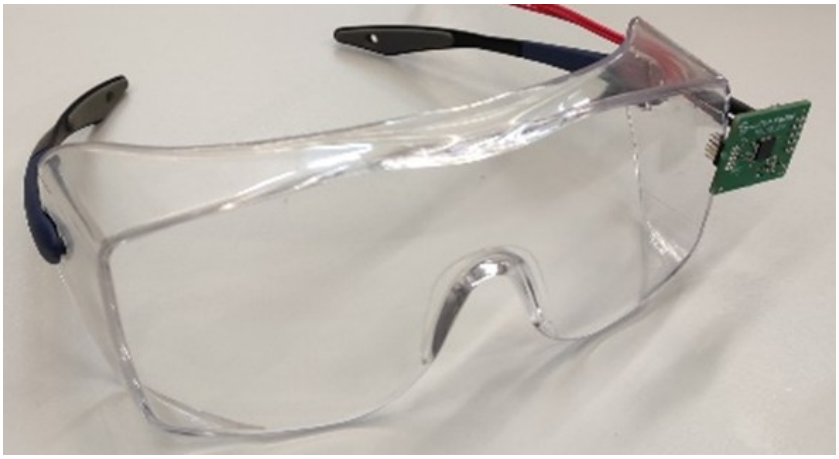

Fig. 3.32: Picture of the demo glasses equipped with the mm-wave radar.

The radar was strategically placed on the left side of the glasses in order to better focus the antenna radiation beam on the left arm. However, different positioning and the simultaneous detection of both hands might be possible by exploiting MIMO radars.

Once again, the combination of extracted displacement and STFT is necessary to recognize the characteristic micro-Doppler signatures resulting from different gestures.

In detail, Fig. 3.33(a) highlights the displacement of about 12 cm resulting from the halt command depicted in the inset figure on the right side, whereas Fig. 3.33(b) shows the relative micro-Doppler signature for this command.

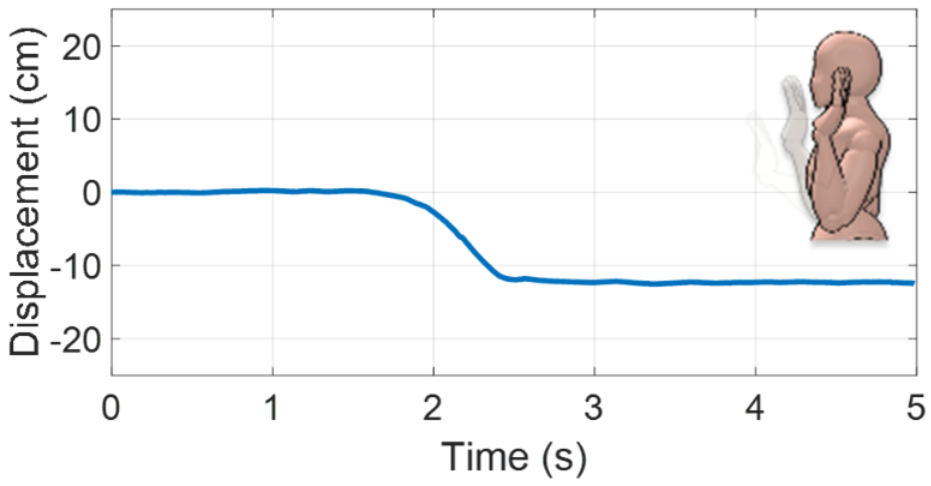

(a)

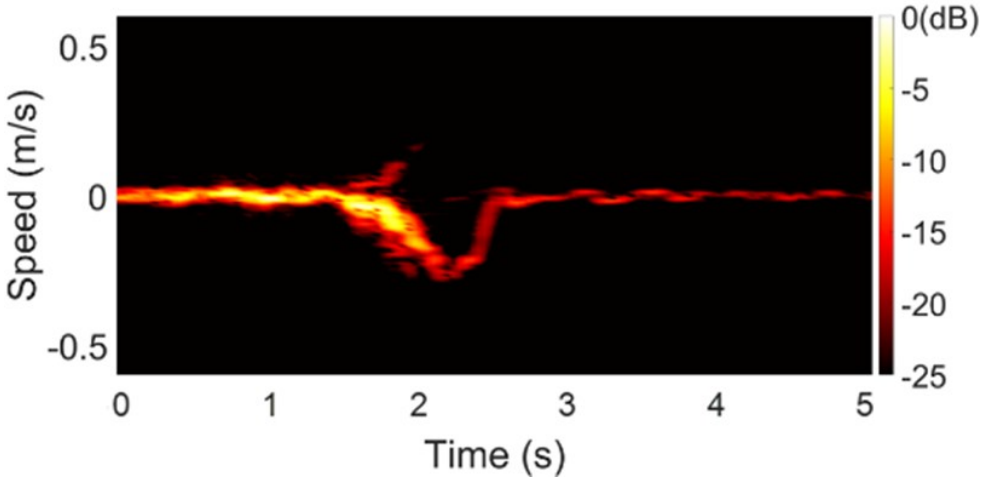

(b)

Fig. 3.33: Halt command: (a) displacement and (b) micro-Doppler signature.

The main speed contribution is due to the arm stretching, resulting in moving away from the radar and thus in a negative strip. The first section of the arm stretching is characterized by acceleration because of the speed increase. Instead, a slowing down and movement in the opposite direction distinguish the last part of the movement. On the other hand, the invite-to-move closer gesture is shown in Fig. 3.34(a). It resembles an oscillating motion due to the continuous movement of the hand fingers. Consequently, the relative micro-Doppler signature presents an alternation of negative and positive speed components as highlighted in Fig. 3.34(b).

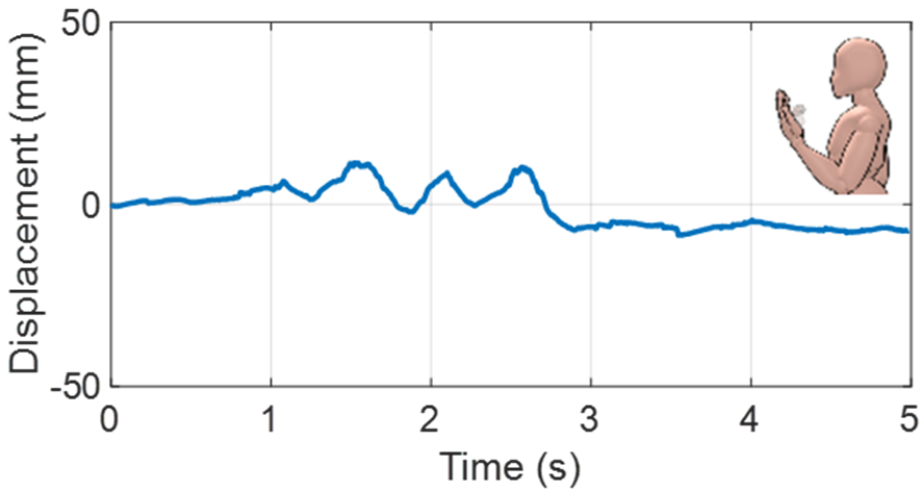

(a)

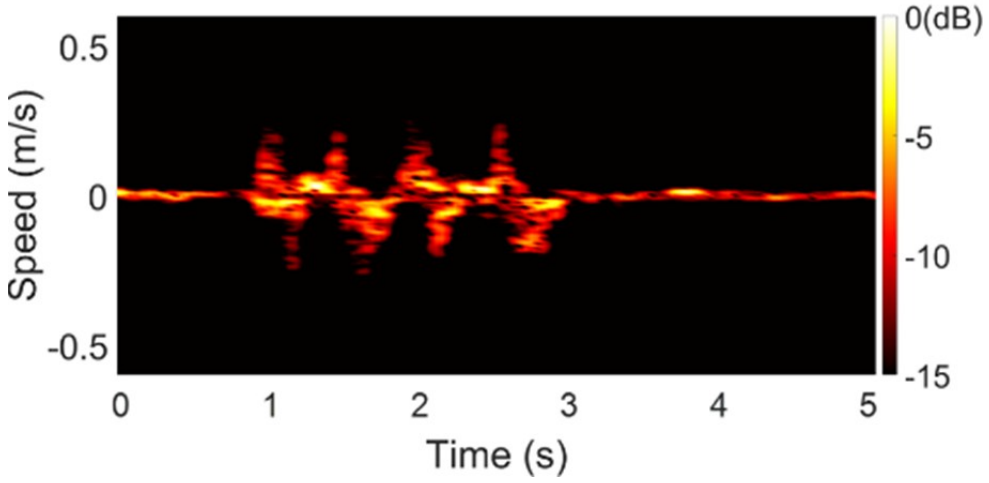

(b)

Fig. 3.34: Invite-to-move closer gesture: (a) displacement and (b) micro-Doppler signature.

Thanks to I/Q imbalance compensation, both two gestures have been properly recognized, thus demonstrating the effectiveness of the proposed solution and its potential to support the camera-based systems for metaverse applications. The next step could be the performance analysis in the presence of a moving subject, as well as the recognition of more gestures with both hands.

To conclude the paragraph, two different radar systems were used to calculate the micro-Doppler signature and phase variation in order to recognize the different movements of a human target. Particular attention was paid to describing the current status of the technology and challenges involved. This work paves the way for the next generation of interactive systems in the metaverse environment and car equipment whereby radar technology can be exploited alongside traditional sensors to provide users with advanced, complete, and reliable interactions.

3.5 Breathing activity detection in real-time

Generally, state-of-the-art papers describe radar raw data processing that occurs offline, i.e., after the measurement. Even though this is reasonable for research purposes and facilitates processing constraints, real-life applications require real-time motion pattern measurements with particular precautions, e.g., in the case of breathing activity monitoring as sketched in Fig. 3.35.

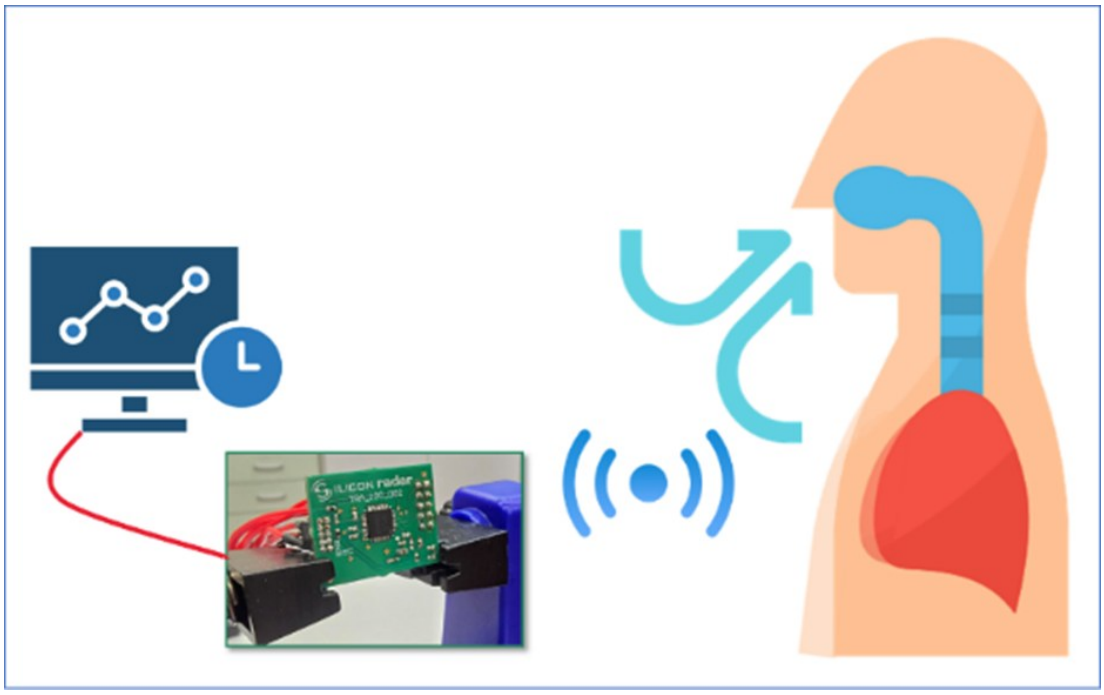

Fig. 3.35: Real-time chest displacement estimation during inhale/exhale activity.

Specifically, the task of this paragraph is to estimate chest displacement during normal respiratory activity as accurately as possible. This was accomplished by applying the algorithm presented in the final section of Chapter 3.3. Concurrently, this type of measurement also corroborates the proposed algorithm, enabling a refined displacement reconstruction during real-time estimation.

Considering the operating frequency of 122 GHz as in the simulated scenario of Chapter 3.3, the TRA_120_002 transceiver [42] was used in CW operation mode. It was combined with a

two-stage differential AC-coupled baseband and DE10-Lite FPGA board, as seen in Chapter 2.3. This aspect underscores the importance of preventing this error in view of the universal trend to exploit higher frequency spectrum in new applications, not just in the field of radar sensors. The entire system is shown in the insets of Fig. 3.36.

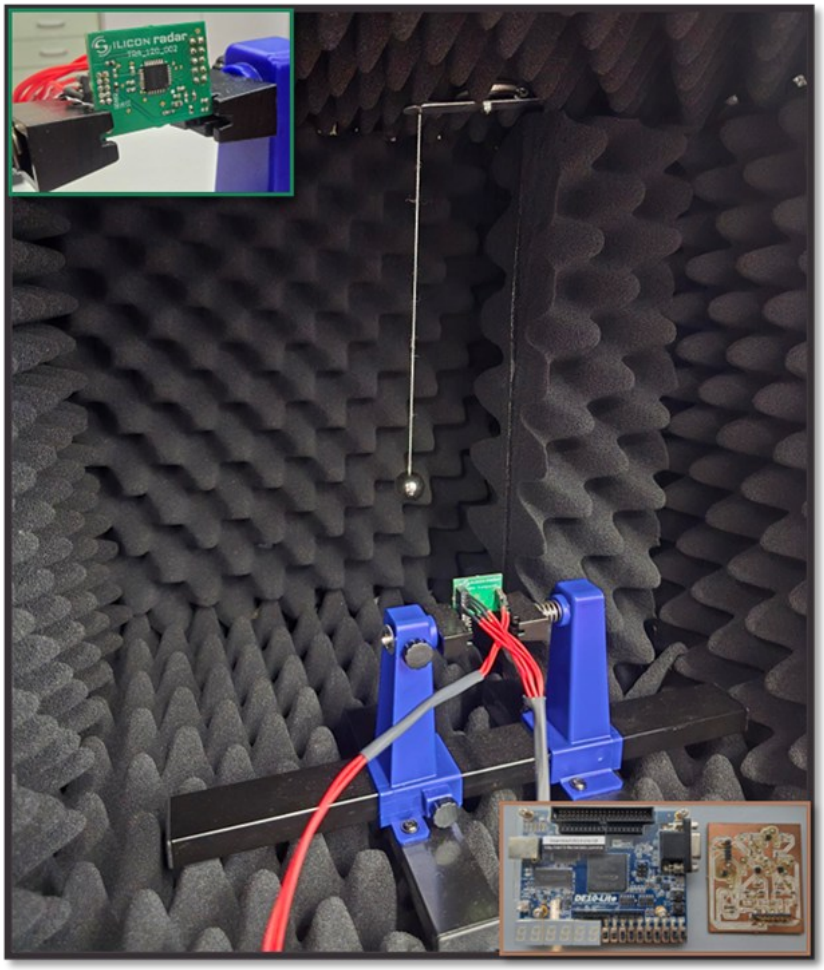

Fig. 3.36: Radar system and experiment setup.

Hence, breathing activity detection was chosen as a proper real-scenario test bench to evaluate the effectiveness of the algorithm proposed in Chapter 3.3. In the state-of-the-art, most articles focus on the in-phase and quadrature signals representation, neglecting the precise tracking of the target movement.

Measuring the breathing activity requires a high-sensitivity radar sensor with a linear receiver. Before assessing the effectiveness of the proposed solution, the radar sensor linearity

has been evaluated. It can be tested by producing an ideal sinusoidal motion using a simple pendulum [136] and measuring its oscillation frequency. A simple pendulum consists of a ball hanging from a wire of length L, which oscillates around a fixed point with a single-frequency periodic behavior. According to [137], the pendulum behaves as a linear harmonic oscillator when the swing angle Ω, shown in Fig. 3.37, is smaller than the threshold angle equal to 0.1 radians, i.e., 5.73°.

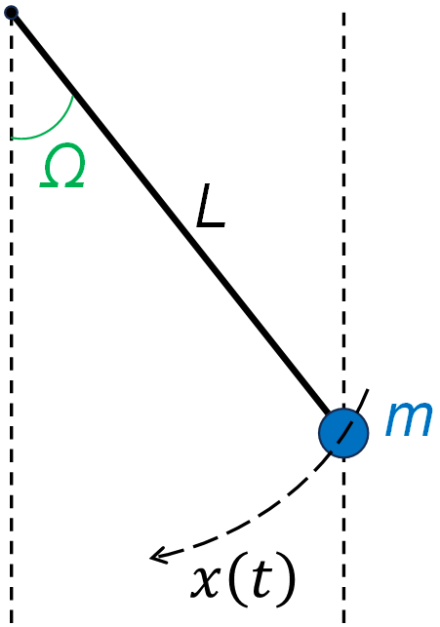

Fig. 3.37: Sketch of a simple pendulum.

Under this condition, the oscillation frequency does not depend on the pendulum mass but on its length L and local gravity acceleration g, as can be noted in Eq. 3.7.

$$f_{oscillation} = \frac{1}{2\pi}\sqrt{\frac{g}{L}} \tag{3.7}$$

The simple pendulum was positioned 16 cm away from the radar inside an anechoic and shielded chamber [138], as shown in Fig. 3.36. The bearing structure of the pendulum has been upholstered with anechoic material to drastically reduce the reflection from the metal structure of the pendulum itself. Since the wavelength is 2.5 mm, the far-field condition is guaranteed from

only 1.3 mm because of the extremely reduced dimensions of the dipoles on-chip. The greatest section of the dipole antenna is, in fact, just 1.25 mm. The steel ball diameter is 1.5 cm, and it is suspended by a 30 cm-long thin string. The reported length keeps track of the fulcrum position and ball size; indeed, the center of the ball is considered the endpoint of the string and the fulcrum as the starting point. The radar sensor was mounted on a holder placed inside the anechoic chamber. According to Eq. 3.7 and considering g equal to 9.81 m/s^2 at sea level, the simple pendulum frequency oscillation is calculated as 0.91 Hz.

The radar linearity test was performed offline, thus in a controlled environment. Detailly, Fig. 3.38(a) shows a segment of around 30 s of pendulum swinging. The pendulum amplitude is approximately 18 mm, and the initial angular position of the pendulum corresponds to 3.44°, thus smaller than the 5.73° threshold. In view of the initial angular position threshold, the simple pendulum swing can be considered a pure harmonic motion as confirmed in Fig. 3.38(b). The estimated pendulum oscillation frequency is 0.89 Hz, which matches the calculated one and confirms the high linearity of the system. The error between the detected and calculated value stems from some approximations and amounts to 2.2%. Indeed, the Eq. 3.7 was derived considering a mass-point equivalence rather than the 1.5 cm ball diameter, an approximated string length and the absence of air friction.

The pure shape of the signal suggests the lack of harmonics. Indeed, Fig. 3.38(b) displays the spectrum of the corresponding pendulum swing measurement, confirming a single pure frequency component without the presence of any harmonics. The absence of harmonics in the spectrum demonstrates the high radar sensor linearity.

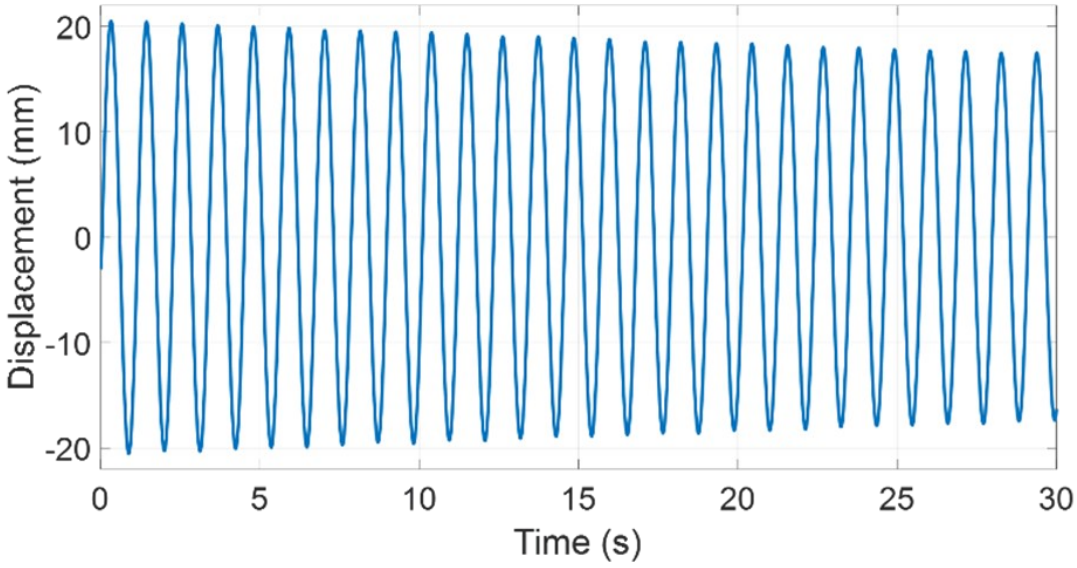

(a)

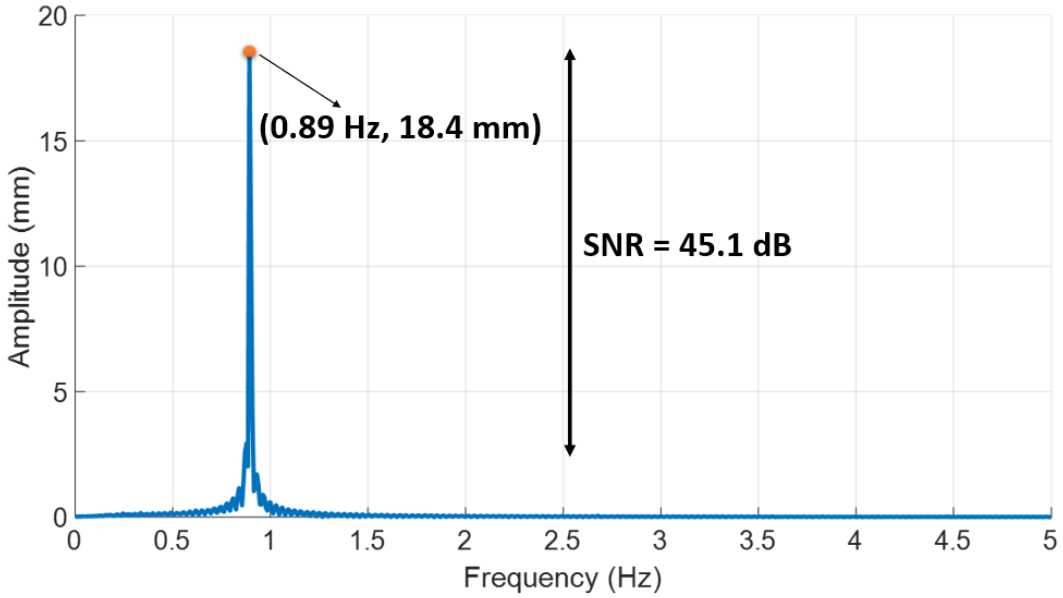

(b)

Fig. 3.38: Displacement (a) and frequency spectra (b) to evaluate the linearity of the system.

Next, to test the sensor sensitivity, the string was shortened to 6.5 cm in order to intentionally increase the pendulum frequency to around 2 Hz. In this manner the oscillation decays rapidly and the sensitivity is evaluable quickly because the swing amplitude decreases rapidly. The reconstructed displacement and its corresponding spectrum in Fig. 3.39 confirm the high radar sensitivity.

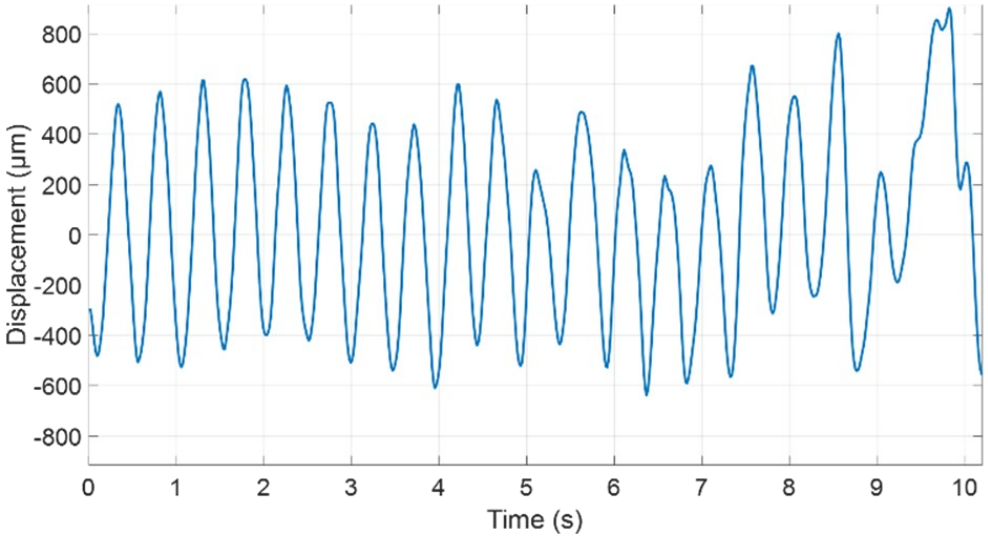

(a)

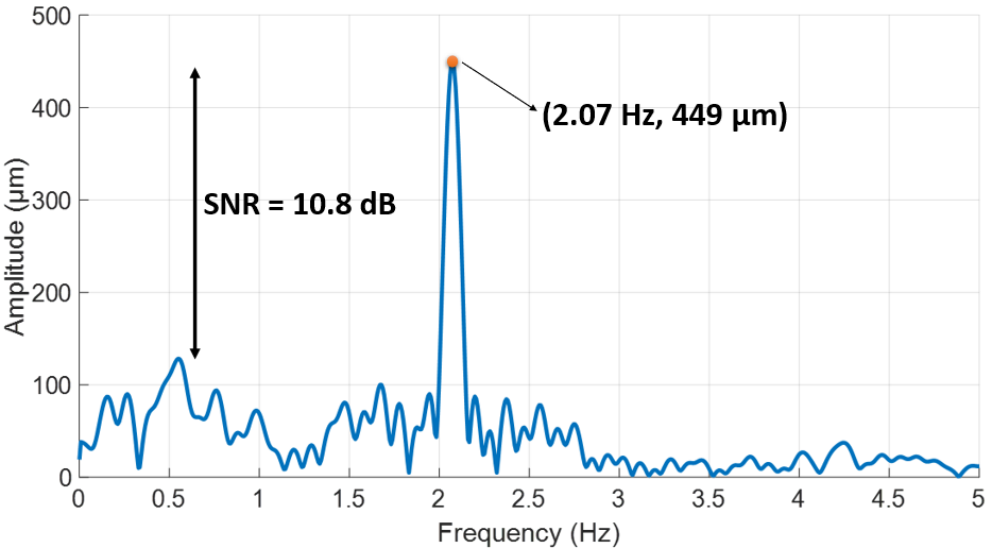

(b)

Fig. 3.39: Displacement (a) and frequency spectra (b) to evaluate the sensitivity of the system.

A 10 dB SNR threshold was chosen as the minimum value making reliable displacement estimation. The swing amplitude is easily distinguishable from the noise floor up to 450 µm where the calculated SNR is equal to 10.8 dB, slightly above the selected threshold. As a result, the linearity and sensitivity tests, enhanced by the use of the anechoic chamber, acted as a ground truth and validated the goodness of this radar system. Hence, considering the pendulum oscillation as ground truth, this radar sensor can be deemed a reliable and accurate system. This

aspect is confirmed by the results illustrated in Fig. 3.38 and 3.39 where the oscillation frequency and the displacement are very close to the calculated results, with a percentage error of 3.3%.

Thus, the radar used allows the expected 1 cm respiratory extent to be detected with confidence, and the measured SNR value ensures that the measurement is performed correctly. After the linearity and sensitivity tests, the radar system was located half a meter from the user, and the measurement was carried out when the user breathed normally. This is just an example to underline the impact of this algorithm in the real-world scenario. It is worth noting that the preliminary characterization with the pendulum in a controlled scenario was performed to quantitatively assess the expected performance. The theoretical foundation of the proposed method is independent of the real scenario, which can be affected by countless parameters and different conditions. However, breathing activity displacement reconstruction is an up-to-date topic in the field of radar contactless sensing of physiological parameters.

The measurement was performed outside the anechoic chamber. The user breathed normally while sitting at a classic workstation. Thus, the respiratory activity was monitored during the daily work. The optimized algorithm for real-time measurements has been applied and the result is shown in Fig. 3.40, in which measurement and frame last 20 s and 1 s, respectively.

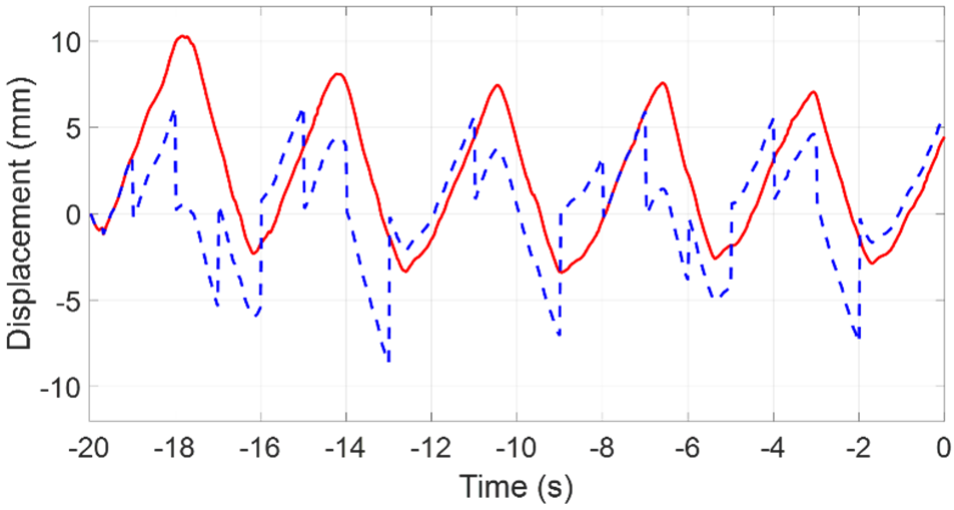

Fig. 3.40: Wrong (blue dashed line) and correct (red solid line) displacement reconstruction after the application of the optimized algorithm during a real-time measurement.

Displacement dynamics of about 10 mm are typical during inhalation and exhalation for a person with healthy breathing activity, when the radar sensor is pointed toward the diaphragmatic area. The discontinuities in the blue dashed line, obtained by applying the algorithm optimized for the offline case, confirm the necessity to use a different algorithm for real-time measurements. Indeed, the new algorithm produces the red solid line that follows the diaphragmatic movement accurately. Nevertheless, the breathing pace of the blue line follows the red one as a result of the cyclic nature of correct breathing. In addition, it is interesting to observe that the offline algorithm does not produce errors for displacements around 0 mm at -1 s, -10 s and -12 s, confirming the considerations of Chapter 3.3. Indeed, the unwrapped phase is equal to zero or less than π because during these transitions, the phase difference does not exceed the π-limit. Hence, no error occurs because unwrapping is not actually required.

As can be seen in Fig. 3.40, the new algorithm is crucial for accurately detecting the breathing activity at any moment and providing a complete and correct view of the movement throughout the entire measurement. The slight drift of the entire movement originates only from the user's natural micro-movements during the measurement. Therefore, this analysis offers a simple solution applicable to any real scenario, as confirmed by the theoretical investigation and measurements in both controlled and realistic scenarios. Therefore, the displacement estimation is now possible in real-life and real-time applications with elevated accuracy and precision.

In a nutshell, a state-of-the-art study revealed a lack of scientific coverage on phase reconstruction during real-time measurements. Although the offline measurement technique is well established within the scientific community, the elaboration steps of the target displacement are not clearly explained during real-time measurements. The proposed algorithm refines displacement reconstruction tailored for real-time estimation by avoiding manipulation of the phase difference between consecutive samples. Hence, the new elaboration steps do not

alter the raw data and phase information, thus ensuring absolute robustness of the algorithm. Thus, the new accurate estimation of chest displacement paves the way for future commercial applications of radar sensors, whereby the peculiarity of real-time sensing needs to be properly addressed.

3.6 Eye-blinking detection

The last paragraph debates one of the most significant achievements of the entire research activity. In fact, the intention to detect eye blinking arose during the PhD program [3], [4]. The idea was to take advantage of the enhanced phase detection and customized micro-Doppler analysis via STFT application to accomplish this task.

This aim was motivated by the fact that one of the most felt and serious problems in our society involves the lack of facilitated communication for people affected by neurodegenerative pathologies. Inability to communicate, as a consequence of patient paralysis, is one of the main detrimental effects of these diseases. Since the head is the last affected part of the body, an accepted solution is to interpret intentional eye blinking as messages or commands. This work demonstrates the effectiveness of radar-based solutions as assistive systems for enabling patients to express their basic needs [3]. A mm-wave Doppler radar is devoted to this purpose with advantages in terms of size, computational cost, privacy concerns, and immunity to different light conditions, compared with competing optical image-based technologies. After analyzing the performance dependence on different radar positions, the radar was integrated into a glass frame. This mitigates the effects of random body motion resulting from the movements due to both physiological activity and external factors. Therefore, the purpose of this final paragraph is to demonstrate the effectiveness of radar as an assistive system that

enables patient communication [4]. The World Health Organization (WHO) estimates that the number of people affected by neurodegenerative disorders has grown rapidly in recent decades, probably due to the increase in life expectancy. The number of people affected by dementia was approximately 55 million in 2019. Dementia is the primary symptom of neurodegenerative pathologies and can manifest memory loss and difficulties with thinking, problem-solving, or language. Furthermore, the number is expected to increase to 139 million by 2050, according to the last WHO report [139].

Serious physical, psychological, social and economic consequences arise, not only for the subject affected by the pathology but also for relatives, friends, and caregivers [140], [141]. Since the body undergoes neuron death and progressive paralysis, the subject loses the ability to speak. This disability goes beyond the limitation of social activities because the capability to communicate basic needs, such as the sense of thirst or hunger, is also impaired compromising health status and life quality. This scenario has not left the scientific community indifferent, which has put a great effort to find new technological solutions that enable subjects to communicate in an alternative way [142]. Even though a limited number of aids are already available, a great scientific effort is still required to provide an effective solution.

Known solutions rely on the detection of brain signals by means of electrooculography (EOG) and electroencephalography (EEG) [143], [144]. They are often aimed at tracking eye movements to select a predefined message. Indeed, many systems are equipped with a display that slowly browses images depicting basic needs or simple words. Once the desired image appears on the display, the subject can select it with an intentional movement, like an eye blinking. Intentional movements must be distinguished from unintentional ones; thus, they are typically coded. For example, an intentional command can be represented by two or three consecutive eye blinking, which can be easily discerned from one. Systems based on EOG or

EEG recognize the ocular movement by directly analyzing the brain signals. However, they require contact electrodes to be placed on the subject's head. This issue is common with all contact-based sensors affecting user comfort.

Another commonly used technology for assisting people affected by neurodegenerative pathologies relies on optical sensors, i.e., cameras. Once again, intentional eye blinking can be used to communicate a specific command. However, also the task of analyzing images with cameras is not exempt from errors. The low immunity of cameras to various light conditions seriously affects system performance and increases the probability of error [12], [82], [145], [146]. Moreover, cameras raise privacy concerns making this technology barely appealing for private environments.

In this scenario, there is a massive growth of radar systems employed for biomedical applications [147], [148], [149], [150], [151]. Once again, this trend is driven by many advantages over optical sensors, such as the ability to accurately measure radial sub-millimeter motions and define micro-Doppler signatures for gestures, the preservation of user privacy and the robust operation in any lighting conditions [152]. Nevertheless, a limited number of examples are available within the scientific literature, whereby radars are employed to recognize eye blinking and head movements [147], [148], [149], [150], [151], [152], [153], [154]. A context of interest for such a kind of detections concerns the automotive industry, where head motion and eye blinking can identify inattentive driving behaviors [153], [154].

This paragraph represents the first contribution that provides a complete analysis of the problem. It not only analyzes ideal scenarios, but also investigates real circumstances that affect measurement effectiveness, such as the effects of random body motion. Indeed, physiological activity is often characterized by incorrect breathing, i.e., costal breathing, which also involves the movement of the shoulders and, consequently, of the head. This could seriously affect the

measurement. However, it should be observed that the costal and diaphragmatic muscles can be tightly coupled during voluntary breathing [161]. Some examples include breathing while singing or playing wind instruments. Furthermore, the breathing patterns depend on the frequency and the individual. To enhance the system immunity to external movements, the radar has been integrated on the glasses frame for the first time in this demonstration. This expedient mitigates the effects of random body motion as a measurement campaign will confirm in the following pages. Using electromagnetic signals allows the radar to be placed behind the lens, ensuring integration with existing glasses and facilitating distribution. Finally, using a radar that works at a very high frequency is a critical step to decreasing the total system size, which facilitates further integration with glasses.

Having already become familiar with the CW radar theory in terms of phase detection and micro-Doppler signature, the first step is to define the eyelid anatomy and the expected eye-blinking micro-Doppler signature via simulation.

The typical eyelid thickness might be considered to be 500 μm, indeed, according to [162], the thickest part of the upper eyelid is just below the eyebrow, i.e., 1127 $\pm$ 238 μm, whereas the thinnest one is near the ciliary margin, i.e., 320 $\pm$ 49 μm as highlighted in Fig. 3.41.

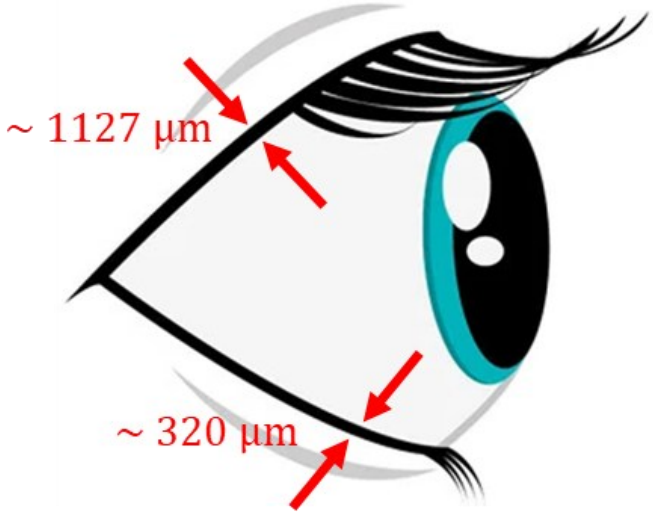

Fig. 3.41: Thickness of some parts of the eyelid.

However, the presence of the eyelashes and the different orientations of the radar in relation to the eye may result in a larger measured displacement of around 1 – 1.5 mm. It is worth noting that, in principle, the detection of the eyeball rotation could be used to enable patients to communicate. Nevertheless, no effects were observed as a consequence of the eyeball rotation during the experimental campaign. Indeed, although the eyelid thickness may be similar to the difference between the actual radius of the eye and the radius of the eye considered as a perfect sphere, the eye blinking is accentuated by the presence of the eyelashes. Furthermore, when the radar is very close to the eye, the entire eye still falls within the radar FOV due to the radiation beam aperture. This makes the radar insensitive to eyeball movement, i.e., there is no range migration for the eyeball. Moreover, due to the wide dimension of the iris compared to the entire sclera, a very evident and unnatural movement of the eyeball would be required to create a noticeable difference in terms of range.

To test the feasibility of the solution and provide a preliminary scenario description, a possible case study has been simulated by analytically reproducing the down-converted signals. In detail, a possible eyelid movement has been simulated and is shown in Fig. 3.42(a). The simulation considers the presence of eyelashes resulting in a typical maximum displacement of 1.48 mm. The eyelid closes and subsequently opens within a time frame of 200 ms.

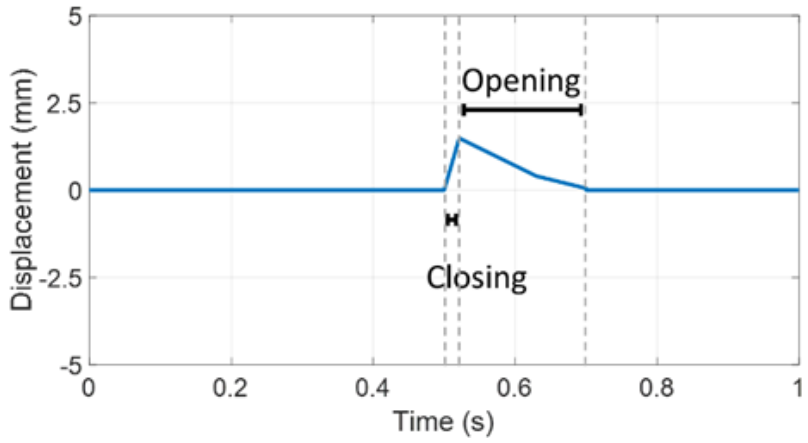

(a)

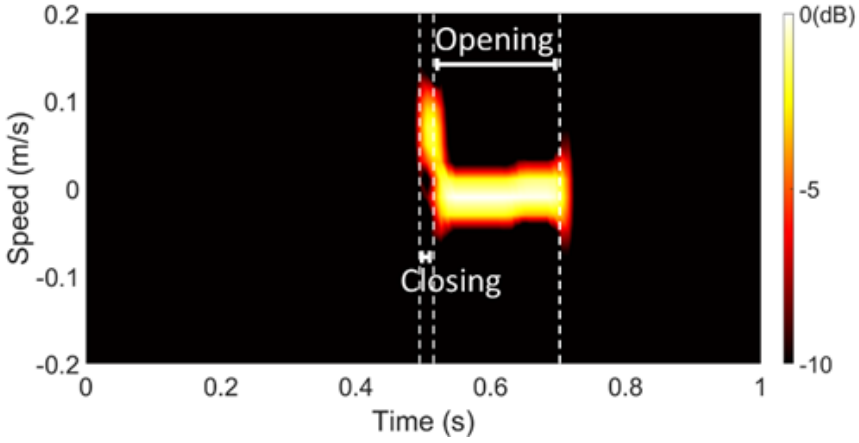

(b)

Fig. 3.42: Simulated displacement (a) and micro-Doppler signature (b) due to the eye blinking.

The STFT, applied to the down-converted signals, is fundamental to recognizing the characteristic micro-Doppler signature due to the eyelid blinking, as shown in Fig. 3.42(b), where the speed variation is plotted over time. The signature of a single blink is characterized by two distinctive moments:

- The eyelid closing reduces the distance between the radar and the eye, generating a tiny strip of positive velocity (the eyelid is drawing near the radar).
- The eyelid opening increases the distance between the radar and the eye, producing a subsequent stocky section of negative velocity (the eyelid is moving away from the radar).

Thus, it is possible to detect not only eye blinking, but also to discriminate between the two phases of the motion. As physiologically expected for a defense mechanism, the closing phase is faster than the opening one. It is worth noting that both measurements make it possible to recognize when eye blinking occurs. However, the simulated case is a simplified scenario. Indeed, although the target is mostly a paralyzed subject, the effect of random body motion cannot be neglected. An additional target movement can easily overcome the tiny eye-blinking extent, thus making the detection very challenging.

One of the main aspects to be considered concerns the head motions resulting from the subject's physiological activity [3]. To this purpose, the respiratory activity of a subject can be divided into two categories: diaphragmatic and costal breathing. Diaphragmatic breathing is the normal respiratory act of a healthy subject. Because of the diaphragm contraction and relaxation, the air is passively expelled from the lungs and the upper side of the body is not subject to any related movement. Since the body motion is confined to the chest area, the head can also be considered a stationary target.

On the other hand, a healthy individual may also exhibit costal breathing. In this case, relaxation of intercostal muscles causes the air to leave the lungs resulting in movement of the head. As investigated in [3], costal breathing seriously impacts the measurement. In many cases, eye-blinking detection by means of the displacement analysis becomes impossible. This can be inferred from Fig. 3.43(a), where the extent of breathing activity is much greater than the eyelid one, which prevents the detection of eye blinking because they cannot be recognized. For these measurements, the radar was placed on a holder 3 cm from the healthy subject's face, in order to reproduce the same distance for the cases described in the following pages.

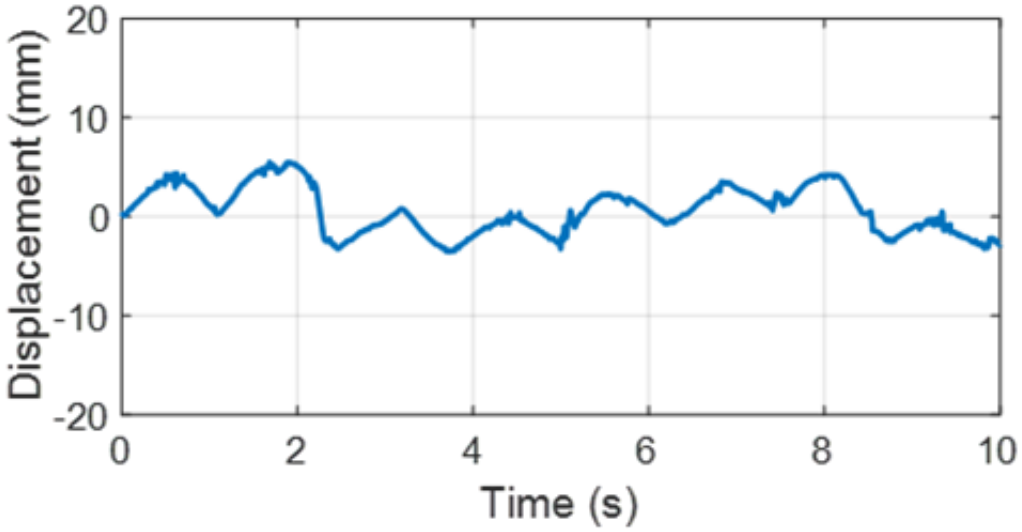

(a)

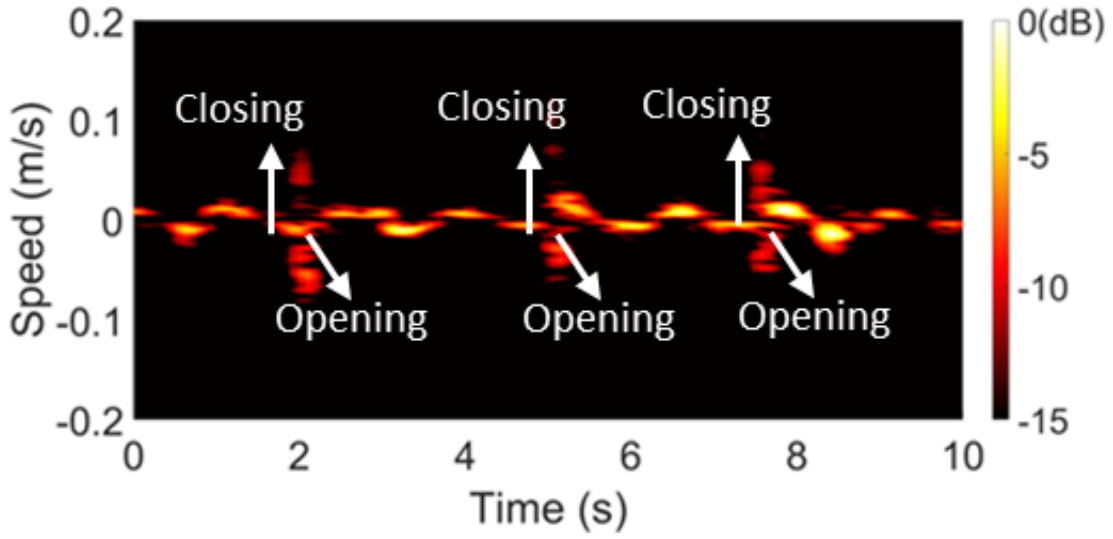

(b)

Fig. 3.43: Displacement (a) and micro-Doppler signature (b) due to the eye blinking during costal breathing. Whereas from (a) it is not possible to notice the eye blinking, it is clearly highlighted in (b).

The subject blinked normally, neither over- nor under-stress the movement. On the other hand, it is interesting to observe that, despite the thin eyelid, the eye movement is characterized by Doppler strips that are longer than those related to the costal breathing activity. Thus, the eye blinking is separable from the breathing activity by means of the micro-Doppler analysis. This demonstrates that the micro-Doppler signature can be considered a reliable tool to detect tiny movements, even in the presence of disturbing motions.

This issue is particularly relevant for people affected by neck and upper limb musculoskeletal disorders. They can lose the natural supporting function of the neck, making the effect of breathing activity on the head more evident.

However, respiratory activity is not the only detrimental body motion effect to be taken into account. People with neurodegenerative disorders exhibit an additional movement-related clinical symptom called myoclonus, which is characterized by involuntary movements caused by muscular contractions or inhibitions [163]. Since myoclonus can make the head move, it must be carefully taken into account in the present analysis to ensure reliable eye-blinking

detection. Moreover, head motion may also be a consequence of external factors. For instance, a subject might be pushed while sitting in a wheelchair. Vibrations, shakes, and changes in velocity can hugely impact the measurement. In order to mitigate the effects of the random body motion, an ad hoc tailored mm-wave radar system is introduced in Fig. 3.44.

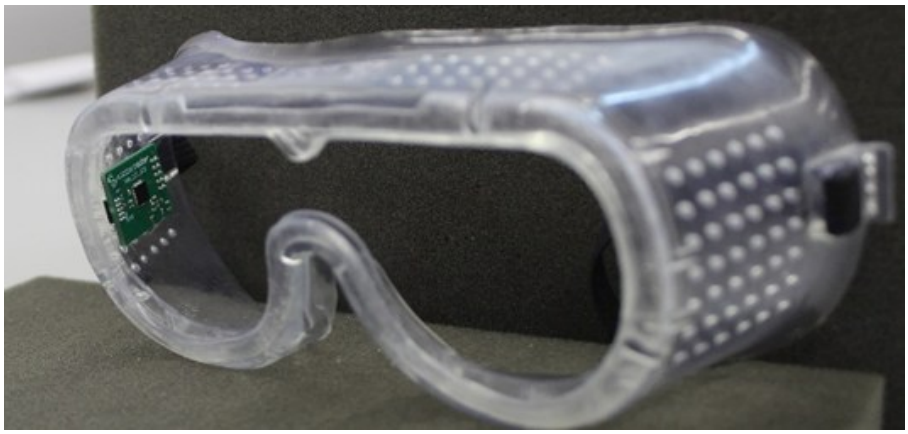

Fig. 3.44: Photograph of the glasses equipped with the mm-wave radar.

The idea is to make the radar move with the head as a whole. Hence, any movement of the head will result in the same movement of the radar, resulting in a net zero-Doppler speed between the two. Of course, the TRA_120_002 is the transceiver suitable for this task. As explained in Chapter 2.3, the entire board is very compact, with dimensions of 2.5 × 2 cm, and it is mounted on demo glasses, as can be observed in Fig. 3.44. In fact, the radar used in [3] is not adequate to be integrated into the goggles frames without significantly affecting the user's comfort.

A preliminary study was conducted in order to investigate performance dependence on radar position and to suggest a suitable location for the radar on the glass frame. In detail, the eye blinking was measured at the following radar positions on the glass front frame: center, top, bottom, right, left, and lateral. These different tested radar positions are graphically depicted in Fig. 3.45.

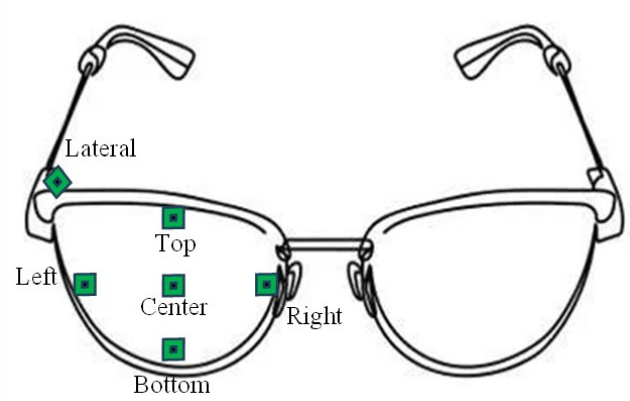

Fig. 3.45: Radar test positions.

Of course, the center position is less attractive from a practical point of view, but it is considered a good reference point. A quantitative analysis of the performance was provided by selecting the distance between the 0 m/s axis, in the micro-Doppler graph, and the maximum point of the micro-Doppler strip due to the eye blinking as a figure of merit. This choice is corroborated by the idea that the higher the micro-Doppler strip, the clearer the eye-blinking detection. Consequently, an estimate of the micro-Doppler shift is a good parameter to quantify the detection effectiveness as illustrated in Fig. 3.46(a). As shown in the inset of Fig. 3.46(a), eye closure is physiologically faster than the opening, even in the measurements. The average micro-Doppler shift values measured at various radar positions are illustrated in Fig. 3.46(b).

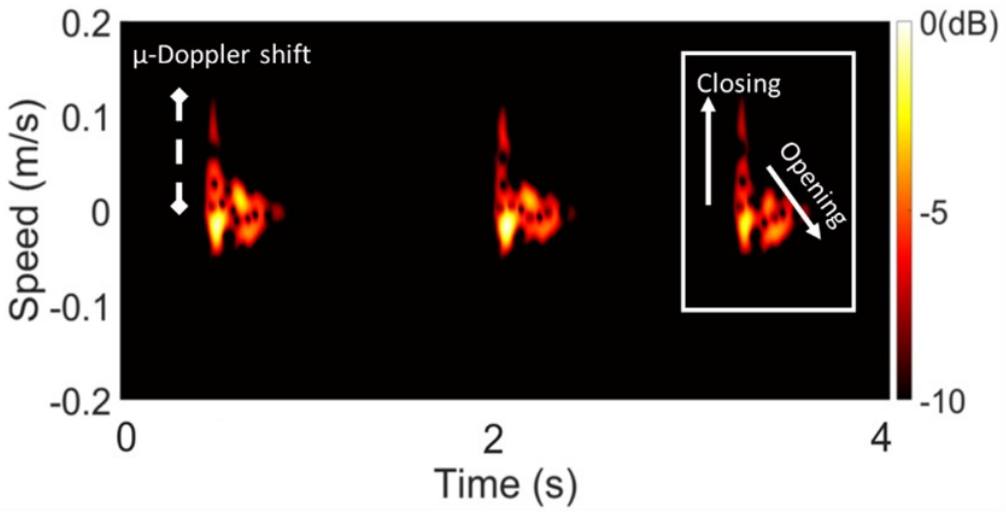

(a)

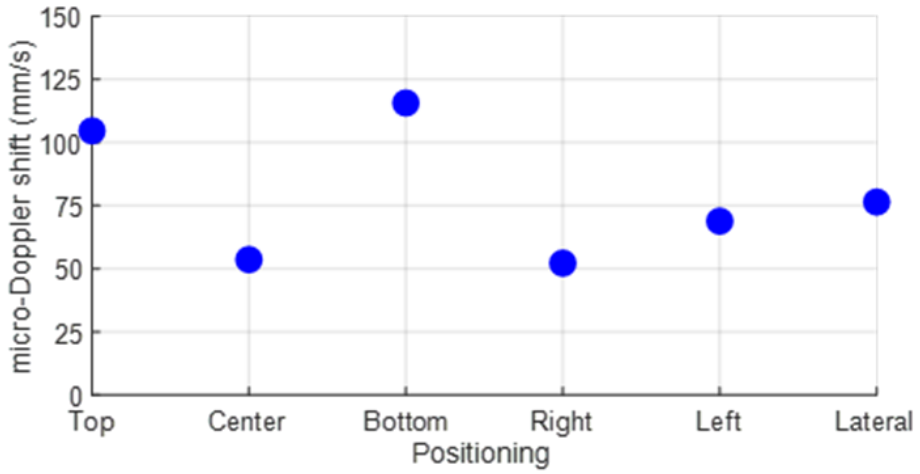

(b)

Fig. 3.46: Micro-Doppler shift evaluation (a) and average of different measured micro-Doppler shifts for different radar positions (b).

Although the measurements are repeatable, the average value was considered to avoid differences related to each single eye-blinking act and not to different positions. It is worth noting that the system performance barely depends on the radar position because the eye blinking can always be detected, with a slight improvement by using the top/bottom positions. This permits radar position selection based solely on design or mechanical considerations while maintaining the performance unchanged.

Even though the radar is very compact, the performance has also been tested when it is placed in the lateral position so that leaving the subject's field of view empty. The variance of the measured micro-Doppler shift for the lateral position is 0.04 mm/s, whereas the average value is 76.4 mm/s. Since the results highlighted that this position represents a good trade-off between measurement effectiveness and user comfort, it was maintained for the next measurements.

After defining the radar placement onto the glasses frame, some case examples are reported below. It begins with the eye-blinking detection during the costal breathing case as highlighted in Fig. 3.47.

It is important to note that the displacement representation in Fig. 3.47(b) was obtained by applying the algorithm discussed in Chapter 3.3, which resolves the uncertainty pertinent to the displacement calculations during the target stationary moment. It is worth remembering that this algorithm fits very well with very short-range applications like this one. Besides, all the micro-Doppler signatures are the product of a customized elaboration that keeps in mind all the considerations drawn throughout the entire PhD thesis.

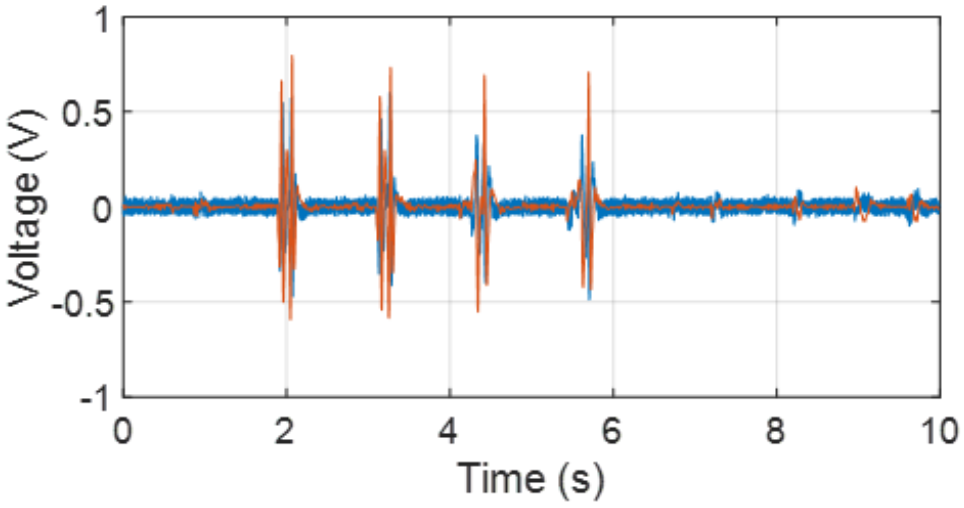

(a)

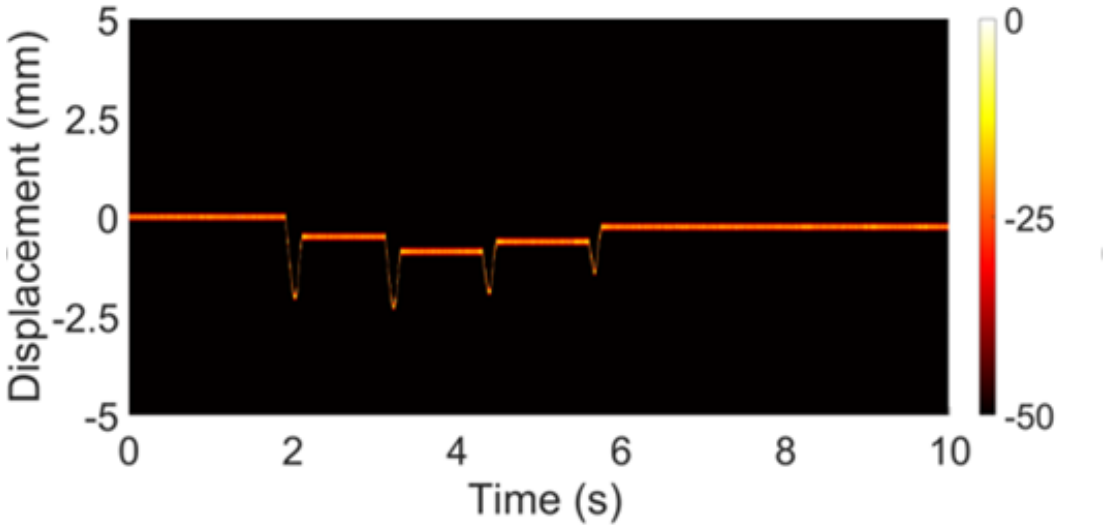

(b)

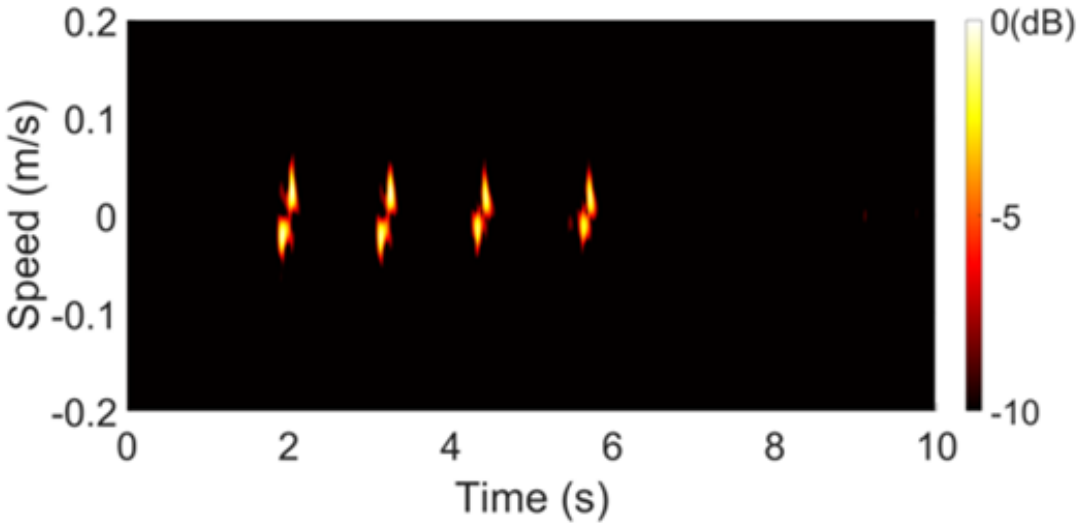

(c)

Fig. 3.47: I/Q signal (a), displacement (b) and micro-Doppler signature (c) due to the eye blinking during costal breathing. The measurement is performed with the radar placed on the glasses frame.

It is interesting to compare these results with those reported in Fig. 3.43. Indeed, both the displacement and micro-Doppler signature reveal that the detrimental effect of the random body motion has been suppressed, even maintaining the same radar-eye distance of 3 cm. The four eye blinking can be straightforwardly identified from both the displacement and the micro-Doppler signature.

The next step was to test the technique in the presence of more intense and irregular movements such as those associated with clinical symptoms, e.g., myoclonus. The subject performed random horizontal, vertical and rotating head movements, as sketched in Fig. 3.48.

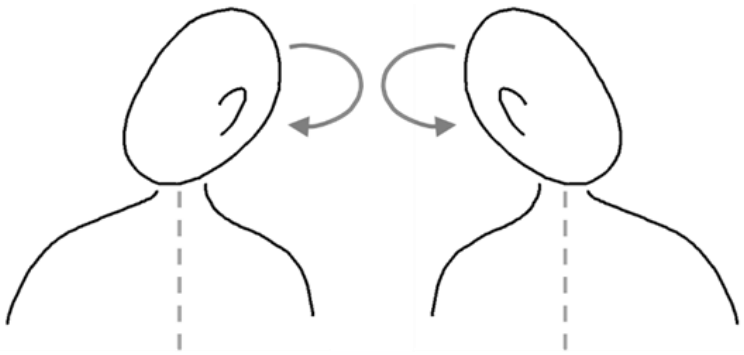

Fig. 3.48: Head movements during eye blinking.

As a matter of fact, these are intense movements, so they can be considered the worst-case scenario in this article. As shown in Fig. 3.49, eye blinking is once again detected.

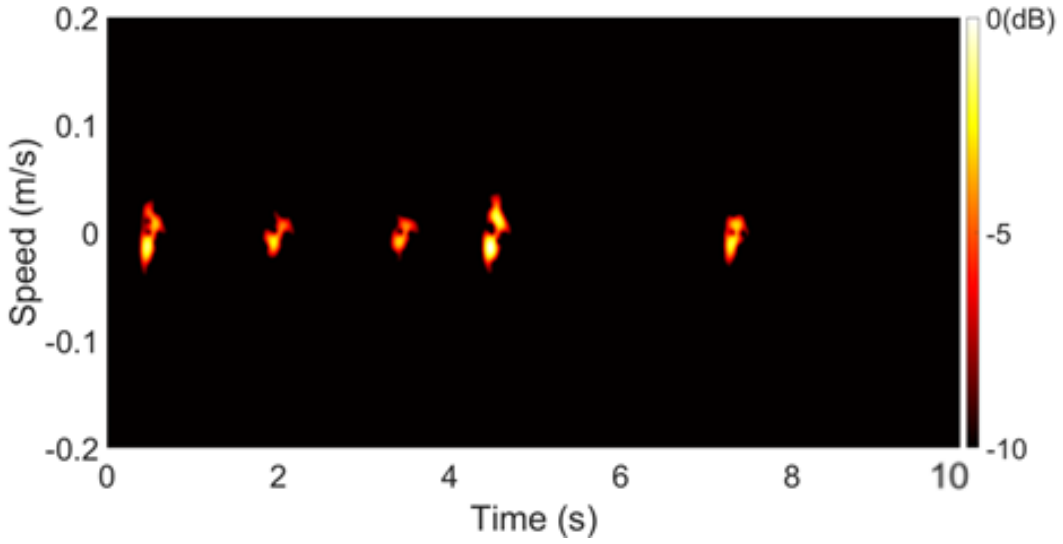

Fig. 3.49: Eye-blinking micro-Doppler signature during random head movements.

The characteristic micro-Doppler signature was exploited as a key indicator of different eye blinking. To test the reliability of the measurements, the experiment was repeated 50 times, achieving a 100% success rate in eye-blinking detection. It is worth underlining that the ability to properly classify and recognize the movement is usually attributed to detection algorithms, which were not the focus of the PhD program. However, the success rate of detection algorithm is strictly related to the SNR of the eye-blinking points compared to the others. The SNR of the results reported in Fig. 3.49 and 3.50 is 10 dB. Of course, this is not the case of a radar mounted on a fixed platform as in [3], which is greatly affected by random body motion that can lead to misclassification and misdetection of eye blinks.

As previously mentioned, the head may also move because of external factors. Therefore, the eye-blinking detection was tested with the subject seated on a moving chair in order to reproduce the motion of a wheelchair. As in the previous case, the eye blinking is properly detected and shown in Fig. 3.50.

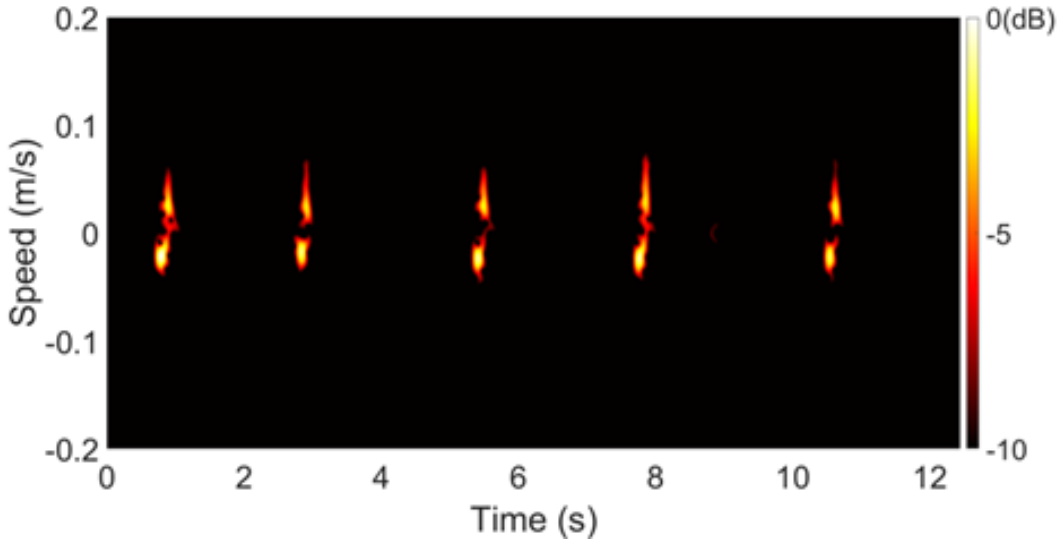

Fig. 3.50: Eye-blinking micro-Doppler signature during random wheelchair movements.

Once again, despite the movement of the entire body, the system isolates and recognizes the eyelid displacement due to the net radial motion between the radar and the eyes.

The goodness assessment of the proposed solution must be confirmed through a brief performance discussion in relation to the rest of scientific literature, in which some research groups have attempted to address the problem of detecting eye blinking using radar.

In [154], only preliminary results were reported concerning a radar system capable of detecting the eye blinking and rotation in a laboratory environment. Compared with the present contribution, only a few measurements in a static scenario have been reported, without any attempt to suppress the random body motion effect.

Also in [155], an FMCW mm-wave radar was tested to detect the eye blinking. However, it required complex postprocessing techniques and only a simple case has been studied with the subject's face and eyes kept very stable in front of the radar. On the other hand, the present work analyzes eye-blinking detection during different respiration patterns, head motions and external factors.

Yang et al. [156] propose a compact sensor based on spoof localized surface plasmons aimed at detecting eye blinking and heartbeats by pointing the sensor toward the temporal region of the subject's head, thus exploiting the motions of the skin. Once again, the tests were performed on a stationary subject, without focusing on a more realistic scenario.

In [159], a 5 GHz radar was exploited for the same purpose. However, the detected signals were affected by low-frequency noise that, in turn, made the detection challenging. The issue was addressed by applying complex processing techniques to distinguish the desired eye movement. The systems proposed in [153] and [160] were devoted to detect drowsy driving and they suffered from the in-cabin clutter. This issue was solved by applying different processing algorithms. Compared with [153], [159] and [160], the present contribution resolves the random body motion issue without applying any complex signal processing algorithms.

The preliminary analyses, reported in [3], [158], focused on detecting of eye blinking under very stable measurement conditions and by testing only the effect of respiration, respectively. Due to the higher operating frequencies, this paragraph described the radar integration on the glass frames and analyzed the system performance for various radar board positions. This configuration suppresses the effects of random body motion, making this system appropriate and reliable in real-world scenarios. Therefore, the distinctive contributions of this work rely on the thoroughness of the reported analysis despite the very low maturity level of the current technology due to the elevated frequencies but exploiting board compactness.

In addition, the proposed study addressed practical issues related to the peculiar condition of subjects affected by neurodegenerative pathologies. Furthermore, the displacement and micro-Doppler signature of the eye blinking have not required any additional processing steps that could have increased the computational cost.

An analytical comparison between the present results and those reported in the literature is not feasible because this is the first work that takes all aspects of this application into consideration. Hence, this mm-wave radar system was employed with the aim to enable nonverbal communication for subjects affected by neurogenerative pathologies. Now, intentional eye blinking can be interpreted as messages or commands for an assistive device or person via radar. This allows paralyzed subjects lying in bed to turn the lights on and off, to control the electric shutters remotely or to ask for help. Anyway, this solution is not confined only to healthcare services. In fact, the applicative field of this system can also be extended to other human-computer interaction applications in which radar-based systems compete with camera-based devices.

Conclusions

This thesis addresses current topics of interest in microwave and mm-wave radar applications. A comprehensive study of state-of-the-art and a thorough presentation of radar theory are the foundations for employing portable radars in new fields. As the applications and demands of modern radar systems grow, more advanced radars and signal processing approaches will be essential for meeting the requirements of each application field. All things considered, a primary purpose of this dissertation is to demonstrate that radar is becoming a ubiquitous tool for advanced, reliable and comfortable motion detection.

New algorithms were developed during the PhD program to ensure the correct and accurate estimation of the target displacement, from millimeters to micrometers. Customized micro-Doppler elaborations were implemented to stand out each frequency component of micro- and multi-motions of multiple targets. By studying how the radar should be positioned to mitigate the effects of random body motions, the thesis improves the recognition of the movement of a single part of the body, from the arm to the hand, from the head to the eyelid.

This work is beneficial for a variety of applications, including in-cabin automotive systems, metaverse environments and healthcare sensing. These fields are important for improving human interaction with objects and people via gesture recognition, enhancing security and enabling communication for paralyzed individuals. Therefore, all the improvements to real-time displacement reconstruction and micro-Doppler analysis are fundamental to the use of customized and refined algorithms for tasks such as gesture recognition during daily activities like driving or working.

Concurrently, design approaches were developed to pave the way for portable radars to play a new role even in navigation and space. Future developments will include implementing the

designed radar systems to test their effectiveness in the related environments, such as the short-range ship collision avoidance systems on ships. Furthermore, this thesis establishes the theoretical basis to design and realize the first MIMO radar composed of multiple already existing SISO ICs operating in the D-band spectrum. Of course, the next advancement is to complete the radar system to thoroughly monitor short-range scenarios, thereby enhancing security in industrial and automotive fields and supervising simultaneously patients' vital signs.

The transversal use of the radar system states that this topology of sensor can work and cooperate with other sensors or, in some cases, even replace them totally due to lots of advantages, e.g., contactless monitoring, compact size and light weight, the possibility to be covered by a radome to protect the radar against weather conditions, immunity to light conditions, and limited privacy concerns.

At the same time, portable radars are a relatively new technology with respect to the others and continuous research activity is indispensable to cut costs and eradicate end users' personal biases against "radiation", since portable radars do not emit ionizing radiation and their transmitted power levels are limited by the ISM regulations. Of course, the perfect sensor does not exist and the best solution depends on the sought-after features. The best result may lie in the use of multiple technologies simultaneously.

In conclusion, the radar provides a complete analysis of real-world scenarios by collecting information on multiple targets of interest contemporarily with a low computational load. Range, velocity, displacement and angular position are the basic parameters used to describe the surrounding environment. Combining all these features, the radar becomes a very powerful tool for overall and emerging applications. Since the history of radar systems for such cutting-edge applications, topologies, and frequency ranges is relatively new and short, many research topics are still open and a great effort will be required by the research community.

References

[1] G. Wang, J.-M. Munoz-Ferreras, C. Gu, C. Li, and R. Gomez-Garcia, “Application of Linear-Frequency-Modulated Continuous-Wave (LFMCW) Radars for Tracking of Vital Signs,” *IEEE Trans. Microw. Theory Tech.*, vol. 62, no. 6, pp. 1387–1399, June 2014, doi: 10.1109/TMTT.2014.2320464.

[2] G. Paterniani *et al.*, “Radar-Based Monitoring of Vital Signs: A Tutorial Overview,” *Proc. IEEE*, vol. 111, no. 3, pp. 277–317, Mar. 2023, doi: 10.1109/JPROC.2023.3244362.

[3] E. Cardillo, G. Sapienza, L. Ferro, C. Li, and A. Caddemi, “Radar Assistive System for People With Neurodegenerative Disorders Through Head Motion and Eyes Blinking Detection,” in *2023 IEEE/MTT-S International Microwave Symposium - IMS 2023*, San Diego, CA, USA: IEEE, June 2023, pp. 979–982. doi: 10.1109/IMS37964.2023.10187979.

[4] E. Cardillo, L. Ferro, G. Sapienza, and C. Li, “Reliable Eye-Blinking Detection With Millimeter-Wave Radar Glasses,” *IEEE Trans. Microw. Theory Tech.*, vol. 72, no. 1, pp. 771–779, Jan. 2024, doi: 10.1109/TMTT.2023.3329707.

[5] E. Cardillo *et al.*, “An Electromagnetic Sensor Prototype to Assist Visually Impaired and Blind People in Autonomous Walking,” *IEEE Sens. J.*, vol. 18, no. 6, pp. 2568–2576, Mar. 2018, doi: 10.1109/JSEN.2018.2795046.

[6] N. Roshandel *et al.*, “mmPrivPose3D: A RaDAR-based approach to privacy-compliant pose estimation and gesture command recognition in human-robot collaboration,” *IEEE Sens. J.*, pp. 1–1, 2025, doi: 10.1109/JSEN.2025.3578094.

[7] H. Gao, C. Williams, V. G. Rizzi Varela, and C. Li, “Violin Gesture Recognition Using FMCW Radars,” in *2023 IEEE Topical Conference on Wireless Sensors and Sensor Networks*, Las Vegas, NV, USA: IEEE, Jan. 2023, pp. 13–15. doi: 10.1109/WiSNeT56959.2023.10046213.

[8] E. Cardillo, L. Ferro, and D. V. Q. Rodrigues, “Exploiting Millimeter-Wave Radars to Enable Accurate Gesture Recognition for the Metaverse Environment,” in *Proceedings of SIE 2023*, vol. 1113, C. Ciofi and E. Limiti, Eds., in Lecture Notes in Electrical Engineering, vol. 1113, Cham: Springer Nature Switzerland, 2024, pp. 110–115. doi: 10.1007/978-3-031-48711-8_13.

[9] E. Cardillo, C. Li, and A. Caddemi, “Embedded heating, ventilation, and air-conditioning control systems: From traditional technologies toward radar advanced sensing,” *Rev. Sci. Instrum.*, vol. 92, no. 6, p. 061501, June 2021, doi: 10.1063/5.0044673.

[10] S. Lim, S. Lee, J. Jung, and S.-C. Kim, “Detection and Localization of People Inside Vehicle Using Impulse Radio Ultra-Wideband Radar Sensor,” *IEEE Sens. J.*, vol. 20, no. 7, pp. 3892–3901, Apr. 2020, doi: 10.1109/JSEN.2019.2961107.

[11] E. Cardillo, L. Ferro, and C. Li, “Microwave and Millimeter-Wave Radar Circuits for the Next Generation Contact-Less In-Cabin Detection,” in *2022 Asia-Pacific Microwave Conference (APMC)*, Yokohama, Japan: IEEE, Nov. 2022, pp. 231–233. doi: 10.23919/APMC55665.2022.9999764.

[12] E. Cardillo, L. Ferro, C. Li, and A. Caddemi, “Microwave Radars for Automotive In-Cabin Detection,” in *Proceedings of SIE 2022*, vol. 1005, G. Cocorullo, F. Crupi, and E. Limiti, Eds., in Lecture Notes in Electrical Engineering, vol. 1005, Cham: Springer Nature Switzerland, 2023, pp. 75–80. doi: 10.1007/978-3-031-26066-7_12.

[13] C. Ding *et al.*, “Inattentive Driving Behavior Detection Based on Portable FMCW Radar,” *IEEE Trans. Microw. Theory Tech.*, vol. 67, no. 10, pp. 4031–4041, Oct. 2019, doi: 10.1109/TMTT.2019.2934413.

[14] M. Caffa, S. Bottigliero, F. Ramonda, L. Gioanola, and R. Maggiora, “Integrated Design and Prototyping of a 77 GHz Automotive Medium Range Radar into Car Rear Lamp,” *IEEE Trans. Veh. Technol.*, vol. 73, no. 3, pp. 3041–3050, Mar. 2024, doi: 10.1109/TVT.2023.3324986.

[15] E. Cardillo and L. Ferro, “Multi-Frequency Analysis of Microwave and Millimeter-Wave Radars for Ship Collision Avoidance,” in *2022 Microwave Mediterranean Symposium (MMS)*, Pizzo Calabro, Italy: IEEE, May 2022, pp. 1–4. doi: 10.1109/MMS55062.2022.9825520.

[16] E. Cardillo, R. Cananzi, L. Ferro, C. Li, P. Vita, and P. Vita, “Detection of Space Debris through Compact X Band FMCW Radar,” in *2023 16th International Conference on Advanced Technologies, Systems and Services in Telecommunications (TELSIKS)*, Nis, Serbia: IEEE, Oct. 2023, pp. 126–129. doi: 10.1109/TELSIKS57806.2023.10316106.

[17] D. M. Pozar, *Microwave engineering*, 4th ed. Hoboken, NJ: Wiley, 2012.

[18] R. K. Amineh, “Applications of Electromagnetic Waves: Present and Future,” *Electronics*, vol. 9, no. 5, p. 808, May 2020, doi: 10.3390/electronics9050808.

[19] M. A. Richards, J. Scheer, W. A. Holm, and W. L. Melvin, Eds., *Principles of modern radar*. Raleigh, NC: SciTech Pub, 2010.

[20] A. Caddemi and E. Cardillo, “A study on dynamic threshold for the crosstalk reduction in frequency-modulated radars,” in *2017 Computing and Electromagnetics International*

Workshop (CEM), Barcelona, Spain: IEEE, June 2017, pp. 29–30. doi: 10.1109/cem.2017.7991871.

[21] X. Guan, L. Zhong, D. Hu, and C. Ding, "Threshold determination for dynamic programming based track-before-detect in passive bistatic radar," in *2014 12th International Conference on Signal Processing (ICSP)*, Hangzhou: IEEE, Oct. 2014, pp. 1938–1943. doi: 10.1109/icosp.2014.7015331.

[22] V. C. Chen, *The micro-Doppler effect in radar*, Second edition. in Artech House radar series. Norwood, MA: Artech House, 2019.

[23] E. Cardillo and C. Li, *Portable Microwave and mmWave Radars for Contactless Healthcare*, 1st ed. New York: River Publishers, 2024. doi: 10.1201/9781003609483.

[24] M. S. Ishrak and V. M. Lubecke, "Accuracy Considerations for CW Radar Monitoring of Respiratory Motion," in *2022 Asia-Pacific Microwave Conference (APMC)*, Yokohama, Japan: IEEE, Nov. 2022, pp. 228–230. doi: 10.23919/apmc55665.2022.9999973.

[25] B.-K. Park, O. Boric-Lubecke, and V. M. Lubecke, "Arctangent Demodulation With DC Offset Compensation in Quadrature Doppler Radar Receiver Systems," *IEEE Trans. Microw. Theory Tech.*, vol. 55, no. 5, pp. 1073–1079, May 2007, doi: 10.1109/tmtt.2007.895653.

[26] I. Djurovie, V. Popovic-Bugarin, and M. Simeunovic, "The STFT-Based Estimator of Micro-Doppler Parameters," *IEEE Trans. Aerosp. Electron. Syst.*, vol. 53, no. 3, pp. 1273–1283, June 2017, doi: 10.1109/taes.2017.2669741.

[27] Z. Peng, C. Li, and F. Uysal, Eds., *Modern radar for automotive applications*. London: The Institution of Engineering and Technology, 2022.

[28] G. R. Curry, *Radar system performance modeling*, 2nd ed. in Artech House radar library. Boston: Artech House, 2005.

[29] E. Cardillo and A. Caddemi, "A Review on Biomedical MIMO Radars for Vital Sign Detection and Human Localization," *Electronics*, vol. 9, no. 9, p. 1497, Sept. 2020, doi: 10.3390/electronics9091497.

[30] Z. D. Chen, G. Gokeda, and Y. Yu, *Introduction to direction-of-arrival estimation*. in Artech house signal processing library. Boston: Artech house, 2010.

[31] C. A. Balanis, *Antenna Theory: Analysis and Design*, 1st ed. in New York Academy of Sciences Series. Newark: John Wiley & Sons, Incorporated, 2016.

[32] C. Vasanelli, R. Batra, A. D. Serio, F. Boegelsack, and C. Waldschmidt, "Assessment of a Millimeter-Wave Antenna System for MIMO Radar Applications," *IEEE Antennas Wirel. Propag. Lett.*, vol. 16, pp. 1261–1264, 2017, doi: 10.1109/LAWP.2016.2631889.

[33] C. Vasanelli, A. Di Serio, and C. Waldschmidt, "Corrections to 'Assessment of a Millimeter-Wave Antenna System for MIMO Radar Applications,'" *IEEE Antennas Wirel. Propag. Lett.*, vol. 19, no. 4, pp. 720–720, Apr. 2020, doi: 10.1109/LAWP.2020.2972656.

[34] J. Li and P. Stoica, Eds., *MIMO radar signal processing*. Hoboken, NJ: J. Wiley & Sons, 2009. doi: 10.1002/9780470391488.

[35] "BGT24MTR11 Silicon Germanium 24 GHz Transceiver MMIC." Infineon Technologies AG, Mar. 25, 2014.

[36] "Sense2Go2 - 24GHz Radar DEMO kit with XMC4200 32-bit ARM® Cortex ™ -M4 Microcontroller." Infineon Technologies AG, Nov. 02, 2015.

[37] “INA827 Wide Supply Range, Rail-to-Rail Output Instrumentation Amplifier With a Minimum Gain of 5.” Texas Instruments Incorporated, Nov. 2017.

[38] Infineon Technologies AG, “KIT XMC45 RELAX LITE V1 Evaluation Board guide,” Jan. 2025.

[39] “IWR6843 Single-Chip 60 to 64 GHz mmWave Sensor.” Texas Instruments Incorporated, May 2020.

[40] “mmWaveICBoost and Antenna Module.” Texas Instruments Incorporated, Apr. 2020.

[41] “mmWave Demo Visualizer.” Texas Instruments Incorporated, Apr. 2020.

[42] “TRA_120_002 120-GHz Wide-Band IQ Transceiver with Antennas on Chip.” Indie Semiconductor FFO GmbH, Nov. 05, 2018.

[43] “SiRad Easy® Radar Front End (RFE) Board TRA_120_002 Product Sheet.” Indie Semiconductor FFO GmbH, Mar. 22, 2021.

[44] Indie Semiconductor FFO GmbH, “User Guide SiRad Easy® Evaluation Kit,” Dec. 2018.

[45] “UM1724 User manual STM32 Nucleo-64 boards (MB1136).” ST Microelectronics, Aug. 2020.

[46] “DE10-Lite User Manual.” Terasic, May 11, 2018.

[47] “TRA_120_045 120-GHz Wide-Band IQ Transceiver with Antennas on Chip.” Indie Semiconductor FFO GmbH, June 2023.

[48] Y. Wang and H. Deng, “Navigation and Collision Avoidance of Ships in Warning Area Based on Artificial Intelligence,” in *Frontier Computing*, vol. 747, J.-W. Chang, N. Yen,

and J. C. Hung, Eds., in Lecture Notes in Electrical Engineering, vol. 747, Singapore: Springer Singapore, 2021, pp. 1055–1062. doi: 10.1007/978-981-16-0115-6_120.

[49] T. N. Luong, S. Hwang, and N. Im, "Harbour Traffic Hazard Map for real-time assessing waterway risk using Marine Traffic Hazard Index," *Ocean Eng.*, vol. 239, p. 109884, Nov. 2021, doi: 10.1016/j.oceaneng.2021.109884.

[50] P. Vidmar, M. Perkovič, L. Gucma, and K. Łazuga, "Risk Assessment of Moored and Passing Ships," *Appl. Sci.*, vol. 10, no. 19, p. 6825, Sept. 2020, doi: 10.3390/app10196825.

[51] Allianz, *SAFETY and Shipping 1912-2012: From Titanic to Costa Concordia : An Insurer's Perspective from Allianz Global Corporate and Specialty*. AGCS, 2015. [Online]. Available: https://books.google.it/books?id=1ERNzwEACAAJ

[52] A. U. Schubert, M. Kurowski, M. Gluch, O. Simanski, and T. Jeinsch, "Manoeuvring Automation towards Autonomous Shipping," presented at the International Ship Control Systems Symposium, Glasgow, UK, Oct. 2018. doi: 10.24868/issn.2631-8741.2018.020.

[53] A. Lazarowska, "Review of Collision Avoidance and Path Planning Methods for Ships Utilizing Radar Remote Sensing," *Remote Sens.*, vol. 13, no. 16, p. 3265, Aug. 2021, doi: 10.3390/rs13163265.

[54] Z. Fang, H. Yu, R. Ke, S.-L. Shaw, and G. Peng, "Automatic Identification System-Based Approach for Assessing the Near-Miss Collision Risk Dynamics of Ships in Ports," *IEEE Trans. Intell. Transp. Syst.*, vol. 20, no. 2, pp. 534–543, Feb. 2019, doi: 10.1109/TITS.2018.2816122.

[55] S. Galić, Z. Lušić, S. Mladenović, and A. Gudelj, “A Chronological Overview of Scientific Research on Ship Grounding Frequency Estimation Models,” *J. Mar. Sci. Eng.*, vol. 10, no. 2, p. 207, Feb. 2022, doi: 10.3390/jmse10020207.

[56] K. Bergman, O. Ljungqvist, J. Linder, and D. Axehill, “An Optimization-Based Motion Planner for Autonomous Maneuvering of Marine Vessels in Complex Environments,” in *2020 59th IEEE Conference on Decision and Control (CDC)*, Jeju, Korea (South): IEEE, Dec. 2020, pp. 5283–5290. doi: 10.1109/CDC42340.2020.9303746.

[57] M. Gil, “A concept of critical safety area applicable for an obstacle-avoidance process for manned and autonomous ships,” *Reliab. Eng. Syst. Saf.*, vol. 214, p. 107806, Oct. 2021, doi: 10.1016/j.ress.2021.107806.

[58] A. Lazarowska, “Review of Collision Avoidance and Path Planning Methods for Ships Utilizing Radar Remote Sensing,” *Remote Sens.*, vol. 13, no. 16, p. 3265, Aug. 2021, doi: 10.3390/rs13163265.

[59] A. R. J. Ruiz and F. S. Granja, “A Short-Range Ship Navigation System Based on Ladar Imaging and Target Tracking for Improved Safety and Efficiency,” *IEEE Trans. Intell. Transp. Syst.*, vol. 10, no. 1, pp. 186–197, Mar. 2009, doi: 10.1109/TITS.2008.2011698.

[60] E. Cardillo, C. Li, and A. Caddemi, “Embedded heating, ventilation, and air-conditioning control systems: From traditional technologies toward radar advanced sensing,” *Rev. Sci. Instrum.*, vol. 92, no. 6, p. 061501, June 2021, doi: 10.1063/5.0044673.

[61] E. Cardillo, C. Li, and A. Caddemi, “Millimeter-Wave Radar Cane: A Blind People Aid With Moving Human Recognition Capabilities,” *IEEE J. Electromagn. RF Microw. Med. Biol.*, vol. 6, no. 2, pp. 204–211, June 2022, doi: 10.1109/JERM.2021.3117129.

[62] H. Li, A. Mehul, J. Le Kernec, S. Z. Gurbuz, and F. Fioranelli, “Sequential Human Gait Classification With Distributed Radar Sensor Fusion,” *IEEE Sens. J.*, vol. 21, no. 6, pp. 7590–7603, Mar. 2021, doi: 10.1109/JSEN.2020.3046991.

[63] S. M. M. Islam and V. M. Lubecke, “Sleep Posture Recognition With a Dual-Frequency Microwave Doppler Radar and Machine Learning Classifiers,” *IEEE Sens. Lett.*, vol. 6, no. 3, pp. 1–4, Mar. 2022, doi: 10.1109/LSENS.2022.3148378.

[64] E. Cardillo and A. Caddemi, “A novel approach for crosstalk minimisation in frequency modulated continuous wave radars,” *Electron. Lett.*, vol. 53, no. 20, pp. 1379–1381, Sept. 2017, doi: 10.1049/el.2017.2800.

[65] S. Kueppers, T. Jaeschke, N. Pohl, and J. Barowski, “Versatile 126–182 GHz UWB D-Band FMCW Radar for Industrial and Scientific Applications,” *IEEE Sens. Lett.*, vol. 6, no. 1, pp. 1–4, Jan. 2022, doi: 10.1109/LSENS.2021.3130709.

[66] A. Caddemi and E. Cardillo, “Automotive Anti-Abandon Systems: a Millimeter-Wave Radar Sensor for the Detection of Child Presence,” in *2019 14th International Conference on Advanced Technologies, Systems and Services in Telecommunications (TELSIKS)*, Nis, Serbia: IEEE, Oct. 2019, pp. 94–97. doi: 10.1109/TELSIKS46999.2019.9002193.

[67] A. Stateczny, W. Kazimierski, D. Gronska-Sledz, and W. Motyl, “The Empirical Application of Automotive 3D Radar Sensor for Target Detection for an Autonomous Surface Vehicle’s Navigation,” *Remote Sens.*, vol. 11, no. 10, p. 1156, May 2019, doi: 10.3390/rs11101156.

[68] P. L. Herselman, C. J. Baker, and H. J. De Wind, “An Analysis of X-Band Calibrated Sea Clutter and Small Boat Reflectivity at Medium-to-Low Grazing Angles,” *Int. J. Navig. Obs.*, vol. 2008, no. 1, p. 347518, Jan. 2008, doi: 10.1155/2008/347518.

[69] T. Kempf, M. Peichl, S. Dill, and H. Süß, “Microwave radar signature acquisition of urban structures.” Sept. 2007.

[70] G. Muntoni, G. Montisci, T. Pisanu, P. Andronico, and G. Valente, “Crowded Space: A Review on Radar Measurements for Space Debris Monitoring and Tracking,” *Appl. Sci.*, vol. 11, no. 4, p. 1364, Feb. 2021, doi: 10.3390/app11041364.

[71] R. Biesbroek, S. Aziz, A. Wolahan, S. Cipolla, M. Richard-Noca, and L. Piguet, “THE CLEARSPACE-1 MISSION: ESA AND CLEARSPACE TEAM UP TO REMOVE DEBRIS”.

[72] *Space Debris*. in Springer Praxis Books. Springer Berlin Heidelberg, 2006. doi: 10.1007/3-540-37674-7.

[73] J. Xi, Y. Xiang, O. K. Ersoy, M. Cong, X. Wei, and J. Gu, “Space Debris Detection Using Feature Learning of Candidate Regions in Optical Image Sequences,” *IEEE Access*, vol. 8, pp. 150864–150877, 2020, doi: 10.1109/ACCESS.2020.3016761.

[74] L. Felicetti and M. R. Emami, “A multi-spacecraft formation approach to space debris surveillance,” *Acta Astronaut.*, vol. 127, pp. 491–504, Oct. 2016, doi: 10.1016/j.actaastro.2016.05.040.

[75] H. Zhao, X. Fu, M. Gao, and S. Ding, “Research on the visibility of low-orbit debris using space-borne radar,” *IET Radar Sonar Navig.*, vol. 9, no. 1, pp. 31–37, Jan. 2015, doi: 10.1049/iet-rsn.2013.0295.

[76] D. Cerutti-Maori, J. Rosebrock, I. O. Maouloud, L. Leushacke, and H. Krag, “PRELIMINARY CONCEPT OF A SPACE-BASED RADAR FOR DETECTING MM-SIZE SPACE DEBRIS”.

[77] A. Anttonen, M. Kiviranta, and M. Höyhtyä, “Space debris detection over intersatellite communication signals,” *Acta Astronaut.*, vol. 187, pp. 156–166, Oct. 2021, doi: 10.1016/j.actaastro.2021.06.023.

[78] E. Cardillo, R. Cananzi, P. Vita, and A. Caddemi, “Dual-Conversion Microwave Down Converter for Nanosatellite Electronic Warfare Systems,” *Appl. Sci.*, vol. 12, no. 3, p. 1524, Jan. 2022, doi: 10.3390/app12031524.

[79] E. Cardillo, R. Cananzi, and P. Vita, “Wideband Versatile Receiver for CubeSat Microwave Front-Ends,” *Sensors*, vol. 22, no. 22, p. 9004, Nov. 2022, doi: 10.3390/s22229004.

[80] Changzhi Li, Xiaogang Yu, Chien-Ming Lee, Dong Li, Lixin Ran, and Jenshan Lin, “High-Sensitivity Software-Configurable 5.8-GHz Radar Sensor Receiver Chip in 0.13-μm CMOS for Noncontact Vital Sign Detection,” *IEEE Trans. Microw. Theory Tech.*, vol. 58, no. 5, pp. 1410–1419, May 2010, doi: 10.1109/TMTT.2010.2042856.

[81] S. Saponara and B. Neri, “Design of compact and low-power X-band Radar for mobility surveillance applications,” *Comput. Electr. Eng.*, vol. 56, pp. 46–63, Nov. 2016, doi: 10.1016/j.compeleceng.2016.10.004.

[82] E. Cardillo, C. Li, and A. Caddemi, “Heating, Ventilation, and Air Conditioning Control by Range-Doppler and Micro-Doppler Radar Sensor,” in *2021 18th European Radar Conference (EuRAD)*, London, United Kingdom: IEEE, Apr. 2022, pp. 21–24. doi: 10.23919/EuRAD50154.2022.9784461.

[83] L. Ferro, C. Li, and E. Cardillo, “Design Considerations for a 120 GHz MIMO Sparse Radar Array Based on SISO Integrated Circuits,” *Sensors*, vol. 25, no. 18, p. 5622, Sept. 2025, doi: 10.3390/s25185622.

[84] A. Moreira, P. Prats-Iraola, M. Younis, G. Krieger, I. Hajnsek, and K. P. Papathanassiou, “A tutorial on synthetic aperture radar,” *IEEE Geosci. Remote Sens. Mag.*, vol. 1, no. 1, pp. 6–43, Mar. 2013, doi: 10.1109/MGRS.2013.2248301.

[85] A. Fabrizi, P. Fiener, T. Jagdhuber, K. Van Oost, and F. Wilken, “Plasticulture detection at the country scale by combining multispectral and SAR satellite data,” *Sci. Rep.*, vol. 15, no. 1, p. 11339, Apr. 2025, doi: 10.1038/s41598-025-93658-2.

[86] K. Uddin, M. A. Matin, and F. J. Meyer, “Operational Flood Mapping Using Multi-Temporal Sentinel-1 SAR Images: A Case Study from Bangladesh,” *Remote Sens.*, vol. 11, no. 13, p. 1581, July 2019, doi: 10.3390/rs11131581.

[87] C. Bredendiek, D. Starke, S. Kueppers, K. Aufinger, and N. Pohl, “120 GHz MIMO FMCW radar chipset in a SiGe bipolar technology,” *Int. J. Microw. Wirel. Technol.*, pp. 1–13, Dec. 2024, doi: 10.1017/S1759078724000990.

[88] A. Bilato, V. Issakov, A. Mazzanti, and A. Bevilacqua, “A Multichannel D-Band Radar Receiver With Optimized LO Distribution,” *IEEE Solid-State Circuits Lett.*, vol. 4, pp. 141–144, 2021, doi: 10.1109/LSSC.2021.3099069.

[89] A. Di Serio, P. Hugler, F. Roos, and C. Waldschmidt, “2-D MIMO Radar: A Method for Array Performance Assessment and Design of a Planar Antenna Array,” *IEEE Trans. Antennas Propag.*, vol. 68, no. 6, pp. 4604–4616, June 2020, doi: 10.1109/TAP.2020.2972643.

[90] H. Yi, Z. Wang, D. Xia, H. Liu, and L. Li, “Periodic Asymmetric Trapezoidal Perturbation Microstrip Antenna for Millimeter-Wave Automotive Radar Sensors,” *IEEE Trans. Antennas Propag.*, vol. 71, no. 2, pp. 1369–1377, Feb. 2023, doi: 10.1109/TAP.2022.3227795.

[91] S. Kueppers, H. Cetinkaya, R. Herschel, and N. Pohl, “A Compact 24 × 24 Channel MIMO FMCW Radar System Using a Substrate Integrated Waveguide-Based Reference Distribution Backplane,” *IEEE Trans. Microw. Theory Tech.*, vol. 68, no. 6, pp. 2124–2133, June 2020, doi: 10.1109/TMTT.2020.2983676.

[92] Z. Xu, Y. Chen, and P. Zhang, “A Sparse Uniform Linear Array DOA Estimation Algorithm for FMCW Radar,” *IEEE Signal Process. Lett.*, vol. 30, pp. 823–827, 2023, doi: 10.1109/LSP.2023.3292739.

[93] H. Ruan, S. Balon, J. Wu, Q. Liu, J. Sun, and X. Wu, “A Joint Design of Sparse Array Layout and DOA Algorithm for mmWave FMCW Radar,” in *2024 IEEE Radar Conference (RadarConf24)*, Denver, CO, USA: IEEE, May 2024, pp. 1–6. doi: 10.1109/RadarConf2458775.2024.10549657.

[94] G. He, Y. Zhang, Z. Dong, T. Song, J. Zhu, and J. Wang, “A DOA Estimation Algorithm with No Angle Ambiguity for SULA of FMCW Radar,” in *2024 International Radar Conference (RADAR)*, Rennes, France: IEEE, Oct. 2024, pp. 1–5. doi: 10.1109/RADAR58436.2024.10993970.

[95] H. Long, Z. Zhang, and Z. Yang, “High-Resolution Radar Imaging Jointly Exploiting Multiple Beams with Sidelobes and Grating Lobes,” in *2025 IEEE Wireless Communications and Networking Conference (WCNC)*, Milan, Italy: IEEE, Mar. 2025, pp. 1–6. doi: 10.1109/WCNC61545.2025.10978404.

[96] V. Valenta *et al.*, “Design and experimental evaluation of compensated bondwire interconnects above 100 GHz,” *Int. J. Microw. Wirel. Technol.*, vol. 7, no. 3–4, pp. 261–270, June 2015, doi: 10.1017/S1759078715000070.

[97] R. Z. Syeda, M. C. Van Beurden, and A. B. Smolders, “Sparse virtual array synthesis for MIMO radar imaging systems,” *IET Microw. Antennas Propag.*, vol. 15, no. 11, pp. 1458–1472, Sept. 2021, doi: 10.1049/mia2.12129.

[98] Z. Peng and C. Li, “A Portable K-Band 3-D MIMO Radar With Nonuniformly Spaced Array for Short-Range Localization,” *IEEE Trans. Microw. Theory Tech.*, pp. 1–12, 2018, doi: 10.1109/TMTT.2018.2869565.

[99] M. I. Skolnik, *Radar handbook*, 3rd ed. New York: McGraw-Hill, 2008.

[100] S. J. Orfanidis, *Electromagnetic Waves and Antennas*, 2004th ed. New Brunswick, NJ: Rutgers University.

[101] T. Spreng, S. Yuan, V. Valenta, H. Schumacher, U. Siart, and V. Ziegler, “Wideband 120 GHz to 140 GHz MIMO radar: System design and imaging results,” in *2015 European Microwave Conference (EuMC)*, Paris, France: IEEE, Sept. 2015, pp. 430–433. doi: 10.1109/EuMC.2015.7345792.

[102] “RO3000® Laminate Data Sheet RO3003 - RO3006 - RO3010 - RO3035.” Rogers Corporation, 2024. [Online]. Available: www.rogerscorp.com

[103] S. Bertl, A. Kirschner, and J. Detlefsen, “Suppression of grating lobes for MMW sparse array setups,” *Adv. Radio Sci.*, vol. 9, pp. 67–71, July 2011, doi: 10.5194/ars-9-67-2011.

[104] J.-H. Park and J.-R. Yang, “Multiphase Continuous-Wave Doppler Radar With Multiarc Circle Fitting Algorithm for Small Periodic Displacement Measurement,” *IEEE Trans. Microw. Theory Tech.*, vol. 69, no. 11, pp. 5135–5144, Nov. 2021, doi: 10.1109/TMTT.2020.3041264.

[105] F. Tong, J. Liu, C. Li, C. Gu, and J. Mao, “A Low-IF Doppler Radar With Asynchronous Bandpass Sampling for Accurate Measurement of Displacement Motions,” *IEEE Trans. Microw. Theory Tech.*, vol. 71, no. 1, pp. 456–465, Jan. 2023, doi: 10.1109/TMTT.2022.3221167.

[106] L. Ferro, C. Li, G. Scandurra, C. Ciofi, and E. Cardillo, “Beneficial Effects of Self-Motion for the Continuous Phase Analysis of Ac-Coupled Doppler Radars,” *Electronics*, vol. 13, no. 4, p. 772, Feb. 2024, doi: 10.3390/electronics13040772.

[107] L. Ferro, G. Scandurra, C. Li, and E. Cardillo, “Robust Doppler Displacement Measurement Resolving the Uncertainty During Target Stationary Moment,” in *2024 IEEE Topical Conference on Wireless Sensors and Sensor Networks (WiSNeT)*, San Antonio, TX, USA: IEEE, Jan. 2024, pp. 57–60. doi: 10.1109/WiSNeT59910.2024.10438649.

[108] L. Ferro, G. Scandurra, C. Ciofi, and E. Cardillo, “An Insight Into the Displacement Evaluation During Real-Time Radar Measurements,” *IEEE Sens. J.*, vol. 25, no. 17, pp. 32651–32658, Sept. 2025, doi: 10.1109/JSEN.2025.3594433.

[109] S. M. M. Islam, L. Oba, and V. M. Lubecke, “Empirical Mode Decomposition (EMD) for Platform Motion Compensation in Remote Life Sensing Radar,” in *2022 IEEE Radio and Wireless Symposium (RWS)*, Las Vegas, NV, USA: IEEE, Jan. 2022, pp. 41–44. doi: 10.1109/RWS53089.2022.9719920.

[110] S. M. M. Islam, L. C. Lubecke, C. Grado, and V. M. Lubecke, “An Adaptive Filter Technique for Platform Motion Compensation in Unmanned Aerial Vehicle Based Remote Life Sensing Radar,” in *2020 50th European Microwave Conference (EuMC)*,

Utrecht, Netherlands: IEEE, Jan. 2021, pp. 937–940. doi: 10.23919/EuMC48046.2021.9338011.

[111] E. Cardillo, C. Li, and A. Caddemi, "Vital Sign Detection and Radar Self-Motion Cancellation Through Clutter Identification," *IEEE Trans. Microw. Theory Tech.*, vol. 69, no. 3, pp. 1932–1942, Mar. 2021, doi: 10.1109/TMTT.2021.3049514.

[112] N. Chordas-Ewell, K. Xu, R. Kadlimatti, A. T. Fam, and J. H. Choi, "Vibrating Antenna Doppler Radar," in *2020 17th European Radar Conference (EuRAD)*, Utrecht, Netherlands: IEEE, Jan. 2021, pp. 242–245. doi: 10.1109/EuRAD48048.2021.00069.

[113] T. Arai *et al.*, "A 77-GHz 8RX3TX Transceiver for 250-m Long-Range Automotive Radar in 40-nm CMOS Technology," *IEEE J. Solid-State Circuits*, vol. 56, no. 5, pp. 1332–1344, May 2021, doi: 10.1109/JSSC.2021.3050306.

[114] M. Zhou, Y. Liu, S. Wu, C. Wang, Z. Chen, and H. Li, "A Novel Scheme of High-Precision Heart Rate Detection With a mm-Wave FMCW Radar," *IEEE Access*, vol. 11, pp. 85118–85136, 2023, doi: 10.1109/ACCESS.2023.3303335.

[115] M. Yang, J. Chen, and C. Shan, "Phase Locked-Loop Design of High-Order Automotive Frequency Modulated Continuous Wave Radar Based on Fast Integration Structure," *IEEE Access*, vol. 12, pp. 11926–11935, 2024, doi: 10.1109/ACCESS.2023.3344997.

[116] Z. Liang, J. Gai, X. Chen, T. Ma, and Q. Liu, "A Method for Threshold Setting and False Alarm Probability Evaluation for Radar Detectors," *Signal Process.*, vol. 207, p. 108930, June 2023, doi: 10.1016/j.sigpro.2023.108930.

[117] D. Rodriguez and C. Li, "Sensitivity and Distortion Analysis of a 125-GHz Interferometry Radar for Submicrometer Motion Sensing Applications," *IEEE Trans.*

Microw. Theory Tech., vol. 67, no. 12, pp. 5384–5395, Dec. 2019, doi: 10.1109/TMTT.2019.2951142.

[118] Y. Song, J. Fang, K. Zhang, R. Su, N. Zhang, and Y. Zhao, "Multi-state FMCW Radar Real-time Vital Signs Monitoring System," in *2023 IEEE 6th International Conference on Electronic Information and Communication Technology (ICEICT)*, Qingdao, China: IEEE, July 2023, pp. 1–6. doi: 10.1109/ICEICT57916.2023.10246004.

[119] M. Salman and Y. Noh, "Contactless Vital Signs Tracking with mmWave RADAR in Realtime," in *2023 IEEE International Conference on Big Data and Smart Computing (BigComp)*, Jeju, Korea, Republic of: IEEE, Feb. 2023, pp. 389–390. doi: 10.1109/BigComp57234.2023.00094.

[120] T. Gänzle, C. Klöck, and K. Heuschkel, "Real-Time Vital Sign Detection using a 77 GHz FMCW Radar," in *2022 IEEE-EMBS Conference on Biomedical Engineering and Sciences (IECBES)*, Kuala Lumpur, Malaysia: IEEE, Dec. 2022, pp. 148–153. doi: 10.1109/IECBES54088.2022.10079417.

[121] G. N. Rathna and D. Meshineni, "Analysis of FM CW-Radar signals to extract vital-sign information," in *2021 IEEE International Conference on Electronics, Computing and Communication Technologies (CONECCT)*, Bangalore, India: IEEE, July 2021, pp. 1–6. doi: 10.1109/CONECCT52877.2021.9622687.

[122] P. Tschapek, G. Korner, C. Carlowitz, and M. Vossiek, "Detailed Analysis and Modeling of Phase Noise and Systematic Phase Distortions in FMCW Radar Systems," *IEEE J. Microw.*, vol. 2, no. 4, pp. 648–659, Oct. 2022, doi: 10.1109/JMW.2022.3195574.

[123] G. Vallant, M. Epp, W. Schlecker, U. Schneider, L. Anttila, and M. Valkama, "Analog IQ impairments in Zero-IF radar receivers: Analysis, measurements and digital

compensation," in *2012 IEEE International Instrumentation and Measurement Technology Conference Proceedings*, Graz, Austria: IEEE, May 2012, pp. 1703–1707. doi: 10.1109/I2MTC.2012.6229222.

[124] T. Zhou, M. Yang, K. Jiang, H. Wong, and D. Yang, "MMW Radar-Based Technologies in Autonomous Driving: A Review," *Sensors*, vol. 20, no. 24, p. 7283, Dec. 2020, doi: 10.3390/s20247283.

[125] F. Zhao, H. Tan, and Z. Liu, "Safety Development Trend of the Intelligent and Connected Vehicle," presented at the WCX SAE World Congress Experience, Apr. 2020, pp. 2020-01–0085. doi: 10.4271/2020-01-0085.

[126] T. Custódio *et al.*, "A Change of Paradigm for the Design and Reliability Testing of Touch-Based Cabin Controls on the Seats of Self-Driving Cars," *Electronics*, vol. 11, no. 1, p. 21, Dec. 2021, doi: 10.3390/electronics11010021.

[127] K. Dandu *et al.*, "2.2 High-Performance and Small Form-Factor mm-Wave CMOS Radars for Automotive and Industrial Sensing in 76-to-81GHz and 57-to-64GHz Bands," in *2021 IEEE International Solid- State Circuits Conference (ISSCC)*, San Francisco, CA, USA: IEEE, Feb. 2021, pp. 39–41. doi: 10.1109/ISSCC42613.2021.9365838.

[128] Y. Chen, Y. Luo, A. Qi, M. Miao, and Y. Qi, "In-cabin Monitoring Based on Millimeter Wave FMCW radar," in *2021 13th International Symposium on Antennas, Propagation and EM Theory (ISAPE)*, Zhuhai, China: IEEE, Dec. 2021, pp. 01–03. doi: 10.1109/ISAPE54070.2021.9753085.

[129] S. Dias Da Cruz, H.-P. Beise, U. Schroder, and U. Karahasanovic, "A Theoretical Investigation of the Detection of Vital Signs in Presence of Car Vibrations and RADAR-

Based Passenger Classification," *IEEE Trans. Veh. Technol.*, vol. 68, no. 4, pp. 3374–3385, Apr. 2019, doi: 10.1109/TVT.2019.2898512.

[130] D. G. Bresnahan and Y. Li, "Classification of Driver Head Motions Using a mm-Wave FMCW Radar and Deep Convolutional Neural Network," *IEEE Access*, vol. 9, pp. 100472–100479, 2021, doi: 10.1109/ACCESS.2021.3096465.

[131] S. Ahmed, F. Khan, A. Ghaffar, F. Hussain, and S. H. Cho, "Finger-Counting-Based Gesture Recognition within Cars Using Impulse Radar with Convolutional Neural Network," *Sensors*, vol. 19, no. 6, p. 1429, Mar. 2019, doi: 10.3390/s19061429.

[132] A. Singh *et al.*, "Data-Based Quadrature Imbalance Compensation for a CW Doppler Radar System," *IEEE Trans. Microw. Theory Tech.*, vol. 61, no. 4, pp. 1718–1724, Apr. 2013, doi: 10.1109/TMTT.2013.2249525.

[133] B.-K. Park, S. Yamada, and V. Lubecke, "Measurement Method for Imbalance Factors in Direct-Conversion Quadrature Radar Systems," *IEEE Microw. Wirel. Compon. Lett.*, vol. 17, no. 5, pp. 403–405, May 2007, doi: 10.1109/LMWC.2007.895742.

[134] M. Uddin, S. Manickam, H. Ullah, M. Obaidat, and A. Dandoush, "Unveiling the Metaverse: Exploring Emerging Trends, Multifaceted Perspectives, and Future Challenges," *IEEE Access*, vol. 11, pp. 87087–87103, 2023, doi: 10.1109/ACCESS.2023.3281303.

[135] R. Chengoden *et al.*, "Metaverse for Healthcare: A Survey on Potential Applications, Challenges and Future Directions," *IEEE Access*, vol. 11, pp. 12765–12795, 2023, doi: 10.1109/ACCESS.2023.3241628.

[136] S. Dong *et al.*, “Doppler Cardiogram: A Remote Detection of Human Heart Activities,” *IEEE Trans. Microw. Theory Tech.*, vol. 68, no. 3, pp. 1132–1141, Mar. 2020, doi: 10.1109/TMTT.2019.2948844.

[137] R. A. Nelson and M. G. Olsson, “The pendulum—Rich physics from a simple system,” *Am. J. Phys.*, vol. 54, no. 2, pp. 112–121, Feb. 1986, doi: 10.1119/1.14703.

[138] E. Cardillo *et al.*, “Development of a Simple Setup to Measure Shielding Effectiveness at Microwave Frequencies,” *Sensors*, vol. 24, no. 12, p. 3741, June 2024, doi: 10.3390/s24123741.

[139] World Health Organization, *World report on vision*. Geneva: World Health Organization, 2019. Accessed: Aug. 20, 2025. [Online]. Available: https://iris.who.int/handle/10665/328717

[140] M. B. Bachli *et al.*, “Evaluating the reliability of neurocognitive biomarkers of neurodegenerative diseases across countries: A machine learning approach,” *NeuroImage*, vol. 208, p. 116456, Mar. 2020, doi: 10.1016/j.neuroimage.2019.116456.

[141] N. P. Oxtoby and D. C. Alexander, “Imaging plus X: multimodal models of neurodegenerative disease,” *Curr. Opin. Neurol.*, vol. 30, no. 4, pp. 371–379, Aug. 2017, doi: 10.1097/WCO.0000000000000460.

[142] C. K. Behera, J. Condell, S. Dora, D. S. Gibson, and G. Leavey, “State-of-the-Art Sensors for Remote Care of People with Dementia during a Pandemic: A Systematic Review,” *Sensors*, vol. 21, no. 14, p. 4688, July 2021, doi: 10.3390/s21144688.

[143] T. Wibble, T. Pansell, S. Grillner, and J. Pérez-Fernández, “Conserved subcortical processing in visuo-vestibular gaze control,” *Nat. Commun.*, vol. 13, no. 1, p. 4699, Aug. 2022, doi: 10.1038/s41467-022-32379-w.

[144] W. Deng, J. Huang, S. Kong, Y. Zhan, J. Lv, and Y. Cui, “Pupil trajectory tracing from video-oculography with a new definition of pupil location,” *Biomed. Signal Process. Control*, vol. 79, p. 104196, Jan. 2023, doi: 10.1016/j.bspc.2022.104196.

[145] C. Waddington and J. Kofman, “Analysis of measurement sensitivity to illuminance and fringe-pattern gray levels for fringe-pattern projection adaptive to ambient lighting,” *Opt. Lasers Eng.*, vol. 48, no. 2, pp. 251–256, Feb. 2010, doi: 10.1016/j.optlaseng.2009.07.001.

[146] L. Ren, L. Kong, F. Foroughian, H. Wang, P. Theilmann, and A. E. Fathy, “Comparison Study of Noncontact Vital Signs Detection Using a Doppler Stepped-Frequency Continuous-Wave Radar and Camera-Based Imaging Photoplethysmography,” *IEEE Trans. Microw. Theory Tech.*, vol. 65, no. 9, pp. 3519–3529, Sept. 2017, doi: 10.1109/TMTT.2017.2658567.

[147] L. Wen, Y. Gao, C. Gu, and J. Mao, “PhysioChair: A Dual-Frequency Radar System for Noninvasive and Continuous Detection of Physiological Signatures,” *IEEE Sens. J.*, vol. 22, no. 8, pp. 8224–8233, Apr. 2022, doi: 10.1109/JSEN.2022.3159587.

[148] Z. Fang *et al.*, “Wide Field-of-View Locating and Multimodal Vital Sign Monitoring Based on ${X}$ -Band CMOS-Integrated Phased-Array Radar Sensor,” *IEEE Trans. Microw. Theory Tech.*, vol. 68, no. 9, pp. 4054–4065, Sept. 2020, doi: 10.1109/TMTT.2020.2989284.

[149] P.-H. Juan, C.-Y. Chueh, and F.-K. Wang, “Distributed MIMO CW Radar for Locating Multiple People and Detecting Their Vital Signs,” *IEEE Trans. Microw. Theory Tech.*, vol. 71, no. 3, pp. 1312–1325, Mar. 2023, doi: 10.1109/TMTT.2022.3216577.

[150] Y. Yuan, A. Y.-K. Chen, and C.-T. M. Wu, “Super-Regenerative Oscillator-Based High-Sensitivity Radar Architecture for Motion Sensing and Vital Sign Detection,” *IEEE Trans. Microw. Theory Tech.*, vol. 69, no. 3, pp. 1974–1984, Mar. 2021, doi: 10.1109/TMTT.2021.3053972.

[151] S. Dong, Y. Li, J. Lu, Z. Zhang, C. Gu, and J. Mao, “Accurate Detection of Doppler Cardiograms With a Parameterized Respiratory Filter Technique Using a K-Band Radar Sensor,” *IEEE Trans. Microw. Theory Tech.*, vol. 71, no. 1, pp. 71–82, Jan. 2023, doi: 10.1109/TMTT.2022.3184019.

[152] E. Cardillo, C. Li, and A. Caddemi, “Radar-Based Monitoring of the Worker Activities by Exploiting Range-Doppler and Micro-Doppler Signatures,” in *2021 IEEE International Workshop on Metrology for Industry 4.0 & IoT (MetroInd4.0&IoT)*, Rome, Italy: IEEE, June 2021, pp. 412–416. doi: 10.1109/MetroInd4.0IoT51437.2021.9488464.

[153] Y. Shu, Y. Wang, X. Yang, and Z. Tian, “An improved denoising method for eye blink detection using automotive millimeter wave radar,” *EURASIP J. Adv. Signal Process.*, vol. 2022, no. 1, p. 9, Dec. 2022, doi: 10.1186/s13634-022-00841-y.

[154] L. Ma, Y. Ye, C. Gu, and J. Mao, “High-Accuracy Contactless Detection of Eyes’ Activities based on Short-Range Radar Sensing,” in *2022 IEEE MTT-S International Microwave Biomedical Conference (IMBioC)*, Suzhou, China: IEEE, May 2022, pp. 266–268. doi: 10.1109/IMBioC52515.2022.9790181.

[155] Y. Wang, Y. Shu, and M. Zhou, “A Novel Eye Blink Detection Method using Frequency Modulated Continuous Wave Radar,” in *2021 IEEE International Workshop on Electromagnetics: Applications and Student Innovation Competition (iWEM)*, Guangzhou, China: IEEE, Nov. 2021, pp. 1–3. doi: 10.1109/iWEM53379.2021.9790529.

[156] X. Yang, S. A. Kurt, Q. Zeng, X. Tian, M. Zhao, and J. S. Ho, “Non-contact mmWave Physiological Sensor in Eyewear Based on Spoof Localized Surface Plasmons,” in *2023 IEEE/MTT-S International Microwave Symposium - IMS 2023*, San Diego, CA, USA: IEEE, June 2023, pp. 975–978. doi: 10.1109/IMS37964.2023.10188017.

[157] E. Cardillo, G. Sapienza, and A. Caddemi, “Sistema di rilevamento di movimenti (system for motion detection),” 102 022 000 010 118, May 16, 2022

[158] E. Cardillo, G. Sapienza, C. Li, and A. Caddemi, “Head Motion and Eyes Blinking Detection: a mm-Wave Radar for Assisting People with Neurodegenerative Disorders,” in *2020 50th European Microwave Conference (EuMC)*, Utrecht, Netherlands: IEEE, Jan. 2021, pp. 925–928. doi: 10.23919/EuMC48046.2021.9338116.

[159] Y. Kim, “Detection of Eye Blinking Using Doppler Sensor With Principal Component Analysis,” *IEEE Antennas Wirel. Propag. Lett.*, vol. 14, pp. 123–126, 2015, doi: 10.1109/LAWP.2014.2357340.

[160] J. Hu *et al.*, “BlinkRadar: Non-Intrusive Driver Eye-Blink Detection with UWB Radar,” in *2022 IEEE 42nd International Conference on Distributed Computing Systems (ICDCS)*, Bologna, Italy: IEEE, July 2022, pp. 1040–1050. doi: 10.1109/ICDCS54860.2022.00104.

[161] M. Higashino, K. Miyata, and K. Kudo, “Coordination dynamics of thoracic and abdominal movements during voluntary breathing,” *Sci. Rep.*, vol. 12, no. 1, p. 13266, Aug. 2022, doi: 10.1038/s41598-022-17473-9.

[162] K. Hwang, “Surgical anatomy of the upper eyelid relating to upper blepharoplasty or blepharoptosis surgery,” *Anat. Cell Biol.*, vol. 46, no. 2, p. 93, 2013, doi: 10.5115/acb.2013.46.2.93.

[163] J. N. Caviness, “Myoclonus and neurodegenerative disease—what’s in a name?,” *Parkinsonism Relat. Disord.*, vol. 9, no. 4, pp. 185–192, Mar. 2003, doi: 10.1016/S1353-8020(02)00054-8.

List of publications

[1] G. Scandurra, E. Cardillo, L. Ferro, G. Giusi, and C. Ciofi, “On the instrumentation for current noise measurements in low impedance devices,” *Fluctuation and Noise Letters*, under review.

[2] L. Ferro*, C. Li, and E. Cardillo, “Design considerations for a 120 GHz MIMO sparse radar array based on SISO integrated circuits,” *Sensors*, vol. 25, iss. 18, no. 5622, Sept. 2025, DOI: 10.3390/s25185622.

[3] L. Ferro*, G. Scandurra, C. Ciofi and E. Cardillo, “An insight into the displacement evaluation during real-time radar measurements,” *IEEE Sensors Journal*, vol. 25, no. 17, pp. 32651-32658, Sept. 2025, DOI: 10.1109/JSEN.2025.3594433.

[4] L. Ferro*, and E. Cardillo, “Frequency Shift in Microwave Circuits Manufactured with Circuit Board Plotters: Case Study of a Parallel Coupled Lines Filter,” *Electronics*, vol. 13, iss. 15, no. 3100, Aug. 2024, DOI: 10.3390/electronics13153100.

[5] E. Cardillo, L. Ferro*, and F. L. Carcione, “An Insight on the Microwave Circulator Theory,” *IEEE Access*, vol. 12, pp. 92164-92168, Jul. 2024, DOI: 10.1109/ACCESS.2024.3421943.

[6] C. Ciofi, E. Cardillo, L. Ferro, G. Giusi and G. Scandurra, “A Simple, Portable, Two Channels Correlation Spectrum Analyzer for Low Frequency Noise Measurements,” *2024 IEEE International Instrumentation and Measurement Technology Conference (I2MTC)*, Glasgow, United Kingdom, pp. 1-6, Jun. 2024, DOI: 10.1109/I2MTC60896.2024.10561212.

[7] E. Cardillo, F. L. Carcione, L. Ferro*, E. Piperopoulos, E. Mastronardo, G. Scandurra, and C. Ciofi, "Development of a simple setup to measure shielding effectiveness at microwave frequencies," *Sensors*, vol. 24, iss. 12, no. 3741, Jun. 2024, DOI: 10.3390/s24123741.

[8] L. Ferro*, C. Li, G. Scandurra, C. Ciofi, and E. Cardillo, "Beneficial effects of self-motion for the continuous phase analysis of AC-coupled Doppler radars," *Electronics*, vol. 13, iss. 4, no. 772, Feb. 2024, DOI: 10.3390/electronics13040772.

[9] L. Ferro*, G. Scandurra, C. Li, and E. Cardillo, "Robust Doppler displacement measurement resolving the uncertainty during target stationary moment," *2024 IEEE Radio and Wireless Week (RWW) - IEEE Topical Conference on Wireless Sensors and Sensor Networks (WiSNet)*, San Antonio, TX, USA, pp. 57-60, Jan. 2024, DOI: 10.1109/WiSNeT59910.2024.10438649.

[10] E. Cardillo, L. Ferro*, G. Sapienza, and C. Li, "Reliable eye-blinking detection with millimeter-wave radar glasses," *IEEE Transactions on Microwave Theory and Techniques*, vol.72, no. 1, pp. 771-779, Jan. 2024, DOI: 10.1109/TMTT.2023.3329707.

[11] E. Cardillo, L. Ferro*, and Davi V.Q. Rodrigues, "Exploiting millimeter-wave radars to enable accurate gesture recognition for the metaverse environment," *2023 54th Annual Meeting of the Italian Electronics Society (SIE)*, Noto, Italy, vol. 1113, pp. 110-115, *Lecture Notes in Electrical Engineering*, Nov. 2023. DOI: 10.1007/978-3-031-48711-8_13.

[12] E. Cardillo, R. Cananzi, L. Ferro, C. Li, P. Vita, and P. Vita, "Detection of space debris through compact X band FMCW radar," *2023 16th International Conference on Advanced*

Technologies, Systems and Services in Telecommunications (TELSIKS), Niš, Serbia, pp. 126-129, Oct. 2023. DOI: 10.1109/TELSIKS57806.2023.10316106.

[13] G. Scandurra, C. Ciofi, E. Cardillo, and L. Ferro, "Portable impedance meter for focused impedance applications," *2023 17th International Workshop on Impedance Spectroscopy (IWIS)*, Chemnitz, Germany, pp. 73-78, Sept. 2023. DOI: 10.1109/IWIS61214.2023.10302766.

[14] E. Cardillo, G. Sapienza, L. Ferro, C. Li, and A. Caddemi, "Radar assistive system for people with neurodegenerative disorders through head motion and eyes blinking detection," *2023 IEEE/MTT-S International Microwave Symposium (IMS)*, San Diego, CA, USA, vol. 2023, pp. 979-982, Jun. 2023. DOI: 10.1109/IMS37964.2023.10187979.

[15] E. Cardillo, L. Ferro, C. Li, and A. Caddemi, "Microwave radars for automotive in-cabin detection," *2022 53th Annual Meeting of the Italian Electronics Society (SIE)*, Pizzo, Italy, vol. 1005, pp. 75-80, *Lecture Notes in Electrical Engineering*, Feb. 2023. DOI: 10.1007/978-3-031-26066-7_12.

[16] E. Cardillo, L. Ferro, and C. Li, "Microwave and millimeter-wave radar circuits for the next generation contact-less in-cabin detection," *2022 Asia Pacific Microwave Conference (APMC)*, Yokohama, Japan, pp. 231-233, Nov. 2022. DOI: 10.23919/APMC55665.2022.9999764.

[17] G. Scandurra, E. Cardillo, C. Ciofi, and L. Ferro, "UHT milk characterization by electrical impedance spectroscopy," *Applied Sciences*, vol. 12, iss. 15, no. 7559, Aug. 2022. DOI: 10.3390/app12157559.

[18] U. Ferlito, A. Cisto, L. Ferro, G. Bruno, and A. D. Grasso, "Planar capacitive transducers for a miniaturized particulate matter detector," *Prime 2022 – 17th International*

Conference on PhD Research in Microelectronics and Electronics, Villasimius, Italy, pp. 49-52, Jun. 2022. DOI: 10.1109/PRIME55000.2022.9816769.

[19] E. Cardillo, and L. Ferro, "Multi-frequency analysis of microwave and millimeter-wave radars for ship collision avoidance," *2022 IEEE Mediterranean Microwave Symposium (MMS)*, Pizzo Calabro, Italy, pp. 1-4, May 2022. DOI: 10.1109/MMS55062.2022.9825520.